

Topological insulator based spintronics: Theoretical investigation of pure spin current devices and polarization measurements

Dissertation

zur Erlangung des akademischen Grades eines
Dr. rer. nat.
an der Fakultät für Physik
der Universität Bielefeld

vorgelegt von
Matthias Götte

im März 2017

1. Gutachter: Prof. Dr. Thomas Dahm
2. Gutachter: Prof. Dr. Jürgen Schnack

Gedruckt auf alterungsbeständigem Papier °° ISO 9706

Erklärung

Hiermit versichere ich, dass ich die vorliegende Arbeit selbstständig verfasst und keine anderen als die angegebenen Quellen und Hilfsmittel benutzt habe. Alle Stellen der Arbeit, die wörtlich oder sinngemäß aus anderen Quellen übernommen wurden, sind als solche kenntlich gemacht worden und die Arbeit wurde in gleicher oder ähnlicher Form noch keiner Prüfungsbehörde vorgelegt.

Bielefeld, den 24.03.2017

Matthias Götte

Danksagung

An dieser Stelle möchte ich mich bei allen bedanken, die mich während meiner Promotion unterstützt haben.

Ganz besonderer Dank gilt dabei Prof. Dr. Thomas Dahm für die Betreuung während meiner Promotion und dafür, dass er mir diese überhaupt erst ermöglicht hat. Er hat sich stets Zeit genommen um mit mir über Ergebnisse und Probleme zu diskutieren. Dabei hat er thematische Vorschläge unterbreitet, mir aber immer auch die Freiheit gelassen eigene Ideen zu verfolgen.

Des Weiteren danke ich Prof. Dr. Jürgen Schnack dafür, dass er sich bereit erklärt hat meine Arbeit zu begutachten.

Allgemein bedanke ich mich bei allen Mitgliedern der Arbeitsgruppen auf E5 für ein angenehmes Arbeitsklima und freundliches Miteinander. Besonderer Dank geht dabei an meine Bürokollegen Igor Sapina und Matthias Borchering, die mir zudem durch diverse Diskussionen bei der Lösung einiger Probleme geholfen haben, und an Hanne Litschewski für ihre große Hilfsbereitschaft bei allen organisatorischen Dingen.

Schließlich möchte ich mich noch bei meiner Familie und meinen Freunden bedanken, die mir während meiner Promotion unterstützend zur Seite standen.

Publications in this thesis

1. Chapter 4 in parts reproduces calculations and results of the publication [1]:
M. Götze, M. Joppe, and T. Dahm, “Pure spin current devices based on ferromagnetic topological insulators,” *Scientific Reports* 6, 36070 (2016).
2. Chapter 5 in parts reproduces concepts and calculations of the publication [2]:
M. Götze, T. Paananen, G. Reiss, and T. Dahm, “Tunneling Magnetoresistance Devices Based on Topological Insulators: Ferromagnet–Insulator–Topological-Insulator Junctions Employing Bi_2Se_3 ,” *Phys. Rev. Applied* 2, 054010 (2014).

Contents

1	Introduction	1
2	Thematic background	3
2.1	Topological insulators	3
2.2	Quantum anomalous Hall effect	10
2.3	Spintronic	11
3	Model Hamiltonian	13
3.1	Effective model for the Bi_2Se_3 class of 3D TIs	13
3.1.1	Tight-binding-approximation	16
3.1.2	Tetragonal lattice	18
3.1.3	Hexagonal lattice	20
3.2	Analytical dispersion and surface states	21
4	Pure spin current devices and quantum transport calculations	27
4.1	Evolution of edge states in a ferromagnetic exchange field	28
4.2	Transport algorithm	34
4.2.1	Wave packets	35
4.2.2	Numerical time-evolution	38
4.2.3	Boundary conditions	40
4.2.4	Observables	41
4.3	2D transport calculations	43
4.3.1	Out-of-plane field	44
4.3.2	In-plane field	50
4.3.3	Parameter stability	52
4.4	Pure spin current devices	55
4.4.1	Generator	55
4.4.2	Detector	58
4.4.3	Transistor	59
4.5	Towards more realistic modeling	61
4.5.1	Domain walls	61
4.5.2	Finite thickness	65
4.5.3	Material imperfections	74
4.5.4	Broken structural inversion symmetry	75
4.5.5	Inhomogeneous exchange field	83
4.6	Summary	87

Contents

5 Meservey Tedrow method	89
5.1 Derivation	91
5.1.1 Influence of the out-of-plane polarization	100
5.1.2 Geometrical factor	103
5.2 Spin diffusion length	107
5.3 Summary	108
6 Spin Hall effect tunneling spectroscopy	111
6.1 Derivation	111
6.2 Numerical test	116
6.3 Summary	118
7 Summary and conclusion	121

1 Introduction

Spintronics (spin-based electronics) is more and more included into conventional information technology because it can significantly reduce the size of device structures and the power consumption. Aside from that, it enables completely new device concepts. It is therefore a very active field of research, often with close connection to applications. The giant magnetoresistance (GMR) effect and, more recently, the tunneling magnetoresistance (TMR) effect are commonly used in read heads of hard disk drives. Compared to conventional charge based concepts, they allowed a dramatic increase of the storage density because of a much higher sensitivity [3–5]. Nowadays, magnetic tunnel junctions in nonvolatile magnetoresistive random access memory (MRAM) can be switched all electrically via the spin-transfer-torque by injection of spin polarized currents [6], and many other spintronic applications may follow as new materials are discovered [5].

Over the last few years, topological insulators (TIs) have generated great interest in the field of spintronics [1, 2, 5, 7–14] because of their unique properties. Like trivial insulators, they have a bulk energy gap separating valence and conduction band. Inside this bulk gap, however, they feature topologically protected surface states or, in the two-dimensional (2D) case, edge states [15, 16]. As TIs preserve time-reversal symmetry, edge or surface states with opposite momentum have to have opposite spin. This has the consequence that currents flowing into opposite directions carry opposite spin and elastic backscattering by time-reversal symmetry preserving perturbations is strongly suppressed. For edge states of 2D TIs, such scattering processes are even completely forbidden [17]. By inducing magnetic order into a 2D TI, it can be driven into a quantum anomalous Hall (QAH) state, where one of the two edge state channels is gapped out so that only one unidirectional spin polarized edge channel remains [18–20].

In this thesis, three different topics are studied which can all be seen in the context of TI based spintronics. The first topic is about currents flowing in gapless states of 2D TIs with locally induced magnetic order, studied by means of numerical quantum transport calculations. Based on the obtained results, devices are conceived which are capable of creating, switching and detecting pure spin currents, i.e. spin currents without net charge flow.

The other two topics are about measuring the spin of topological surface states, which is crucial for the applicability and efficiency of TIs in spintronic applications. A method first considered by Meservey and Tedrow [21, 22] uses tunneling from superconducting aluminum films in a strong magnetic field to investigate the polarization of ferromagnetic materials. It is shown that, by making some changes, this method can be used to measure the in-plane spin component of topological surface states. By investigating another method called spin Hall effect tunneling spectroscopy [23, 24], it is shown that tunneling from ferromagnets can be used to give a relation between the in-plane and out-of-plane component of the surface state spin. When the in-plane component is already known, this allows measurement of the

1 Introduction

out-of-plane spin.

The thesis starts with an introducing chapter about TIs and the QAH effect and their potential role in spintronics to give a theoretical background for the rest of the thesis. In the subsequent chapter, the model Hamiltonian, which is the basis for all calculations in this thesis, is introduced and examined analytically. After three chapters covering the three main topics, a complete summary is given.

2 Thematic background

This chapter summarizes the discovery and basic properties of TIs and the QAH effect in order to give a thematic background for the content of this thesis. Detailed introductions about TIs can be found, e.g., in review articles by Hasan and Kane [17] and Qi and Zhang [25]. After this more general introduction, the topics of this thesis will be presented in the context of potential applications of TIs in the field of spintronics. More general introductions to the field of spintronics can be found in review articles by Wolf *et al.* [3], Žutić *et al.* [4] and Bader and Parkin [5].

2.1 Topological insulators

The advent of TIs began about a decade ago with the theoretical prediction [15] and successive experimental realization [26] of the quantum spin Hall (QSH) effect in HgTe/CdTe quantum wells. Similar to the quantum Hall (QH) insulator, which arises when a 2D electron gas in a semiconductor is exposed to a strong magnetic field [27], the QSH insulator, or 2D TI, features one-dimensional (1D) conducting edge state channels in an otherwise insulating bulk gap (see Fig. 2.1) [15]. In a 2D semiconductor, a strong magnetic field causes the electrons to move in circular orbits, which leads to a splitting of the electron states into quantized Landau levels. At low temperature, the bulk of the semiconductor is insulating when the Fermi level is located between two Landau levels, but the edges feature chiral edge states. These edge states can be attributed to skipped cyclotron orbits of the electrons at the edges. When an electrical field is applied, the cyclotron orbits start to drift and cause a quantized Hall conductance $\sigma_{xy} = Ne^2/h$, where N is the number of filled Landau levels, e the electron charge and h the Planck constant. An increase of the magnetic field increases the splitting of the Landau levels so that the number of filled levels decreases. Hence, the resistance increases stepwise with increasing magnetic field [17, 27].

Electrons in chiral edge states can only move in one direction along the edge so that forward and backward moving electron channels are spatially separated in a system of sufficient width. These electrons are then immune to backscattering from any defects because there is simply no back-moving electron state at the same edge. While this robustness of the edge states makes QH insulators interesting for low dissipation semiconductor devices, the requirement of a strong magnetic field and low temperature makes them rather impracticable [17, 28].

The QSH effect, on the other hand, does not need an external magnetic field but originates from strong intrinsic spin-orbit coupling. More precisely, the QSH effect is only robust in the absence of magnetic fields, when time-reversal symmetry is preserved. Where the QH insulator has only one edge state channel, the QSH insulator has (at least) two counter-propagating edge state channels. Still, electrons in these edge states are immune to elastic backscattering

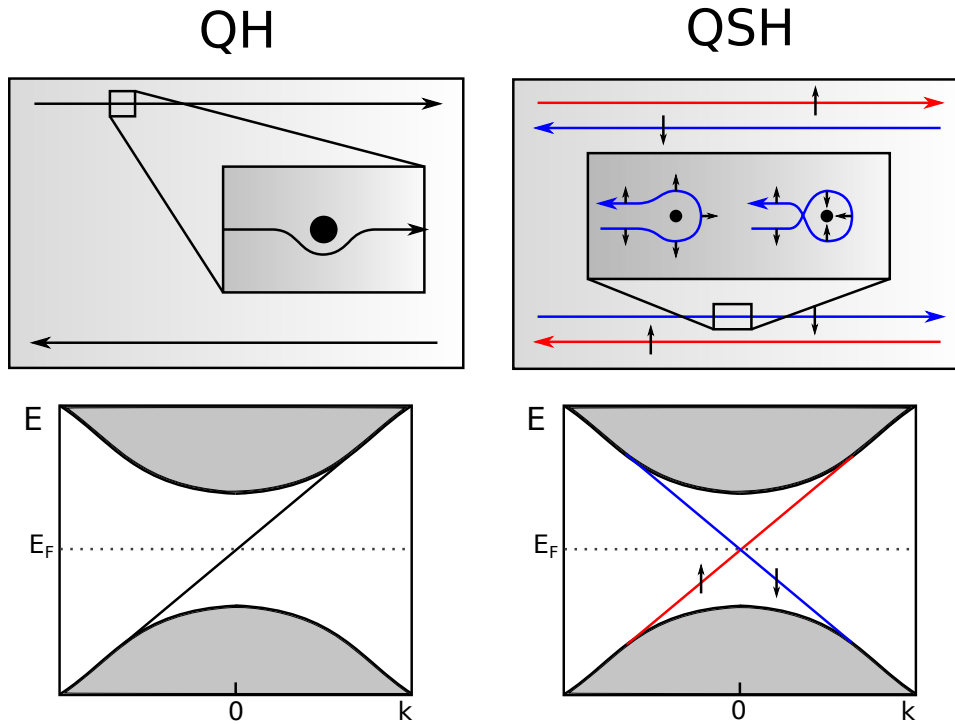


Figure 2.1: Schematic comparison of QH effect and QSH effect. Both effects feature 1D edge states in an insulating bulk gap (the QH state between Landau levels). Electrons in QH edge states are immune to backscattering because there is no back-moving state at the same edge. The electron will just move around any defect. The QSH state has two states per edge with opposite spin. Electrons can propagate either clockwise or counterclockwise around time-reversal symmetry preserving perturbations. As these paths differ by a total 2π rotation of the electron spin, corresponding to a relative minus sign of the wave functions, they interfere destructively. Time-reversal symmetry requires that the edge state bands cross in a so called Dirac point at $k = 0$. Figure inspired by Hasan and Kane [17] and Qi and Zhang [28].

from time reversal symmetry preserving perturbations because the edge states are helical, i.e. counter-propagating electrons have opposite spin (see Fig. 2.1). In order to change its movement direction, an electron has to change its spin. Depending on the path the electron takes around any perturbation, the spin is rotated adiabatically by either π or $-\pi$ so that the two paths differ by a total 2π rotation of the electron spin. As such a 2π rotation inverts the sign of the electron wave function, the two reflective paths interfere destructively. This destructive interference requires time-reversal symmetry. When time-reversal symmetry is broken, e.g. by a magnetic impurity, the edge state transport becomes dissipative [25, 28].

The case of only one forward and one backward moving electron state with opposite spins is the simplest. Generally, there can be multiple electron states per movement direction so that backscattering without an inversion of the spin is possible and transport can become dissipative. The QSH effect is therefore only robust when there is an odd number of forward and backward moving edge states, which is characterized by a \mathbb{Z}_2 topological quantum number [25]. Since there is no dissipation in the QSH state, the two-terminal longitudinal conductance should be quantized to $2e^2/h$ per pair of edge states [15], and indeed, a quantized conductance of $2e^2/h$ was measured for HgTe quantum wells beyond a critical thickness [26, 29].

Prior to the discovery of the QH effect, quantum states were classified by broken symmetries. For example, crystalline solids break translational symmetry, magnets rotation symmetry and superconductors gauge symmetry. The QH effect was the first quantum state which could not be classified in this way because its properties are a matter of topology instead of the exact geometry. This was the beginning of a new class of topological materials, which also includes the QSH effect or topological insulator [28].

The mathematical concept of topology can most easily be understood using the example of the 2D surfaces of three-dimensional (3D) objects. In topology, objects are not classified by their exact geometry. Instead, objects that can be smoothly deformed into each other are considered equivalent. For example, a sphere can be transformed into an ellipsoid by smooth deformations. These objects are therefore topologically equivalent. However, in order to transform the sphere into a torus (donut), a hole has to be created in the surface of the sphere, which is no smooth transformation. Thus, 3D objects can be classified by the number of holes the surface has, which is termed genus. In that sense, the donut is topologically equivalent to a coffee cup despite the completely different geometry [17].

This concept of a smooth transformation can be transferred to physical many-particle systems with a gap, i.e. insulators. If the Hamiltonian describing such a system can be smoothly transformed into the Hamiltonian of another system without closing the gap, the two systems are topologically equivalent. One of these topological equivalence classes is the trivial insulator, including atomic insulators and vacuum. Other classes are distinguished from the trivial insulator by topological quantum numbers similar to the genus. The existence of gapless edge states then already follows from this classification. Consider two systems described by different Hamiltonians that cannot be smoothly transformed into each other, i.e. that have different topological quantum numbers. When these systems are in contact, there has to be a point where a transition from one system to the other has to happen. Since this requires a closure of the gap, there must be gapless states located at the interface of the two systems. This relation is called bulk-boundary correspondence and is directly connected to the change of

2 Thematic background

the topological invariant along the interface [17].

All time-reversal invariant Hamiltonians can be assigned to two different classes classified by a \mathbb{Z}_2 topological invariant ν , which is 0 or 1 for topologically trivial or nontrivial insulators, respectively. A Bloch Hamiltonian $H(\mathbf{k})$ that is invariant under time-reversal satisfies [17]

$$\Theta H(\mathbf{k}) \Theta^{-1} = H(-\mathbf{k}), \quad (2.1)$$

where $\Theta = \exp(i\pi S_y/\hbar) K$ is an antiunitary operator representing the time-reversal symmetry. In this expression, S_y is the spin operator and K complex conjugation. Kramers' theorem now states that, for spin 1/2 electrons, all eigenstates of such a Hamiltonian are at least twofold degenerate because $\Theta^2 = -1$. Any non degenerate eigenstate $|\chi\rangle$ of Θ and $H(\mathbf{k})$ would have constant eigenvalues c so that $\Theta^2 |\chi\rangle = |c|^2 |\chi\rangle$ with $|c|^2 \neq -1$. Consider now a system that has a boundary. In that case, there can be states inside the bulk gap that are bound to the boundary. If this is the case, according to the Kramers' theorem, they have to be twofold degenerate at all time-reversal invariant momenta. For other momenta, the degeneracy is lifted by spin-orbit coupling. Depending on the topological invariant, these momenta are connected in a different fashion. If they are connected pairwise, it is possible to push the boundary states out of the bulk gap by a smooth change of the Hamiltonian. So this case is topologically trivial. However, if they are not connected pairwise, they are robust to smooth changes of the Hamiltonian. In the first case, the Fermi level is crossed an even number of times between two time-reversal invariant momenta. In the second case, the number is odd. The change $\Delta\nu$ of the topological quantum number across the boundary is therefore related to the number of boundary state pairs N_K (due to time-reversal symmetry, each boundary state at \mathbf{k} has a partner at $-\mathbf{k}$) crossing the Fermi level via the bulk-boundary correspondence [17]

$$N_K = \Delta\nu \bmod 2. \quad (2.2)$$

The remaining question is: What bulk property distinguishes the topologically nontrivial insulator from a trivial insulator? As mentioned above, the QSH effect arises in materials with strong spin-orbit coupling. Strong spin-orbit coupling can cause an inversion of the normal band order for parts of momentum space. If the bands forming the bulk gap are inverted at an odd number of time-reversal invariant momenta, the system is in a QSH state. In HgTe/CdTe quantum wells, the band ordering of the HgTe layer at the Γ point, i.e. $\mathbf{k} = 0$, changes as a function of the quantum well thickness d . For layers thinner than a critical thickness d_c , the bands have a normal ordering, so the quantum well is in a trivial state. When the thickness is increased beyond d_c , the band ordering in the HgTe layer is inverted, so the quantum well is in a QSH state [15]. In general, good potential candidates for new TI materials are therefore semiconductors with a rather small bulk gap and strong spin-orbit coupling, i.e. those consisting of heavy elements [30].

There are multiple approaches to calculate the topological invariant ν for a given band structure [25]. A simple algorithm by Fu and Kane [31] is based on the parity eigenvalues of occupied energy bands at the time-reversal invariant momenta in inversion symmetric insulators.

At each time-reversal invariant momentum Γ_i , the product [31]

$$\delta_i = \prod_{m=1}^N \xi_{2m}(\Gamma_i) \quad (2.3)$$

of the parity eigenvalues $\xi_{2m}(\Gamma_i) = \pm 1$ of all occupied Kramers' degenerate energy bands is calculated. The parity eigenvalues of the Kramers' pairs $2m$ and $2m - 1$ are the same, and the product runs only over these degenerate pairs. The topological quantum number ν is then determined by the product of all δ_i , i.e. in 2D [31]

$$(-1)^\nu = \prod_{i=1}^4 \delta_i. \quad (2.4)$$

On the basis of this equation, it can be seen that $\nu = 1$ only if bands of different parity are inverted at an odd number of time-reversal invariant momenta.

In 3D, four topological invariants can be defined. The generalization of Eq. (2.4) to the eight time-reversal invariant momenta of the 3D Brillouin zone gives the "strong" topological invariant ν_0 [31]

$$(-1)^{\nu_0} = \prod_{i=1}^8 \delta_i. \quad (2.5)$$

However, by multiplying any δ_i for which the Γ_i are in the same plane [31]

$$(-1)^{\nu_k} = \prod_{n_k=1; n_{j \neq k}=0,1} \delta_{i=(n_1 n_2 n_3)}, \quad (2.6)$$

three additional "weak" invariants ($\nu_1 \nu_2 \nu_3$) can be defined. These invariants depend on the definition of the lattice structure. A strong topological insulator ($\nu_0 = 1$) is the 3D generalization of the QSH effect, with protected surface states on all surfaces. In that case, the surface Fermi surface encloses an odd number of time-reversal invariant momenta. On the other hand, if $\nu_0 = 0$, the system can be viewed as stacked QSH insulators, where the stacking direction is defined by $(\nu_1 \nu_2 \nu_3)$. Then, there are no surface states at the top and bottom surface of the stack, only at the edges. As the surface Fermi surface encloses an even number of time-reversal invariant momenta, these edge states are not immune to perturbations [31].

Even though this approach is only valid if the insulator has inversion symmetry, it has already been of great use. For example, the proposal of the alloy $\text{Bi}_x\text{Sb}_{1-x}$ by Fu and Kane [31] and of the Bi_2Se_3 class by Zhang *et al.* [32] as 3D TIs is based on this approach. Additionally, it can also be applied to insulators without inversion symmetry if the Hamiltonian can be smoothly transformed into an inversion symmetric one since the topological invariant does not change under such transformations [25].

The alloy $\text{Bi}_x\text{Sb}_{1-x}$ was the first material that was identified as a strong 3D TI by observing nontrivial surface states by means of angle-resolved photoemission spectroscopy (ARPES) [33]. Later, also Bi_2Se_3 [34], Bi_2Te_3 [35, 36] and Sb_2Te_3 [37] were identified in the same way. These materials of the so called second generation have much simpler surface states and a

2 Thematic background

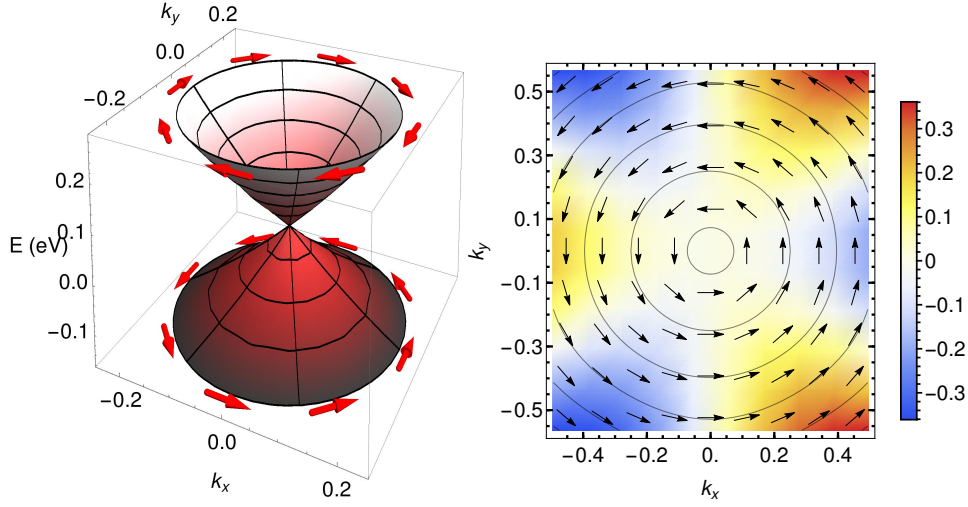


Figure 2.2: Dispersion and spin orientation of surface states of a 3D TI. The dispersion forms a nearly ideal Dirac cone (left panel), where the electron spin is locked orthogonal to the momentum and therefore rotates around the Fermi surface (indicated by red arrows). Some materials feature a hexagonal deformation of the Fermi surface along with an out-of-plane spin component (right panel). The in-plane spin is indicated by black arrows and the out-of-plane spin by color. Black lines are constant energy contours. Both figures are based on analytical solutions of the model Hamiltonian for Bi_2Se_3 (see section 3.2). The right panel shows only the lower part of the Dirac cone.

larger bulk gap than $\text{Bi}_x\text{Sb}_{1-x}$ and can be produced at a higher quality because they are compounds instead of alloys [17]. Where $\text{Bi}_x\text{Sb}_{1-x}$ has multiple, topological and non-topological, surface states, these materials have only a single Dirac cone at the Γ -point. Especially Bi_2Se_3 has surface states that form a nearly ideal Dirac cone, like in Fig. 2.2, with the spin lying mainly in the surface plane and locked orthogonal to the momentum [38, 39]. The spin therefore rotates around the Fermi surface because time-reversal symmetry again requires that states with opposite momentum have opposite spin [17]. Besides, some materials, especially Bi_2Te_3 [40, 41], show a hexagonal deformation of the Dirac cone along with an out-of-plane spin component (Fig. 2.2). Like in the 2D case, scattering into states with opposite spin is forbidden when time-reversal symmetry is preserved. As the electron wave-function acquires a minus sign, i.e. a π Berry phase, when it is adiabatically transported around the Fermi surface, different reflection paths interfere destructively. This applies, however, only to a direct reversal of the spin. Since there are now surface states with intermediate spin orientations, scattering into these states is possible even by non-magnetic perturbations, even though such perturbations cannot destroy the topological surface states. This leads to diffusive surface transport, where a reversal of the initial electron spin is possible through multiple scattering events [17]. The locking of spin and momentum has been demonstrated in multiple spin-resolved ARPES (SARPES) measurements, however with strongly varying values for the degree of the spin-

polarization in the range of about 45%-100% [38, 39, 42, 43].

The simple band structure, which allows theoretical modeling by a simple Hamiltonian [32, 44] (see section 3.1), and the large bulk gap of up to $\sim 0.3\text{eV}$ in Bi_2Se_3 [32], potentially enabling room temperature applications, established materials of the Bi_2Se_3 class as prototypical 3D TIs. Since they grow in only weakly coupled quintuple-layers (QL) of about 1nm, they can be produced in very smooth thin films down to a single QL by molecular beam epitaxy [37, 45, 46]. This is very important for transport measurements and potential applications in spintronics. While calculations predict that the Fermi level resides inside the bulk gap, this is in most cases not true for real samples because of imperfections that result in intrinsic doping. Especially the surface Fermi level changes with time when exposed to air. Therefore, the Fermi level is often even different for the bulk and the surface, resulting in bulk conductivity even when the Fermi level in ARPES measurements seems to be in the bulk gap. Partly, this can be compensated by individual chemical doping of bulk and surface with nonmagnetic dopants, but fine-tuning is difficult. In thin layers, however, the overall impact of bulk carriers is reduced and the Fermi level can be fine-tuned by a gate voltage [17, 25].

Interestingly, when the thickness of these TIs is decreased down to the spatial extend of the surface states at the top and bottom surface (below 6QL for Bi_2Se_3 [46] and 5QL for Sb_2Te_3 [37]), also a QSH state can be realized in these materials [47–49]. When the surface states from top and bottom surface overlap, they hybridize and open a gap in the surface state dispersion, which increases with decreasing thickness [46]. Then, as long as the thickness remains above a certain threshold, the material remains topologically nontrivial and features 1D edge states inside the hybridization gap. For Bi_2Se_3 , this threshold is 3nm (3QL) [48], where the hybridization gap measured by ARPES already has a size of about 138meV [46]. Even though this is more than an order of magnitude larger than the gap size of the order of 10meV [15] in HgTe quantum wells, it may still be too small for room temperature applications. However, proof of principle measurements at moderate temperatures should be possible. Other newly predicted 2D materials reach even larger gap sizes, similar to or larger than that of bulk Bi_2Se_3 [50, 51].

When magnetic ordering is introduced into a TI, e.g. by doping with transition metal atoms or by proximity to a ferromagnetic material, time-reversal symmetry is broken, and the surface states are no longer topologically protected. But then, other interesting effects can be created. Magnetic moments with anisotropy perpendicular to the surface of the TI induce a ferromagnetic exchange field in the same direction and open a gap in the surface state dispersion. If the Fermi level lies inside this gap, this results in an insulating massive Dirac fermion state, which may allow observation of many interesting effects [52]. A ferromagnetic exchange field parallel to the surface, on the other hand, may cause a transition into a Weyl semi-metal, where a flat surface band spans between two Dirac points [53, 54]. Particularly interesting effects arise when magnetic ordering is introduced into 2D TIs. In that case, an out-of-plane exchange field causes a transition into another topologically different state, the quantum anomalous Hall (QAH) state.

2.2 Quantum anomalous Hall effect

The QAH state is very similar to the QH state because it features quantized, but now spin polarized topologically protected chiral edge states in an insulating gap. However, like the QSH state it does not need an external magnetic field even though it requires breaking of time-reversal symmetry. Instead, it relies on the intrinsic spin-orbit coupling. In fact, the QSH state can be viewed as two copies of the QAH state connected by time-reversal symmetry [55]. Because of this, the QAH effect was proposed to be observable in 2D ferromagnetic TIs [18, 19].

Magnetic dopants with out-of-plane orientation induce a ferromagnetic exchange field in the TI that acts as an additional mass term in the Hamiltonian, with opposite sign for the two copies of the QAH state. The sign of the mass term defines whether or not the bands are inverted, and its absolute value corresponds to half the gap size at zero momentum. So, when the exchange field is increased, the gap of one state widens while the other one shrinks. If the field is strong enough, this results in a band inversion for the one state, i.e. a phase transition into a topologically trivial state, while the other one remains nontrivial. Which of the two states remains, and consequently the propagation direction and spin of the edge states, is determined by the sign of the exchange field [18, 19].

The QAH state was first proposed to exist in Mn doped HgTe quantum wells [18]. However, an additional Zeeman field is needed to polarize the magnetic dopants, because they do not order spontaneously. This makes it difficult to distinguish the QAH effect from the QH effect. Later, the QAH effect was also proposed for thin films of the new Bi₂Se₃ class of 3D TIs [19]. In addition to a potentially larger gap in the 2D state, the magnetic moments order spontaneously with out-of-plane anisotropy in these materials [56]. A few years after the theoretical prediction, the QAH state was observed in Cr and V doped (Bi,Se)₂Te₃, with a quantized Hall conductance of $\sigma_{xy} \approx e^2/h$ at temperatures of the order of a few 10mK [20, 56, 57]. This temperature, however, is about two orders of magnitude smaller than the Curie temperature and also much smaller than the predicted ferromagnetic excitation gap in the edge state dispersion. Most likely, this is due to an overlap of the Dirac point with the bulk valence band, resulting in a largely reduced effective excitation gap [57, 58]. According to Qi *et al.* [59], the problem is that doping with a single element reduces the size of the bulk gap, which could be overcome by codoping of (Bi,Se)₂Te₃ with I and V. They calculate a Curie temperature of about 50K and an excitation gap of at least ~ 50 meV for a film thickness of 5QL.

Another way to introduce ferromagnetism into a TI is by proximity to a ferromagnetic insulator (FMI) like EuS [60–62]. This has advantages as well as disadvantages. As the FMI forms a very clean interface with the TI, no magnetic impurities are injected into the TI so that the bulk properties of the TI should remain basically unaffected. Besides, it was recently shown by Katmis *et al.* [62] that a Bi₂Se₃/EuS bilayer structure can retain a finite magnetization for temperatures larger than 300K. EuS alone has a Curie temperature of about 17K, i.e. the TI stabilizes the FMI. A problem for some applications, like the QAH effect, could be that EuS has in-plane anisotropy, which leads to an out-of-plane anisotropy in the surface of Bi₂Se₃ due to strong spin-orbit coupling. Still, there is also a finite in-plane component in Bi₂Se₃,

which becomes smaller as the thickness of the layers is decreased [62]. However, the biggest problem is that, up to now, the theoretical excitation gap ($\sim 7\text{meV}$) is much smaller than with magnetic doping [61]. The penetration depth of the proximity field is about $1\text{nm}-2\text{nm}$ [61, 62], which may be enough to turn thin TI films of $3\text{nm}-6\text{nm}$ into the QAH state, especially in a sandwich structure with FMs above and below the TI. Another advantage of the proximity effect in hindsight of device structures discussed in this thesis is that it is potentially easier to apply exchange fields that are locally restricted.

2.3 Spintronic

In conventional electronics, information is only carried by the charge of electrons. So, there are only two states, charge (transport) or no charge (transport). Spintronics, on the other hand, includes or solely uses the spin degree of freedom. This enables new device concepts with increased functionality and decreased power consumption, but it requires engineering of new materials and methods. In many cases, spintronic devices can be divided into generation, transport and detection of spins, where the different aspects usually require different materials [3, 4]. Materials with strong spin-orbit coupling can act as generators and detectors, while those with weak spin-orbit coupling are good at conserving the spin [9]. In TIs, the locking of spin and momentum in surface or edge states promises both, efficient generation of spin currents as well as long spin-diffusion lengths. Spin diffusion lengths of $\sim 2\mu\text{m}$ have been reported for HgTe quantum wells [29, 63].

The field of spintronics began with the discovery of the giant magnetoresistance (GMR) effect in heterostructures of two ferromagnetic layers separated by a thin nonmagnetic conductor [3]. Depending on the relative magnetic orientation of the two magnetic layers, the resistance of the heterostructure is either high (antiparallel) or low (parallel) because the polarized current coming from one ferromagnet is largely reflected by the other one in an antiparallel orientation. Even larger changes in resistance can be achieved with the tunneling magnetoresistance (TMR) effect, where the nonmagnetic conducting layer is replaced by an insulating layer [4]. This effect is based on quantum tunneling through the insulating layer, which has better spin conserving properties. Both GMR and TMR effect are of great technological importance as they find application in read heads of hard disk drives and in non-volatile magnetoresistive random access memory (MRAM) [3]. Due to the spin-momentum locking in topological surface states, a spin-polarized current injected into the surface will flow into a certain direction, leading to a direction dependent resistance. Thus, similar effects can also be achieved in heterostructures of TIs and ferromagnets [2, 64, 65].

In GMR and TMR devices, ferromagnets are used to polarize electrons, but it also works the other way around. Currents of spin polarized electrons can transfer angular momentum to a ferromagnet and thereby change its magnetization [3, 4, 66]. This effect, known as spin-transfer torque, is of great current interest for all electrical switching of ferromagnetic domains in spin-transfer torque MRAM (STT-MRAM) because it promises low power consumption and good scalability and switching times [6]. Currently, the spin polarized currents for the switching of STT-MRAM are generated by ferromagnets [6, 67], but the search for more efficient methods goes on. One suggestion are TIs [12], and it has already been shown for TI/ferromagnet [10]

2 Thematic background

and TI/ferromagnetic TI [68] bilayers that the spin-transfer torque generated by TIs is strong.

Since in many cases, the charge of a spin current is not needed, the generation of pure spin currents without a net charge current is of great interest. A pure spin current produces no magnetic field and the Joule heating is usually reduced [66]. While there are already a few methods to produce pure spin currents, their efficiency is usually low. The most prominent method, the spin Hall effect, where a current through a nonmagnetic 2D conductor produces a traverse spin voltage due to spin-orbit coupling, reaches only charge spin conversion efficiencies of about 10% [66, 69]. The inverse spin Hall effect, i.e. the creation of a charge current as a result of a spin voltage, is often used for the detection of spin currents, with the same poor efficiency [66, 69]. Other methods for creating pure spin currents are the Spin Seebeck effect [70] and spin pumping [71]. In TIs, every charge current is also a spin current, where currents flowing in opposite directions carry opposite spin. So, when charge currents of equal magnitude are driven in both directions, the charge currents cancel, but the spin currents add to a pure spin current. As the charge currents are directly transferred into spin currents, this promises to be very efficient. The investigation of how pure spin currents can be created, switched and detected in 2D TIs with local ferromagnetic exchange fields is therefore at the heart of chapter 4.

Whenever ferromagnets or TIs are involved in spintronic devices, the efficiency of the devices depends on the polarization strength of the ferromagnets and the topological surface or edge states. It is therefore crucial to get accurate quantitative values for the spin polarization. A widely used method for the determination of the spin polarization is SARPES, where the spin polarization is determined from the polarization of photoelectrons. However, in the case of TIs, SARPES measurements show no uniform result [38, 39, 42, 43]. Another way of measuring spin polarizations is quantum tunneling between different polarized materials. Meservey and Tedrow developed a method that utilizes the quasiparticle splitting in thin films of superconducting aluminum in a strong parallel magnetic field for measuring the polarization of ferromagnets [21, 22]. How this method can be applied to TIs is examined in chapter 5. This method, however, is limited to measuring the in-plane spin component. Therefore, another approach, called spin Hall effect tunneling spectroscopy [23, 24], that uses tunneling from ferromagnets is considered for measuring the out-of-plane component in chapter 6.

3 Model Hamiltonian

There are currently two prototypical classes of TI materials that are often considered in model calculations as they were the first materials found to be TIs and in most cases have a simple band structure. CdTe/HgTe/CdTe quantum wells, which become a 2D TI beyond a critical thickness of the HgTe layer, were the first material in which the QSH effect was measured [26]. They can be described by a simple model Hamiltonian [15], but the small bulk gap of the order of 10meV [15] significantly reduces the applicability in spintronic applications. Besides, the QAH state, which is one of the main material requirements in this thesis, cannot easily be achieved in HgTe quantum wells. The QAH state is proposed to exist in Mn doped HgTe, but as the magnetic moments of the donor atoms do not order spontaneously, a small additional magnetic field is needed to induce magnetic order [18].

Materials belonging to the Bi_2Se_3 class (Bi_2Se_3 , Sb_2Te_3 , Bi_2Te_3 , etc.) are 3D TIs in the first place but can feature one-dimensional edge states in the thin film limit [48, 49]. So, a corresponding model can be used for 2D and 3D calculations. These materials are also much more attractive for spintronic applications. The large bulk gaps of up to $\sim 0.3\text{eV}$ [32] potentially allow room temperature application, and a QAH phase has already been observed in thin films of these materials [20, 56, 57]. When doped with transition metal atoms, these TIs enter a QAH phase without the need of an additional Zeeman field because they are ferromagnetic with out-of-plane anisotropy [56]. For these reasons, calculations in this thesis are based on a model Hamiltonian for the Bi_2Se_2 class of materials, which is presented in the following sections.

3.1 Effective model for the Bi_2Se_3 class of 3D TIs

A model Hamiltonian for the Bi_2Se_3 class of materials has been derived by Liu *et al.* [44] by symmetry principles and $\mathbf{k} \cdot \mathbf{p}$ perturbation theory. Considering Bi_2Se_3 as an example, the crystal consist of alternating Bi and Se layers that are stacked along the c -axis. Inside every layer, the lattice is hexagonal, while the whole crystal has a rhombohedral crystal structure with space group $D_{3d}^5 (R\bar{3}m)$. Five layers of the crystal, i.e. three Bi and two Se layers, form a so called quintuple layer (QL) with strong chemical bonding inside the QL. Different QLs are only weakly coupled through the van der Waals force. A unit cell consist of three differently oriented QLs in c -direction [44]. Due to the weak coupling of individual QLs, Bi_2Se_3 and other materials of the class can be produced with good precision down to about 1nm, i.e. one QL, using molecular beam epitaxy [37, 45].

The four band model of Liu *et al.* [44] considers the two most important hybrid orbitals of Bi and Se near the Fermi level. To get these orbitals, they start from the atomic orbitals of Bi ($6s^26p^3$) and Se ($4s^24p^4$) and successively take into account different interaction terms. As

3 Model Hamiltonian

the outermost shells of both Bi and Se are p orbitals, only the p orbitals of the five atoms within one QL are considered. The layered arrangement of Bi and Se atoms then causes a level repulsion so that Bi states are raised in energy while Se states are lowered. Inversion symmetry of the system allows to write these states in terms of bonding and anti-bonding states, of which the Bi states $|P1^+, \alpha\rangle$ and the Se states $|P2^-, \alpha\rangle$ are closest to the Fermi level. Here, \pm denotes the parity and $\alpha = p_x, p_y, p_z$ the different p orbitals. As the z -direction is different from the x - and y -direction in this layered system, these states split further so that valence and conduction band are formed by the p_z -orbitals. When spin-orbit coupling is taken into account, these bands are inverted at the Γ -point of the first Brillouin zone, and, due to the different parity of the inverted bands, the material is a topological insulator. The four states $|P1_z^+, \sigma\rangle$ and $|P2_z^-, \sigma\rangle$, where $\sigma = \uparrow, \downarrow$ denotes the spin in the σ_z basis, can thus be taken as a basis for the model Hamiltonian. Due to time-reversal symmetry, spin-up and spin-down states have to be degenerate at any time-reversal invariant momenta.

By invoking the crystal symmetries, Liu *et al.* [44] end up with the following Hamiltonian in third order of momentum \mathbf{k} :

$$H_{\text{eff}} = H_0 + H_3 \quad (3.1)$$

with

$$H_0 = \epsilon_{\mathbf{k}} + \mathcal{M}(\mathbf{k}) \Gamma^4 + \mathcal{B}(k_z) \Gamma^3 k_z + \mathcal{A}(k_{\parallel}) (\Gamma^1 k_y - \Gamma^2 k_x), \quad (3.2)$$

$$H_3 = R_1 \Gamma^5 (k_x^3 - 3k_x k_y^2) + R_2 \Gamma^3 (3k_x^2 k_y - k_y^3). \quad (3.3)$$

The coefficients are given by $\epsilon_{\mathbf{k}} = C_0 + C_1 k_z^2 + C_2 k_{\parallel}^2$, $\mathcal{M}(\mathbf{k}) = M_0 + M_1 k_z^2 + M_2 k_{\parallel}^2$, $\mathcal{A}(k_{\parallel}) = A_0 + A_2 k_{\parallel}^2$, and $\mathcal{B}(k_z) = B_0 + B_2 k_z^2$, where $k_{\parallel}^2 = k_x^2 + k_y^2$. In the basis

$$(1 \uparrow, 1 \downarrow, 2 \uparrow, 2 \downarrow)^T, \quad (3.4)$$

which is a short form for the basis given above, the Dirac Γ -matrices read

$$\Gamma^{1,2,3,4,5} = (\tau_1 \otimes \sigma_1, \tau_1 \otimes \sigma_2, \tau_2 \otimes \mathbb{I}_{2 \times 2}, \tau_3 \otimes \mathbb{I}_{2 \times 2}, \tau_1 \otimes \sigma_3). \quad (3.5)$$

The Pauli matrices τ_i and σ_i act in the orbit- and spin-space, respectively. Note that, compared to Ref. [44], the order of spin and orbital degrees of freedom has been changed. $\mathcal{M}(\mathbf{k})$ describes the momentum dependent gap for a particle hole symmetric case, where M_0 is half the gap size at $\mathbf{k} = 0$. A particle hole asymmetry is introduced by the term $\epsilon_{\mathbf{k}}$, where C_0 defines the Fermi level. $\mathcal{A}(k_{\parallel})$ and $\mathcal{B}(k_z)$ are spin-orbit coupling terms. They enable transitions between the two otherwise decoupled orbitals. H_3 contains only third order spin-orbit coupling terms and breaks the in-plane rotation symmetry along the z -direction down to a threefold rotation symmetry.

Parameters for this model Hamiltonian are obtained by Liu *et al.* [44] by applying $\mathbf{k} \cdot \mathbf{p}$ perturbation theory to the wave functions at the Γ point, obtained from *ab initio* calculations. They list parameters for Bi_2Se_3 , Sb_2Te_3 and Bi_2Te_3 , but only those for Bi_2Se_3 and Sb_2Te_3 will

3.1 Effective model for the Bi_2Se_3 class of 3D TIs

	Bi_2Se_3 (a) [44]	Sb_2Te_3 [44]	Bi_2Se_3 (b) [32]
A_0 (eVÅ)	3.33	3.40	4.1
B_0 (eVÅ)	2.26	0.84	2.2
C_0 (eV)	-0.0083	0.001	-0.0068
C_1 (eVÅ ²)	5.74	-12.39	1.3
C_2 (eVÅ ²)	30.4	-10.78	19.6
M_0 (eV)	-0.28	-0.22	0.28
M_1 (eVÅ ²)	6.86	19.64	-10
M_2 (eVÅ ²)	44.5	48.51	-56.6
R_1 (eVÅ ³)	50.6	103.2	-
R_2 (eVÅ ³)	-113.3	-244.67	-

Table 3.1: List of parameters for the model Hamiltonian Eq. (3.1). Parameters in the first two rows are directly taken from Ref. [44], while those in the third row are adjusted to fit the conventions of Eq. (3.1). They belong to a version of the Hamiltonian that is only of second order in momentum \mathbf{k} , which is why R_1 and R_2 are missing.

be used here (see table 3.1). Parameters for Bi_2Te_3 are not used because the model Hamiltonian, which strictly speaking is only valid for small \mathbf{k} , in that case shows no gap for large k_z . Third order spin-orbit coupling terms, i.e. term proportional to A_2 and B_2 , have already been neglected in Ref. [44] and are therefore missing here as well. The lattice constants of Bi_2Se_3 are $a \approx 4.14\text{Å}$ and $c \approx 28.64\text{Å}$ and of Sb_2Te_3 $a \approx 4.25\text{Å}$ and $c \approx 30.35\text{Å}$ [72].

After a unitary transformation [44]

$$U_1 = \begin{pmatrix} 1 & 0 & 0 & 0 \\ 0 & 1 & 0 & 0 \\ 0 & 0 & -i & 0 \\ 0 & 0 & 0 & i \end{pmatrix} \quad (3.6)$$

and neglecting third order terms, this Hamiltonian coincides with another Hamiltonian published prior to this by the same authors in Ref. [32]. In the same publication, they give a different set of parameters for Bi_2Se_3 (see table 3.1), obtained by fitting the model to *ab initio* band structure calculations. Even though these parameters may have some ambiguities due to the fitting [44], they will be used along with the other parameters. For the case of a tetragonal lattice, where the H_3 term will be neglected, the model parameters for the Hamiltonian containing only second order terms may be more appropriate. Unfortunately, only parameters for Bi_2Se_3 are given in that publication. For Sb_2Te_3 , the parameters of the third order Hamiltonian are used even if the H_3 term is neglected.

Because the spin matrices

$$S_x = \frac{1}{2}\mathbb{I}_{2 \times 2} \otimes \sigma_1, \quad S_y = \frac{1}{2}\mathbb{I}_{2 \times 2} \otimes \sigma_2, \quad S_z = \frac{1}{2}\mathbb{I}_{2 \times 2} \otimes \sigma_3 \quad (3.7)$$

3 Model Hamiltonian

are not generally invariant under unitary transformations, the spin in the Hamiltonian does not necessarily coincide with the real electron spin. According to Ref. [44, 73], Eq. (3.1) contains the real spin, i.e. Eq. (3.7) is valid, while the spin in the other Hamiltonian is a pseudo spin. In that case, the real electron spin is given by $S_x = \frac{1}{2}\tau_3 \otimes \sigma_1$, $S_y = \frac{1}{2}\tau_3 \otimes \sigma_2$ and $S_z = \frac{1}{2}\mathbb{I}_{2 \times 2} \otimes \sigma_3$ [73]. Pseudo spin and real spin are therefore equal for the first orbital and connected by a π rotation around the z -axis for the second orbital. Only S_z is invariant under this transformation.

Since the model Hamiltonian Eq. (3.1) contains the real electron spin, a ferromagnetic exchange field of strength $\mathbf{V} = (V_x, V_y, V_z)$ can be introduced by a Zeeman term of the form

$$H_Z = \sum_{i=1}^3 V_i \mathbb{I}_{2 \times 2} \otimes \sigma_i = \mathbb{I}_{2 \times 2} \otimes (\mathbf{V} \cdot \boldsymbol{\sigma}) \quad (3.8)$$

with $\boldsymbol{\sigma} = (\sigma_1, \sigma_2, \sigma_3)$.

3.1.1 Tight-binding-approximation

The main concept of a tight-binding-approximation is that electrons are strongly bound to the atomic potentials at individual lattice sites. In that case, at least the low lying energy levels are well approximated by the atomic potentials, and only the outermost electron orbitals contribute to the chemical bonding of the crystal. The interaction of these atomic electron states causes the degenerate atomic energy levels to split into bonding and anti-bonding states. For the large amount of atoms in the lattice, this results in a continuous dispersion (energy bands) and allows electrons to travel from atom to atom [74].

A single electron real space tight-binding Hamiltonian in second quantization can in a general form be written as

$$H = \sum_{i,a,a',\sigma,\sigma'} \epsilon_{iaa'\sigma\sigma'} d_{ia\sigma}^\dagger d_{ia'\sigma'} + \sum_{i,j,a,a',\sigma,\sigma'} t_{ijaa'\sigma\sigma'} d_{ia\sigma}^\dagger d_{ja'\sigma'}, \quad (3.9)$$

where i and j are lattice indices, a and a' orbital indices and σ and σ' spin indices. The operator $d_{ia\sigma}$ removes an electron with spin σ from orbital a at lattice site i , while $d_{ia\sigma}^\dagger$ creates an electron with the same properties. Local energies $\epsilon_{iaa'\sigma\sigma'}$, like energy splitting of different orbitals or spins and constant energy shifts, are given by the first term in Eq. (3.9). This term can also include electrostatic potentials or ferromagnetic exchange fields. The second term describes hopping processes between different lattice sites with transition matrix elements $t_{ijaa'\sigma\sigma'}$, originating from the overlap of the electron state of position i with the potential and electron state of position j . Due to the strongly localized atomic states, it is in most cases sufficient to run the second sum only over nearest neighbors or at most next nearest neighbors [74].

In the case of periodic boundary conditions and translational invariance, the Hamiltonian can be transformed into momentum space by transforming the operators $d_{ia\sigma}$ into Bloch functions

$$d_{ia\sigma} = \frac{1}{\sqrt{N}} \sum_{\mathbf{k}} e^{i\mathbf{k}\mathbf{R}_i} c_{\mathbf{k}a\sigma}. \quad (3.10)$$

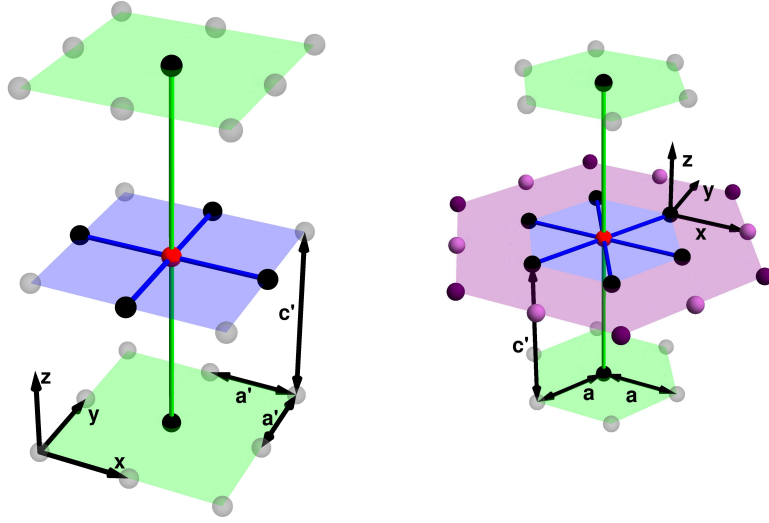


Figure 3.1: Lattice structure of the two lattice approximations used in this thesis. In the tetragonal lattice (left panel), a lattice site (red dot) is coupled to six nearest neighbors (black dots). Coupling is isotropic within one layer (blue) and has an anisotropy in z -direction (green). In the hexagonal lattice (right panel), there are six nearest (black) and twelve next nearest (purple) neighbors within one layer. While coupling to the nearest neighbors is isotropic, coupling to next nearest neighbors is different along different crystal axes, which is indicated by different shades of purple. Lattice constants $a' = a \cdot \sqrt{\frac{\sqrt{3}}{2}}$ and $c' = \frac{c}{15}$ are effective versions of the real lattice constants.

Here, \mathbf{R}_i is a basis vector of the crystal, N the number of lattice sites and the operator $c_{\mathbf{k}a\sigma}$ removes an electron with momentum \mathbf{k} and spin σ from orbital a . \mathbf{k} runs over all wave vectors of the first Brillouin zone, with a discretization defined by the lattice. If periodic boundary conditions and translational invariance are only given for some crystal axes, one can still use a mixed representation of the Hamiltonian in real and momentum space, e.g. to describe a system that has an interface in one direction but can be considered translational invariant in other directions.

Depending on whether or not the sign of $t_{ijaa'\sigma\sigma'}$ changes when interchanging i and j , the summands of the second sum translate into terms that are odd or even in $k_{i=x,y,z}$, respectively. Odd terms couple orbital states with different parity, while even or constant terms couple those with the same parity. The exact form is a matter of the underlying lattice. Here, two different approximations of the real TI lattice are used.

3.1.2 Tetragonal lattice

The simplest approximation of the TI lattice is a tetragonal lattice with z -anisotropy (see Fig. 3.1). It has all symmetries of the original crystal structure except for the threefold rotation symmetry around the z -axis, which enters only in third order into the Hamiltonian and is neglected in this approximation. A lattice regularized version of the Hamiltonian given in Ref. [32] has been given by Li *et al.* [75]. After adapting it to the conventions of the Hamiltonian Eq. (3.1), it reads

$$H(\mathbf{k}) = \epsilon_0(\mathbf{k}) \mathbb{I}_{4 \times 4} + \sum_{i=1}^4 m_i(\mathbf{k}) \Gamma^i, \quad (3.11)$$

where the coefficients are given by

$$\epsilon_0(\mathbf{k}) = C_0 + 2C_1(1 - \cos k_z) + 2C_2(2 - \cos k_x - \cos k_y), \quad (3.12)$$

$$m_1(\mathbf{k}) = A_0 \sin k_y, \quad (3.13)$$

$$m_2(\mathbf{k}) = -A_0 \sin k_x, \quad (3.14)$$

$$m_3(\mathbf{k}) = B_0 \sin k_z, \quad (3.15)$$

$$m_4(\mathbf{k}) = M_0 + 2M_1(1 - \cos k_z) + 2M_2(2 - \cos k_x - \cos k_y). \quad (3.16)$$

For the tetragonal lattice, the lattice regularization is achieved by simply replacing k with $\sin k$ and k^2 with $2(1 - \cos k)$. In the lattice regularized Hamiltonian, all wave vectors are normalized to the lattice constants. Consequently, all material parameters are normalized as well and have the dimension of an energy. All x - and y - parameters (A_0 , C_2 and M_2) are divided by powers of $a' = a \cdot \sqrt{\frac{\sqrt{3}}{2}}$ and all z -parameters (B_0 , C_1 and M_1) by powers of $c' = \frac{c}{15}$. a' and c' are effective lattice constants, where a' is chosen such that the size of the first Brillouin zone of the 2D square lattice matches that of the actual hexagonal lattice. c' is the mean atomic distance in a unit cell with lattice constant c , consisting of 15 layers. As the reciprocal lattice of a tetragonal lattice is tetragonal as well, all wave vectors in the first Brillouin zone run from $-\pi$ to π in steps of $\Delta k_i = \frac{2\pi}{N_i}$.

Equation (3.11) is written in terms of 4×4 matrices. However, it can also be expressed in terms of pairs of creation and annihilation operators, $c_{\mathbf{k}a\sigma}^\dagger$ and $c_{\mathbf{k}a\sigma}$. When applied to a vector, the matrix element m_{ij} acts as an annihilation operator on the j th vector element and as a creation operator for the i th element of the new vector, i.e. $m_{ij} = c_i^\dagger c_j$. The basis Eq. (3.4) assigns orbital and spin indices, a and σ , to the matrix indices i and j .

Then, by performing the inverse transformation to Eq. (3.10) [29]

$$c_{\mathbf{k}a\sigma} = \frac{1}{\sqrt{N}} \sum_{i=0}^{N-1} e^{-i\mathbf{k}\mathbf{R}_i} d_{ia\sigma}, \quad (3.17)$$

this Hamiltonian can be (partly) transformed into real space. A partial transformation of a

3.1 Effective model for the Bi_2Se_3 class of 3D TIs

cosine term is shown in the following for $\cos k_y$, i.e. after the transformation, the Hamiltonian is in real space for the y -direction. x - and z -direction remain in momentum space. The reduced 2D momentum vector is denoted as $\tilde{\mathbf{k}} = (k_x, k_z)$, and N_y is the number of lattice sites in y -direction. Transfer matrix elements t , orbitals a and a' as well as spins σ and σ' are kept unspecified because the transformation is independent of them. The indices i and j run over all lattice sites in y -direction and \mathbf{k} and $\tilde{\mathbf{k}}$ over all discrete momenta of the 3D or 2D first Brillouin zone, respectively.

$$\begin{aligned}
& t \sum_{\mathbf{k}} \cos k_y c_{\mathbf{k}a'\sigma'}^\dagger c_{\mathbf{k}a\sigma} \\
&= t \frac{1}{N_y} \sum_{\mathbf{k}, i, j} e^{ik_y(y_i - y_j)} \cos k_y d_{\mathbf{k}ia'\sigma'}^\dagger d_{\tilde{\mathbf{k}}ja\sigma} \\
&= \frac{t}{2} \frac{1}{N_y} \sum_{\mathbf{k}, i, j} \left(e^{ik_y(y_i - y_j + 1)} + e^{ik_y(y_i - y_j - 1)} \right) d_{\mathbf{k}ia'\sigma'}^\dagger d_{\tilde{\mathbf{k}}ja\sigma} \\
&= \frac{t}{2} \sum_{\tilde{\mathbf{k}}, i, j} (\delta_{i, j-1} + \delta_{i, j+1}) d_{\mathbf{k}ia'\sigma'}^\dagger d_{\tilde{\mathbf{k}}ja\sigma} \\
&= \frac{t}{2} \sum_{\tilde{\mathbf{k}}, j} \left(d_{\tilde{\mathbf{k}}(j-1)a'\sigma'}^\dagger d_{\tilde{\mathbf{k}}ja\sigma} + \text{h.c.} \right)
\end{aligned}$$

In the third step, the completeness relation $\frac{1}{N} \sum_{\mathbf{k}} e^{ik(i-j)} = \delta_{ij}$ has been used. So, after the transformation, every cosine term is transformed into nearest neighbor hopping terms along the direction defined by the momentum. An analogous calculation for $\sin k_y$ yields

$$\begin{aligned}
& t \sum_{\mathbf{k}} \sin k_y c_{\mathbf{k}a'\sigma'}^\dagger c_{\mathbf{k}a\sigma} \\
&= \frac{t}{2i} \sum_{\tilde{\mathbf{k}}, i, j} (\delta_{i, j-1} - \delta_{i, j+1}) d_{\mathbf{k}ia'\sigma'}^\dagger d_{\tilde{\mathbf{k}}ja\sigma} \\
&= i \frac{t}{2} \sum_{\tilde{\mathbf{k}}, j} \left(d_{\tilde{\mathbf{k}}(j+1)a'\sigma'}^\dagger d_{\tilde{\mathbf{k}}ja\sigma} - \text{h.c.} \right).
\end{aligned}$$

Here, the sign of the hopping term is different for different movement directions. Momentum independent terms simply transform as

$$t \sum_{\mathbf{k}} c_{\mathbf{k}a'\sigma'}^\dagger c_{\mathbf{k}a\sigma} = t \sum_{\tilde{\mathbf{k}}, j} d_{\tilde{\mathbf{k}}ja'\sigma'}^\dagger d_{\tilde{\mathbf{k}}ja\sigma}. \quad (3.18)$$

When the Hamiltonian is completely transformed into real space, each lattice site (red dot in Fig. 3.1) is coupled to six nearest neighbors, where the coupling parameters for x - and y -direction differ from those for the z -direction. Up to now, the lattice has still periodic boundaries, i.e. the lattice sites $N - 1$ and 0 for a given spatial direction are linked. A surface can

3 Model Hamiltonian

be introduced by simply breaking this connection.

After transformation into real space, the Hamiltonian can be rewritten as a $4N \times 4N$ matrix, where each of the N real space lattice sites is represented by a 4×4 (momentum dependent) sub-matrix, which represents the orbital and spin degrees of freedom, a and σ . As the Hamiltonian involves only nearest neighbor hopping, the matrix is a band matrix in the case of open boundary conditions.

In a sufficiently thin film, where the surface states of the top and bottom surface are gapped out, the 3D Hamiltonian can be approximated by an effective 2D Hamiltonian, where k_z is replaced by its mean value $\langle k_z \rangle$. If the confining potential is symmetric, the mean value is $\langle k_z \rangle = 0$, and therefore, terms proportional to C_1 , M_1 and B_0 drop out in the effective 2D Hamiltonian [55]. Paananen *et al.* [53] further introduced an effective 2D mass term

$$M_{2D} = M_0 + M_1 \left(\frac{\pi}{L_z} \right)^2, \quad (3.19)$$

where L_z is the film thickness. This term reduces the size of the bulk gap in thin films and eventually, when the film is reduced below a critical thickness, causes a phase transition into a topologically trivial state.

3.1.3 Hexagonal lattice

As a second approximation of the real TI lattice, a hexagonal lattice is chosen, which respects all symmetries of the TI crystal, including the threefold rotation symmetry around the z -axis. When the lattice axes are chosen according to the right panel of Fig. 3.1, the Hamiltonian reads [2]

$$H(\mathbf{k}) = \epsilon_0(\mathbf{k}) \mathbb{I}_{4 \times 4} + \sum_{i=1}^4 m_i(\mathbf{k}) \Gamma^i + \mathcal{R}_1(\mathbf{k}) \Gamma^5 + \mathcal{R}_2(\mathbf{k}) \Gamma^3 \quad (3.20)$$

with coefficients

$$\begin{aligned} \epsilon_0(\mathbf{k}) &= C_0 + 2C_1(1 - \cos k_z) + \frac{4}{3}C_2 \left(3 - 2 \cos \frac{1}{2}k_x \cos \frac{\sqrt{3}}{2}k_y - \cos k_x \right), \\ m_1(\mathbf{k}) &= A_0 \frac{2}{\sqrt{3}} \cos \frac{1}{2}k_x \sin \frac{\sqrt{3}}{2}k_y, \\ m_2(\mathbf{k}) &= -A_0 \frac{2}{3} \left(\sin \frac{1}{2}k_x \cos \frac{\sqrt{3}}{2}k_y + \sin k_x \right), \\ m_3(\mathbf{k}) &= B_0 \sin k_z, \\ m_4(\mathbf{k}) &= M_0 + 2M_1(1 - \cos k_z) + \frac{4}{3}M_2 \left(3 - 2 \cos \frac{1}{2}k_x \cos \frac{\sqrt{3}}{2}k_y - \cos k_x \right). \end{aligned}$$

Here, the coefficients $\epsilon_0(\mathbf{k})$ and $m_1(\mathbf{k})$ - $m_4(\mathbf{k})$ have been adapted from Ref. [76] to fit the chosen lattice orientation and the parametrization of Liu *et al.* [44]. Material parameters and momenta are now normalized with respect to the lattice constants a and $c' = \frac{c}{15}$. After transformation into real space, analogous to the previous section, these coefficients are hopping terms to nearest neighbors, symbolized by black dots in Fig. 3.1. Again, the coupling strength to all lattice sites within one layer is the same and differs from that to neighbors in other layers.

For the coefficients $\mathcal{R}_1(\mathbf{k})$ and $\mathcal{R}_2(\mathbf{k})$, which are third order terms to lowest order in momentum, no lattice regularized versions were given in Ref. [76]. They can be written as [2]

$$\mathcal{R}_1(\mathbf{k}) = 2R_1 \left(\cos \sqrt{3}k_y - \cos k_x \right) \sin k_x,$$

$$\mathcal{R}_2(\mathbf{k}) = \frac{16}{3\sqrt{3}}R_2 \left(\cos \frac{\sqrt{3}}{2}k_y - \cos \frac{3}{2}k_x \right) \sin \frac{\sqrt{3}}{2}k_y.$$

In real space, they represent couplings to two different sets of next nearest neighbors (purple dots) within one layer. Neighbors represented by $\mathcal{R}_1(\mathbf{k})$ have a darker color than those represented by $\mathcal{R}_2(\mathbf{k})$.

3.2 Analytical dispersion and surface states

In this section, (approximate) analytical solutions of the eigenvalue problem for the two lattices are given. These solutions give insight into some quantities like bulk gap and surface state dispersion and polarization. Besides, the analytical surface state approximation for the hexagonal lattice is the basis for the derivation of the Meservey Tedrow method in chapter 5 and the spin Hall effect tunneling spectroscopy in chapter 6. Since the analytical solution of the hexagonal lattice is of greater importance for the rest of the thesis and gives a more detailed description of the TI physics, a detailed derivation is shown only for that lattice. The simpler solution for a tetragonal lattice, which has some relevance for the quantum transport calculations, is briefly stated at the end of this section.

The bulk physics of the model TI for sufficiently separated surfaces is well represented by the Hamiltonian in momentum space, corresponding to an infinite system. Dispersion and eigenstates of the bulk are therefore easily obtained by diagonalization of the 4×4 matrix Eq. (3.20). The size of the bulk gap can then be read from the twofold degenerate energy eigenvalues

$$\epsilon_{\pm}(\mathbf{k}) = \epsilon_0 \pm \sqrt{m_1^2 + m_2^2 + (m_3 + \mathcal{R}_2)^2 + m_4^2 + \mathcal{R}_1^2} \quad (3.21)$$

of the valence (−) and conduction bands (+). To get the exact surface states for a lattice with Z lattice sites in z -direction and periodic boundaries in the other directions, a $4Z \times 4Z$ matrix has to be solved. This can only be done numerically. An analytical approximation of the surface states can be obtained under the assumption of well separated surfaces, following Ref. [76].

For well separated surfaces, the system is considered half infinite with open boundary con-

3 Model Hamiltonian

ditions $\psi(k_x, k_y, z = 0) = 0$ and $\psi(k_x, k_y, z \rightarrow \infty) = 0$ for the surface states. Then, as a first step, k_x and k_y are set to zero, and all k_z -dependent terms are expanded up to second order in k_z . After the expansion, k_z is replaced by the momentum operator $-i\partial_z$. These steps decouple the Hamilton matrix H into two identical 2×2 sub-matrices

$$H' = \begin{pmatrix} M_0 - (C_1 + M_1) \partial_z^2 & -B_0 \partial_z \\ B_0 \partial_z & -M_0 - (C_1 - M_1) \partial_z^2 \end{pmatrix}, \quad (3.22)$$

coupling only orbital $1 \uparrow$ with $2 \uparrow$ and $1 \downarrow$ with $2 \downarrow$, respectively.

A nontrivial solution that satisfies the boundary conditions must have the form

$$\psi(z) = \begin{pmatrix} u_1 \\ u_2 \end{pmatrix} (e^{-\alpha_1 z} - e^{-\alpha_2 z}) \quad (3.23)$$

with $\alpha_1 \neq \alpha_2$ and $\text{Re}\alpha_{i=1,2} > 0$. So, with the ansatz $\psi(z) = \begin{pmatrix} u_1 \\ u_2 \end{pmatrix} e^{-\alpha z}$, the eigenvalue problem

$$\begin{pmatrix} M_0 - (C_1 + M_1) \alpha^2 & B_0 \alpha \\ -B_0 \alpha & -M_0 - (C_1 - M_1) \alpha^2 \end{pmatrix} \begin{pmatrix} u_1 \\ u_2 \end{pmatrix} e^{-\alpha z} = E \begin{pmatrix} u_1 \\ u_2 \end{pmatrix} e^{-\alpha z} \quad (3.24)$$

has to be solved. From the characteristic polynomial, the expressions

$$\alpha_{\pm}^2 = -\frac{(EC_1 + M_0 M_1 + \frac{B_0^2}{2})}{(C_1^2 - M_1^2)} \pm \sqrt{\frac{(EC_1 + M_0 M_1 + \frac{B_0^2}{2})^2}{(C_1^2 - M_1^2)^2} - \frac{E^2 - M_0^2}{(C_1^2 - M_1^2)}} \quad (3.25)$$

for the exponent α and

$$u_1 = 1, \quad u_2 = -\frac{(M_0 - (C_1 + M_1) \alpha^2 - E)}{B_0 \alpha} \quad (3.26)$$

for the vector components are obtained. To fulfill the boundary conditions, it follows from Eq. (3.23) that u_2 has to be equal for α_{\pm} , i.e. $u_2(\alpha_+) = u_2(\alpha_-)$. This relation can then be solved for the energy

$$E = -\frac{C_1 M_0}{M_1} \quad (3.27)$$

of the Dirac point. When Eq. (3.27) is inserted back into Eq. (3.25), α_{\pm}^2 simplifies to

$$\alpha_{\pm}^2 = \left(\frac{M_0}{M_1} + \frac{B_0^2}{2(M_1^2 - C_1^2)} \right) \pm \frac{1}{(M_1^2 - C_1^2)} \frac{B_0^2}{2} \sqrt{1 + \frac{M_0}{M_1} \frac{4(M_1^2 - C_1^2)}{B_0^2}} \quad (3.28)$$

$$= \frac{B_0^2}{4(M_1^2 - C_1^2)} \left[1 \pm \sqrt{1 + \frac{M_0}{M_1} \frac{4(M_1^2 - C_1^2)}{B_0^2}} \right]^2. \quad (3.29)$$

3.2 Analytical dispersion and surface states

Here, it was assumed that $M_1 > C_1$, which is the case for the investigated parameters. However, the only difference when $M_1 < C_1$ is that \pm in the right expressions has to be changed to \mp , i.e. only the declaration of the exponents is changed. For the given parameter sets, solutions with $\text{Re}\alpha > 0$ are obtained by taking the positive roots of α_{\pm}^2 . The final vector components [2]

$$u_1 = \sqrt{\frac{M_1 - C_1}{2M_1}}, \quad u_2 = \sqrt{\frac{M_1 + C_1}{2M_1}} \quad (3.30)$$

of $\psi(z)$ are then obtained by inserting Eq. (3.27)-(3.29) into Eq. (3.26) and successive normalization. So the two degenerate surface states at the Dirac point are [2]

$$\psi_1(z) = \frac{1}{N} \begin{pmatrix} u_1 \\ 0 \\ u_2 \\ 0 \end{pmatrix} (e^{-\alpha_1 z} - e^{-\alpha_2 z}), \quad \psi_2(z) = \frac{1}{N} \begin{pmatrix} 0 \\ u_1 \\ 0 \\ u_2 \end{pmatrix} (e^{-\alpha_1 z} - e^{-\alpha_2 z}), \quad (3.31)$$

where N is a normalization constant for the z -dependent part that will not be further specified.

Surface states with finite in-plane momentum can be obtained through degenerate perturbation theory. For that purpose, all neglected terms are combined into the matrix

$$H_{\mathbf{k}} = \begin{pmatrix} \epsilon'_0 + m'_4 & 0 & \mathcal{R}_1 - i\mathcal{R}_2 & m_1 - im_2 \\ 0 & \epsilon'_0 + m'_4 & m_1 + im_2 & -\mathcal{R}_1 - i\mathcal{R}_2 \\ \mathcal{R}_1 + i\mathcal{R}_2 & m_1 - im_2 & \epsilon'_0 - m'_4 & 0 \\ m_1 + im_2 & -\mathcal{R}_1 + i\mathcal{R}_2 & 0 & \epsilon'_0 - m'_4 \end{pmatrix} \quad (3.32)$$

with reduced coefficients

$$\epsilon'_0 = \frac{4}{3}C_2 \left(3 - 2 \cos \left(\frac{\sqrt{3}}{2}k_y \right) \cos \left(\frac{1}{2}k_x \right) - \cos(k_x) \right),$$

$$m'_4 = \frac{4}{3}M_2 \left(3 - 2 \cos \left(\frac{\sqrt{3}}{2}k_y \right) \cos \left(\frac{1}{2}k_x \right) - \cos(k_x) \right).$$

The eigenvalues of

$$H_s = \begin{pmatrix} \psi_1^\dagger(H_{\mathbf{k}}\psi_1) & \psi_1^\dagger(H_{\mathbf{k}}\psi_2) \\ \psi_2^\dagger(H_{\mathbf{k}}\psi_1) & \psi_2^\dagger(H_{\mathbf{k}}\psi_2) \end{pmatrix} \quad (3.33)$$

are then the energy corrections, while the eigenvectors give the correct linear combination of the unperturbed states. So, the perturbed surface states are given by [2]

$$\psi_{\pm}(k_x, k_y, z) = v_1\psi_1 + v_2\psi_2 \quad (3.34)$$

with factors [2]

3 Model Hamiltonian

$$v_1(k_x, k_y) = -\frac{(m_1 - im_2) \operatorname{sgn}\left(\mathcal{R}_1 \mp \sqrt{m_1^2 + m_2^2 + \mathcal{R}_1^2}\right)}{\sqrt{m_1^2 + m_2^2 + \left(\mathcal{R}_1 \mp \sqrt{m_1^2 + m_2^2 + \mathcal{R}_1^2}\right)^2}}, \quad (3.35)$$

$$v_2(k_x, k_y) = \frac{\sqrt{\left(\mathcal{R}_1 \mp \sqrt{m_1^2 + m_2^2 + \mathcal{R}_1^2}\right)^2}}{\sqrt{m_1^2 + m_2^2 + \left(\mathcal{R}_1 \mp \sqrt{m_1^2 + m_2^2 + \mathcal{R}_1^2}\right)^2}} \quad (3.36)$$

and corresponding eigenvalues [2]

$$E_{\pm}(k_x, k_y) = -\frac{C_1 M_0}{M_1} + \epsilon'_0 - \frac{C_1}{M_1} m'_4 \pm \sqrt{(m_1^2 + m_2^2 + \mathcal{R}_1^2) \left(1 - \frac{C_1^2}{M_1^2}\right)}. \quad (3.37)$$

Here, \pm is for the upper and lower Dirac cone, respectively.

The spin polarization $\mathbf{p} = (p_x, p_y, p_z)$ is given by the expectation value of the spin matrices

$$\Sigma_x = \mathbb{I}_{2 \times 2} \otimes \sigma_1, \quad \Sigma_y = \mathbb{I}_{2 \times 2} \otimes \sigma_2, \quad \Sigma_z = \mathbb{I}_{2 \times 2} \otimes \sigma_3. \quad (3.38)$$

For the considered z -surface, the spin lies mainly in the surface plane

$$p_x = \psi_{\pm}^{\dagger} (\Sigma_x \psi_{\pm}) = -2 \frac{m_1 \left(\mathcal{R}_1 \mp \sqrt{(m_1^2 + m_2^2 + \mathcal{R}_1^2)}\right)}{\left(m_1^2 + m_2^2\right) + \left(\mathcal{R}_1 \mp \sqrt{(m_1^2 + m_2^2 + \mathcal{R}_1^2)}\right)^2}, \quad (3.39)$$

$$p_y = \psi_{\pm}^{\dagger} (\Sigma_y \psi_{\pm}) = -2 \frac{m_2 \left(\mathcal{R}_1 \mp \sqrt{(m_1^2 + m_2^2 + \mathcal{R}_1^2)}\right)}{\left(m_1^2 + m_2^2\right) + \left(\mathcal{R}_1 \mp \sqrt{(m_1^2 + m_2^2 + \mathcal{R}_1^2)}\right)^2} \quad (3.40)$$

with a small momentum dependent out-of-plane tilt

$$p_z = \psi_{\pm}^{\dagger} (\Sigma_z \psi_{\pm}) = \frac{m_1^2 + m_2^2 - \left(\mathcal{R}_1 \mp \sqrt{(m_1^2 + m_2^2 + \mathcal{R}_1^2)}\right)^2}{m_1^2 + m_2^2 + \left(\mathcal{R}_1 \mp \sqrt{(m_1^2 + m_2^2 + \mathcal{R}_1^2)}\right)^2}. \quad (3.41)$$

Since both considered orbitals have the same spin direction, the surface states are fully polarized, i.e. $|\mathbf{p}| = \sqrt{p_x^2 + p_y^2 + p_z^2} = 1$. Dispersion and spin polarization of the lower Dirac cone are shown in the right panel of Fig. 2.2 for the parameter set Bi_2Se_3 (a). The left panel of the same figure shows the Dirac cone for parameter set Bi_2Se_3 (b) with R_1 and R_2 set to zero. The different parameter set was chosen for illustrative purposes because it produces a better pronounced Dirac cone. For parameter set Bi_2Se_3 (a), the Dirac point is very close to the bulk conduction band so that only the lower part of a Dirac cone would be clearly visible.

3.2 Analytical dispersion and surface states

Concerning the tetragonal lattice, only analytical surface states at a y -surface in the 2D limit are of interest. By an analogous calculation, one ends up with the edge state dispersion

$$E_{\pm}(k_x) = -\frac{M_0 C_2}{M_2} \pm A_0 \sin(k_x) \sqrt{\left(1 - \frac{C_2^2}{M_2^2}\right)}, \quad (3.42)$$

where the sign now corresponds to the slope of the edge state bands, not the part of the Dirac cone. So, these edge state bands cross in the Dirac point. The corresponding edge states are

$$\psi_{+(-)}(y) = \frac{1}{\sqrt{2}N} \begin{pmatrix} \sqrt{1 - \frac{C_2}{M_2}} \\ 0 \\ 0 \\ (-) i \sqrt{1 + \frac{C_2}{M_2}} \end{pmatrix} (e^{-\alpha+y} - e^{-\alpha-y}), \quad (3.43)$$

$$\psi_{-(+)}(y) = \frac{1}{\sqrt{2}N} \begin{pmatrix} 0 \\ \sqrt{1 - \frac{C_2}{M_2}} \\ (-) i \sqrt{1 + \frac{C_2}{M_2}} \\ 0 \end{pmatrix} (e^{-\alpha+y} - e^{-\alpha-y}) \quad (3.44)$$

with

$$\alpha_{\pm}^2 = \frac{A_0^2}{4(M_2^2 - C_2^2)} \left(1 \pm \sqrt{1 + \frac{M_0}{M_2} \frac{4(M_2^2 - C_2^2)}{A_0^2}}\right)^2 \quad (3.45)$$

and some normalization constant N . Depending on the sign of $M_2 - C_2$, the edge states corresponding to the dispersion Eq. (3.42) vary. Signs in brackets correspond to the case $M_2 - C_2 < 0$, i.e. for example the parameter set Bi₂Se₃ (b).

These edge states have now only a z -spin, which is reduced to

$$p_z = \psi_{\pm(\mp)}^\dagger (\Sigma_z \psi_{\pm(\mp)}) = (-) \mp \frac{C_2}{M_2} \quad (3.46)$$

due to opposite spin orientations of the two orbitals. For the given parameter sets, the exponents are given by the positive roots of Eq. (3.45). As $\sqrt{1 + \frac{M_0}{M_2} \frac{4(M_2^2 - C_2^2)}{A_0^2}}$ is imaginary, the spatial dependence of the edge states is a superposition of an exponential decay and a sine, i.e. $(e^{-\alpha+y} - e^{-\alpha-y}) \propto e^{-y \operatorname{Re} \alpha_+} \sin(y \operatorname{Im} \alpha_+)$.

4 Pure spin current devices and quantum transport calculations

The recent experimental realization of a QAH effect in thin films of ferromagnetic TIs [20, 56, 57] (see section 2.2) grants a possibility to control current and spin flow in topological edge state channels. In ferromagnetic TIs, one of the two TI edge states is removed so that polarized edge currents propagate only in one direction along the edge. Propagation direction and spin thereby depend on the magnetization direction perpendicular to the film [18–20, 56, 57]. When ferromagnetism is induced into the TI only locally, edge currents are locally separated but not completely removed. Magnetic domains can therefore be used to direct edge currents between different leads attached to the TI film. By combining multiple magnetic domains, devices that create, switch and detect pure spin currents can be devised. A theoretical investigation of how edge currents can be steered by magnetic domains and how this can be used to create pure spin current devices is subject of this chapter. The main results of this chapter have been published in Ref. [1].

In mesoscopic devices, where the system size is smaller than the phase coherence length of the material, currents flowing between different leads can be described in terms of a scattering matrix. This scattering matrix can be calculated from the underlying Hamiltonian [77]. Consider now a homogeneous mesoscopic sheet with well separated edges of a 2D TI, with helical edge states, or a QAH insulator, with spin-polarized chiral edge states. Then, if either of the two materials is connected by leads and a voltage is applied, it is relatively easy to predict the currents flowing through certain leads. In this chapter, the interest is in the scattering matrix of 2D TIs with local ferromagnetic exchange fields (FEF). To calculate the scattering matrix of these more complex systems, multiple approaches exist. A widely used approach is the non-equilibrium Green's function (NEGF) formalism [78–80]. However, this approach involves matrix inversions, which are computationally unfavorable, and the scattering matrix can be calculated only for a single energy per calculational run [8, 77]. Here, following Krückl and Richter [8, 81], the scattering matrix is calculated from the propagation of a wave packet on a lattice. As the wave packet contains a broad energy range, the energy dependence of the scattering matrix and, at the same time, the non-equilibrium local density of states can be determined in a single calculational run. Besides, the wave packet transport calculations require only matrix vector multiplications of sparse matrices instead of matrix inversions so that much larger systems can be treated. Memory requirement and computation time scale about linear with the number of lattice sites.

The quantum transport code used here was originally written in C++ and *CUDA* by Michael Joppe [82] in his master thesis for 2D TI devices. For this thesis, however, it has been significantly enhanced regarding computation time, memory usage and functionality. Due to these enhancements, it can now be applied to much larger systems, including 3D TIs, or

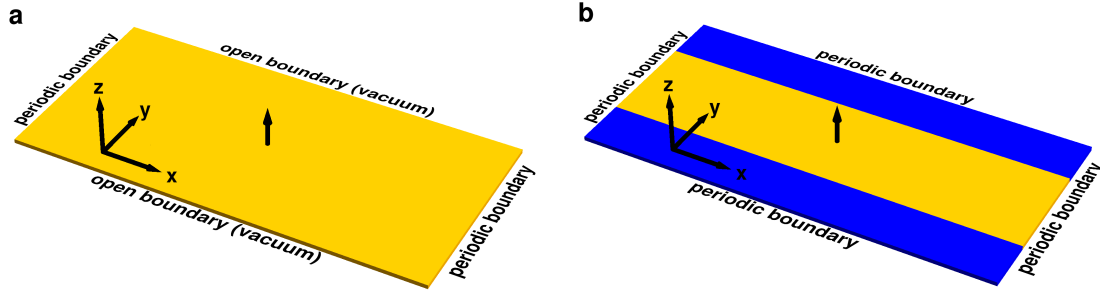


Figure 4.1: Geometry of the thin TI strips with homogeneous FEF. The FEF is only applied in the yellow regions, where the black arrow shows the direction of the field corresponding to the dispersions shown in Fig. 4.2 and 4.4.

much longer propagation times. Using an additional program, unique device structures with arbitrary geometries, local electrostatic fields and FEFs can be created by means of simple commands and then put into the quantum transport code. Even heterostructures of TIs and trivial insulators can be investigated.

This chapter is structured as follows. In section 4.1, the evolution of edge states in the presence of homogeneous FEFs is investigated to get a first estimate of the conducting channels and their gap sizes and polarizations as well as the required field strengths. The concepts of the quantum transport calculations are presented in section 4.2. These concepts are then first applied to a pure 2D system in section 4.3, and based on the obtained results, pure spin current devices are conceived in section 4.4. The robustness of these devices with respect to some effects present in real devices is checked in section 4.5.

4.1 Evolution of edge states in a ferromagnetic exchange field

This chapter is mostly about scattering at magnetic domains in a 2D TI. It is therefore reasonable to first look at the evolution of edge states in the presence of a homogeneous FEF. This gives already a good estimate of the behavior of the propagating wave packet in sufficient distance to potential scattering regions. The dispersion relation yields information on the size and position of the bulk gap as well as the presence, degeneracy and propagation of edge states. A closer look at the edge states gives additional information like the spin.

The dispersion relations shown in the following are calculated by exact numerical diagonalization of the Hamiltonian Eq. (3.11) on a lattice with open boundaries in y -direction and periodic boundary conditions in x -direction. Thus, the wavenumber k_x remains a good quantum number, and eigenvalues and eigenvectors can be calculated separately for each k_x for a 1D chain in y -direction. This is done using built-in functions of the computer algebra program *Wolfram Mathematica*. Parameters are chosen corresponding to a thin layer of Bi_2Se_3 (parameter set (b) in Tab. 3.1) with an effective $M_{2D} = 0.17\text{eV}$, corresponding to a film thickness of 15 layers. Analogous calculations for the case of a TI constricted by vacuum (Fig. 4.1a) have been done in Ref. [53, 54]. Other parameter sets are briefly discussed in section 4.3.3.

4.1 Evolution of edge states in a ferromagnetic exchange field

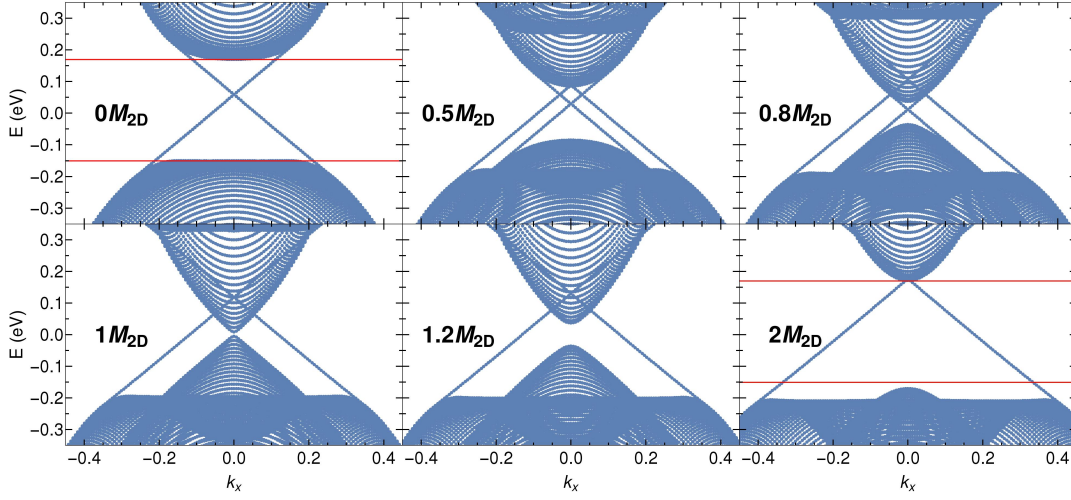


Figure 4.2: Numerical dispersion around the bulk gap of a TI with homogeneous FEF V_z of various strength (see labels). The TI is bounded by vacuum in y -direction, as depicted in Fig. 4.1a. When the FEF is increased, so far degenerate edge state bands of opposite pseudo-spin split and the bulk gap closes. At a critical field strength of $V_z = M_{2D}$, the system undergoes a quantum phase transition into a quantum anomalous Hall state with only spin-up states remaining inside the bulk gap. At $V_z = 2M_{2D}$, the original bulk gap, indicated by horizontal red lines, is restored.

For the case of a thin TI strip with homogeneous FEF of strength V_z in z -direction (perpendicular to the surface plane) in contact to vacuum as depicted in Fig. 4.1a, the dispersion is shown in Fig. 4.2. The lattice has a size of $Y = 256$ lattice sites in y -direction, and the momentum discretization $\Delta k_x = \frac{2\pi}{1024}$ corresponds to $X = 1024$ lattice sites in x -direction. Without FEF, conduction and valence band are separated by a bulk gap of about 0.3eV. Inside this bulk gap, two twofold degenerate, approximately linearly dispersing bands of edge states exist, which cross at $k_x = 0$. Depending on the group velocity $v_x = \frac{1}{\hbar} \frac{\partial E}{\partial k_x}$, electrons in these edge states propagate either in positive or negative x -direction along the edge. Considering a thin TI sheet of finite size, these edge states form two channels with opposite pseudo-spin and opposite propagation direction along the edge. Edge states contributing to one channel are orthogonal to those of the other channel. All edge states propagating clockwise, i.e. in positive x -direction at the upper edge (larger y -values) and in negative direction at the lower edge, have only contributions from orbital $1 \uparrow$ and $2 \downarrow$, where orbital $1 \uparrow$ is dominant. This leads to a net positive z -polarization. Edge states propagating in the opposite direction have only contributions from orbital $1 \downarrow$ and $2 \uparrow$ and therefore a net negative z -polarization. However, the absolute value of the spin polarization $p = |C_2/M_2| \approx 0.35$ is the same for both types of states. In the following, these pseudo-spin states will therefore be referred to as spin-up and

4 Pure spin current devices and quantum transport calculations

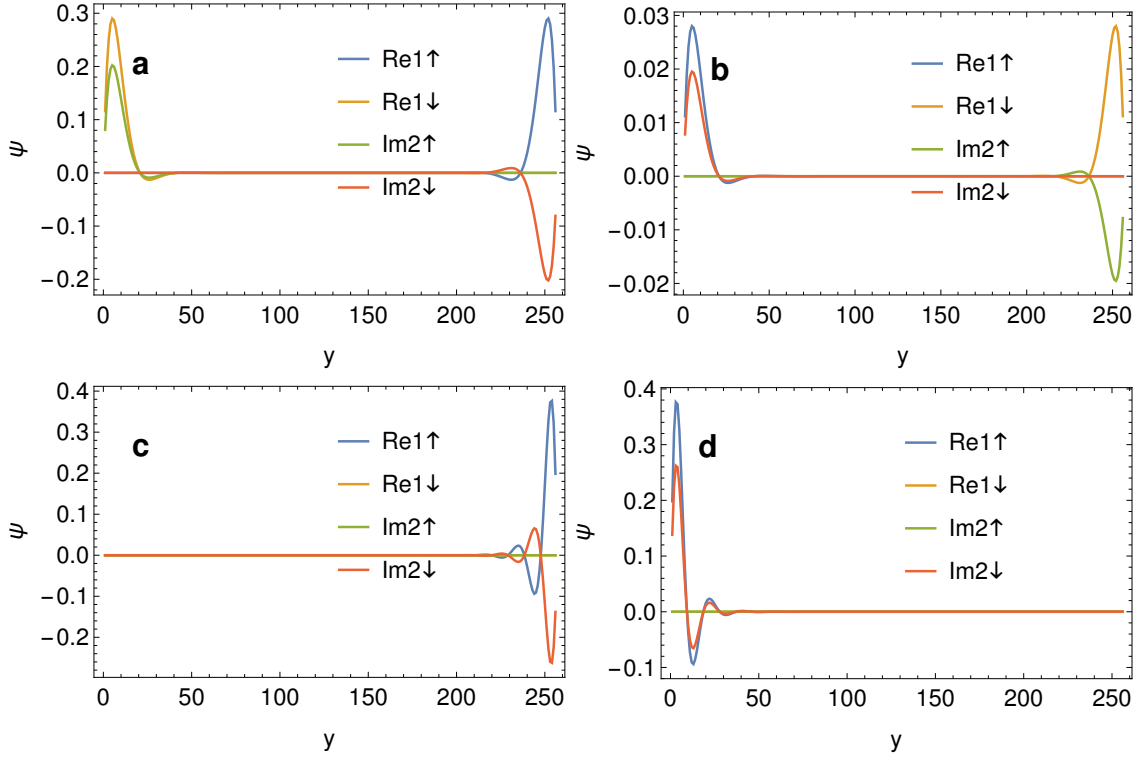


Figure 4.3: Numerical edge states of a TI bounded by vacuum. **(a)+(b)** show the case without FEF, where in **(a)** $k_x = -0.1$ and $v_x > 0$ and in **(b)** $k_x = 0.1$ and $v_x < 0$. There are two edge states each, with opposite pseudo-spin on opposite edges. Edge states have only contributions from either 1 \uparrow and 2 \downarrow or 1 \downarrow and 2 \uparrow so that the dominance of orbital 1 results in a net positive or negative z -polarization. With positive FEF $V_z = 2M_{2D}$ (**(c)+(d)**), only edge states with pseudo-spin up exist. Again, in **(c)** $k_x = -0.1$ and $v_x > 0$ and in **(d)** $k_x = 0.1$ and $v_x < 0$.

spin-down states, according to their predominant spin direction. Four edge states with a common energy are shown exemplarily in Fig. 4.3**a+b** for $|k_x| = 0.1$. The phase of the eigenstates was adjusted so that orbital 1 is real and orbital 2 imaginary, and only these components are shown.

When an FEF is applied, the edge state bands split and the bulk gap becomes smaller. Spin-up bands are shifted towards higher momenta, while spin-down bands are slightly shifted towards smaller momenta and gradually become part of the bulk bands while further increasing the field. At $V_z = M_{2D}$, valence and conduction band of the bulk states touch and the spin-down states completely disappear. For even higher field strengths, the bulk gap reopens, but the spin-down edge states remain absent. The system now features only edge states with spin-up and clockwise propagation direction (see Fig. 4.3**c+d**), i.e. it is in a quantum anomalous Hall state. To utilize the full size of the TI bulk gap in devices with local FEFs, the bulk gap of the TI with FEF has to span the full energy range of the pure TI bulk gap, which is

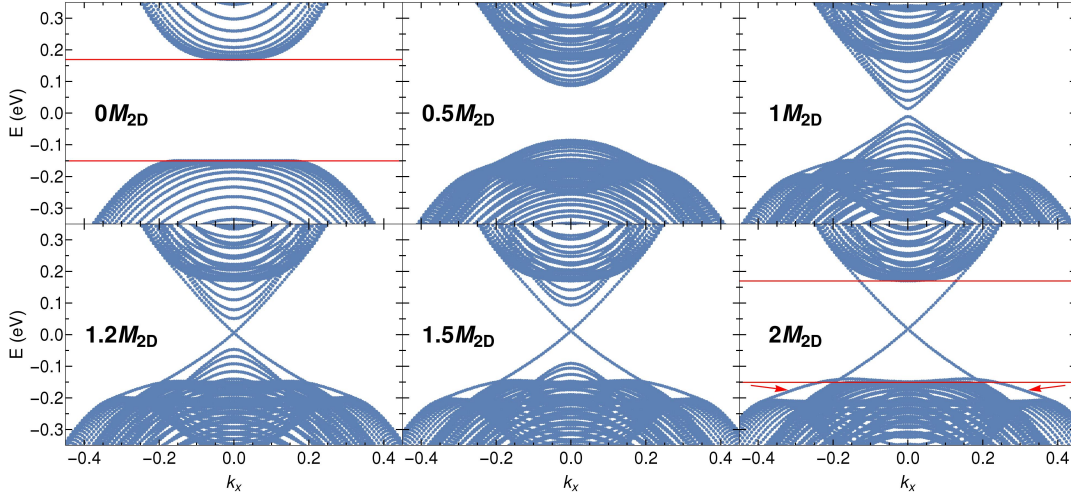


Figure 4.4: Numerical dispersion around the bulk gap of a TI with homogeneous FEF V_z of various strength (see labels) in contact with a pure TI as shown in Fig. 4.1b. Like in the vacuum restricted case, the system undergoes a quantum phase transition into a QAH state at $V_z = M_{2D}$. However, the spin of the edge states is opposite, while the propagation direction is the same. At $V_z = 2M_{2D}$, the original bulk gap, indicated by red horizontal lines, is nearly restored. Overlapping with the lower band edge and slightly reaching into the bulk gap, two more edge state bands, marked by red arrows, of opposite pseudo-spin exist.

achieved for $V_z \gtrsim 2M_{2D}$. For the used Bi_2Se_3 parameters, this corresponds to $V_z \gtrsim 0.34\text{eV}$. The two edge state bands now cross in the conduction band. They have thereby a slightly modified group velocity compared to the case without FEF. The degree of spin-polarization, however, remains the same as without FEF, as can already be seen from the analytical approximation of edge states (section 3.2). An FEF in z -direction acts like an effective parameter $M_{\text{eff}} = M_{2D} \pm V_z$ and therefore has no influence on the spin-polarization. Here, \pm belongs to matrix elements acting on the spin-up and spin-down vector components, respectively. An FEF of opposite sign yields the same dispersion relation with interchanged spin states, i.e. in the QAH state, only spin-down edge states with counterclockwise propagation direction exist. In the following, a TI with an FEF that is strong enough to drive the TI into a QAH state will be referred to as a ferromagnetic topological insulator (FTI).

In TI devices with local FEFs, there are naturally not only interfaces with vacuum but also with a pure TI. The edge states emerging at such an interface can be studied with the geometry depicted in Fig. 4.1b. Compared to Fig. 4.1a, the FEF has been restricted to $Y = 128$ lattice sites in the middle of the sheet, thereby creating two boundaries of the FTI with a pure TI. In order to remove other edge states normally emerging at the TI-vacuum interfaces, the first and last lattice site in y -direction have been linked to create periodic boundary conditions.

4 Pure spin current devices and quantum transport calculations

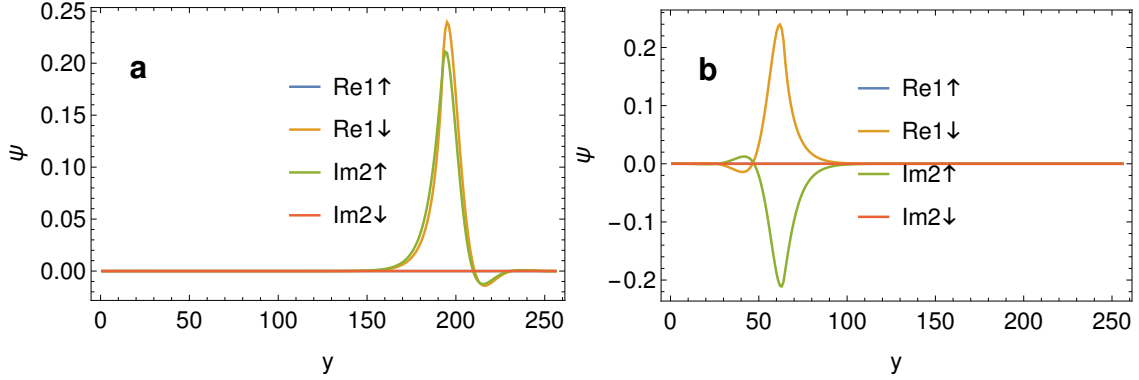


Figure 4.5: Edge states of an FTI with $V_z = 2M_{2D}$ bounded by a pure TI. **(a)** $k_x = -0.1$ and $v_x > 0$. **(b)** $k_x = 0.1$ and $v_x < 0$. The edge states are localized at the interface and have pseudo-spin down, in contrast to the vacuum interface. Compared to the vacuum bounded case, the edge states are also less localized and have a smaller spin-polarization.

Without FEF, there are logically no edge states, because there is no interface, and the size of the bulk gap is the same as for the TI bound by vacuum. With FEF, the bulk gap narrows until it closes at about $V_z = M_{2D}$ and edge state bands start to separate from the bulk bands. For higher fields, the bulk gap reopens with a pair of edge state bands with pseudo spin-down, crossing at $k_x = 0$ inside the gap. The corresponding eigenstates are localized at the interface between TI with and without FEF (see Fig. 4.5). This is in contrast to the TI-vacuum interface, where the remaining edge states for a positive FEF had pseudo spin-up. However, the propagation direction along the edge of an FTI with positive FEF surrounded by a pure TI is the same as for the one surrounded by vacuum. Though the pseudo-spin is the same as for the vacuum interface, i.e. the eigenstates have only contributions from the same two orbitals, the degree of spin polarization is smaller ($p \approx 0.16$ at the peak position). The group velocity of the edge states is slightly higher than that of edge states at a TI-vacuum interface without FEF. Additionally, while the original bulk gap was restored for $V_z = 2M_{2D}$ at the FTI-vacuum interface, it is now effectively reduced at the lower gap edge and cannot be further increased by increasing the field. Overlapping with the lower gap edge and slightly reaching into the bulk gap, two more edge state bands exist. These states have only contributions from orbital 1 \uparrow and 2 \downarrow , but the polarization is strongly spatially dependent. If the FEF is increased beyond $V_z = 2M_{2D}$, these bands are gradually pushed into the bulk gap. However, as they do not cross the bulk gap, they are not topologically protected and may therefore be removable from the bulk gap by smooth changes of the Hamiltonian.

An in-plane FEF always opens a gap in the edge state dispersion at the TI-vacuum interface, independent of its strength (Fig. 4.6a). Additionally, it enables spin-flip scattering as it couples the former decoupled pseudo-spin states. So, a combination of these two effects may also have practical use in spintronic devices for blocking certain edge state channels. Besides, any device allegedly only having FEFs perpendicular to the surface may in practice have in-

4.1 Evolution of edge states in a ferromagnetic exchange field

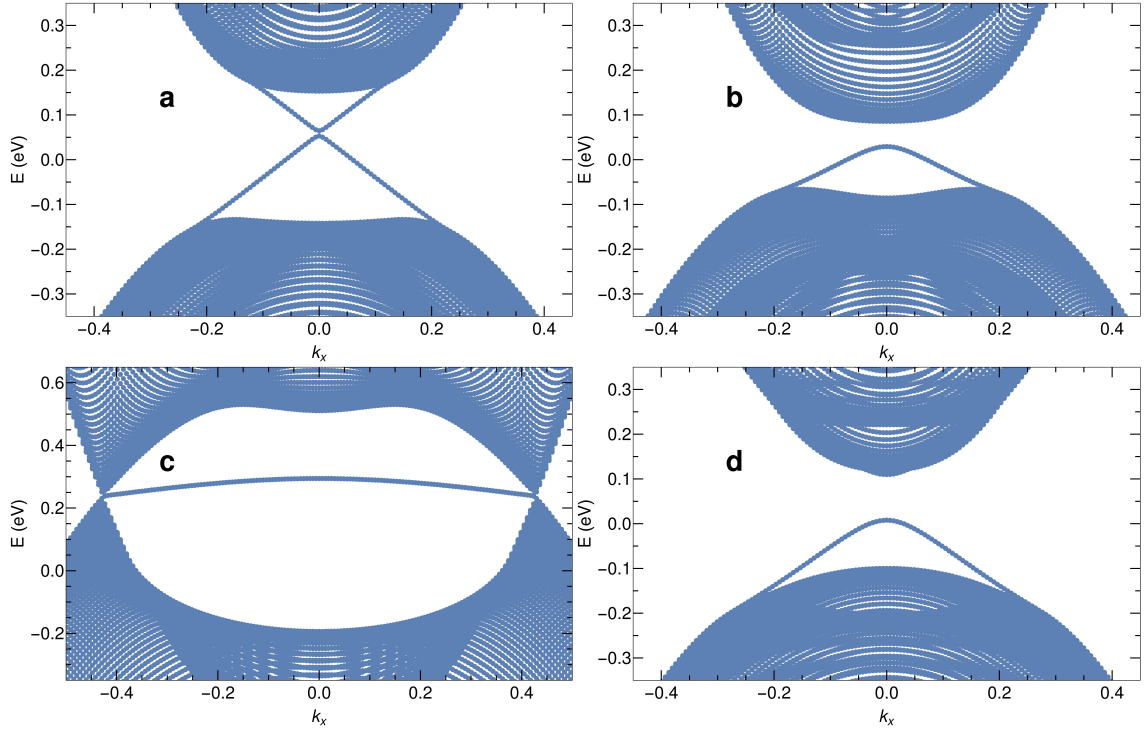


Figure 4.6: Dispersion of a TI with in-plane FEF bounded by vacuum. **(a)** Already a small field of $V_y = 0.1M_{2D} = 0.017\text{eV}$ opens a visible gap in the edge state bands. **(b)** Higher fields ($V_y = 0.5M_{2D}$) widen the gap in the edge state bands but, at the same time, shrink the bulk gap. **(c)** For very high fields ($V_y = 4M_{2D}$), a flat band emerges that spans between two Weyl nodes. The material is then called a Weyl semi metal [53, 54]. **(d)** An FEF in x -direction results in a favorable gap size already for smaller fields ($V_x = 0.3M_{2D}$).

plane components as well, e.g. at domain boundaries, where the magnetization rotates from positive to negative (see section 4.5.1).

When the in-plane field is increased, the gap in the edge state bands becomes bigger and the bulk gap becomes smaller. The best relation between the two gap sizes is realized for $V_y \approx 0.5M_{2D}$ for a y -field (Fig. 4.6**b**) and $V_x \approx 0.3M_{2D}$ for an x -field (Fig. 4.6**d**). The x -field yields the overall better result and this already at a smaller field strength. For higher fields, first the bulk gap closes at $V_{x/y} = M_{2D}$, and then, the material transforms into a Weyl semi metal if the field is orthogonal to the edge, i.e. in this case, directed into the y -direction (Fig. 4.6**c**) [53, 54]. In a Weyl semi metal, the bulk bands touch in two “Weyl nodes” and a flat band spans between these two points. Even though flat bands will sometimes emerge, Weyl semi metals will not be discussed in detail in this thesis.

Dispersions corresponding to Fig. 4.6**b+d** but at an FTI-TI interface are the same in the vicinity of the gap edges, only without any edge states inside the bulk gap.

4.2 Transport algorithm

In order to get the time-evolution of a given quantum state $\psi(\mathbf{r}, t_0)$ in a system described by the Hamiltonian $H(t)$, the time-dependent Schrödinger equation [83]

$$i\hbar \frac{\partial}{\partial t} \psi(\mathbf{r}, t) = H(t) \psi(\mathbf{r}, t) \quad (4.1)$$

has to be solved. For a general time-dependent Hamiltonian, the solution of the Schrödinger equation can be written as [83]

$$\psi(\mathbf{r}, t) = U(t, t_0) \psi(\mathbf{r}, t_0), \quad (4.2)$$

where $\psi(\mathbf{r}, t_0)$ is the solution at time t_0 and [83]

$$U(t, t_0) = T \exp \left(-\frac{i}{\hbar} \int_{t_0}^t H(t') dt' \right) \quad (4.3)$$

the time-evolution operator. The time-ordering operator T sorts all following time-dependent factors downwards from high time values on the left to low values on the right. In the case of a time-independent Hamiltonian, Eq. (4.3) reduces to [83]

$$U(t, t_0) = \exp \left(-\frac{i}{\hbar} H(t - t_0) \right). \quad (4.4)$$

Since $H(t_0 + n\Delta t)$ commutes with $H(t_0 + m\Delta t)$ for all n and m inside a time-ordered product and $\exp(AB) = \exp(A)\exp(B)$ for commuting A and B , Eq. (4.3) is equivalent to [83]

$$U(t, t_0) = \exp \left(-\frac{i}{\hbar} H(t_0 + (N-1)\Delta t) \Delta t \right) \cdot \dots \cdot \exp \left(-\frac{i}{\hbar} H(t_0) \Delta t \right). \quad (4.5)$$

Here, $\Delta t = \frac{t-t_0}{N}$ ($N \rightarrow \infty$) is the discretization of the time-interval $[t_0, t]$ into N infinitesimal subintervals. This product notation with finite N is the basic concept of the numerical time-evolution. Starting from an initial state $\psi(\mathbf{r}, t_0)$, $\psi(\mathbf{r}, t_0 + n\Delta t)$ is calculated successively via the recursion relation

$$\psi(\mathbf{r}, t_0 + n\Delta t) = \exp \left(-\frac{i}{\hbar} H(t_0 + (n-1)\Delta t) \Delta t \right) \psi(\mathbf{r}, t_0 + (n-1)\Delta t). \quad (4.6)$$

If the Hamiltonian is time-dependent, the time-steps Δt have to be small enough to assume $H(t)$ to be approximately constant during the time-step. For a time-independent Hamiltonian, the size of Δt is only a matter of convergence (see section 4.2.2).

The general setup for all transport calculations is shown in Fig. 4.7. It consists of a TI strip in real space (blue) with periodic boundaries in x -direction and open boundary conditions in y -direction. In the middle of the TI strip, a scattering region (orange) of arbitrary size exists, which may contain FEFs, electrostatic potentials, special geometries, and even other materials. A wave packet constructed from edge states (see section 4.2.1) can be placed in one of

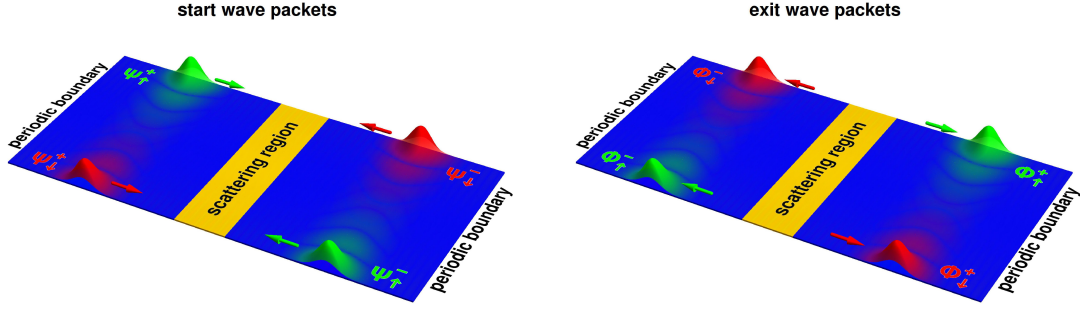


Figure 4.7: General setup for quantum transport calculations. It consists of a long TI strip in real space (blue) with open boundary condition in y -direction and a scattering region (orange) indicated in the middle of the strip. Boundaries in x -direction are usually periodically connected, with an absorbing imaginary potential at both ends. Start wave packets Ψ_α of different spin and propagation direction (see labels) can be placed at either of the four positions shown in the left figure. Additionally, spin-up wave packets are indicated by green color and spin-down wave packets by red color. Arrows show their propagation direction. Probabilities for scattering into the four edge state exit channels can be calculated through a Fourier transformation of the time-dependent overlap with exit wave packets Φ_β (see section 4.2.4). Φ_β are just spatially shifted versions of Ψ_α . Taken from Ref. [1].

the four starting positions $\Psi_{\uparrow\downarrow}^\pm$ (left figure), where the spin is also denoted by color, i.e. green for spin-up and red for spin-down. For example, Ψ_{\downarrow}^+ is a wave packet with spin-down that moves from left to right, i.e. in positive x -direction. During time-evolution, this wave packet will enter the scattering region and may thereby be scattered into one or multiple of the four exit-channels (right figure). Besides other observables (see section 4.2.4), energy dependent scattering rates into these channels can be calculated from the time-dependent overlap with shifted copies $\Phi_{\uparrow\downarrow}^\pm$ of all four starting wave packets. To avoid repeated passages of the wave packet, imaginary potentials, which absorb incoming wave packets, can be added at the ends of the strip (see section 4.2.3).

4.2.1 Wave packets

Wave packets for quantum transport calculations are constructed from eigenstates of the Hamiltonian Eq. (3.11) without FEF in contact to vacuum. The eigenstates are calculated by exact numerical diagonalization, analogous to section 4.1. Periodic boundaries are applied in x -direction and open boundaries in y -direction. So, for a given k_x , one gets a set of one-dimensional eigenstates $\psi_{k_x}^i(y)$, depending only on y . The corresponding dispersion is therefore similar to that shown in the upper left panel of Fig. 4.2. From these eigenstates, only those belonging to the edge state bands are chosen and then sorted into four groups (denoted by ν), according to the sign of their group velocity $v_x(k_x) = \frac{1}{\hbar} \frac{\partial E(k_x)}{\partial k_x}$ and their spin. ν can therefore take the values $\uparrow +$, $\downarrow +$, $\uparrow -$, and $\downarrow -$, in consistence with the previous section.

4 Pure spin current devices and quantum transport calculations

The chosen edge states are not only from inside the bulk gap but also to a certain degree from outside the bulk gap as long as the edge state bands and bulk bands are well separated. This increases the width in momentum-space and thereby results in a better localization of the wave packet in real-space and a smoother energy cut-off at the gap edges. Especially, the momentum cut-off is moved out of the bulk gap. The states $\chi_\nu(k_x, y)$ of each group are then Fourier transformed in k_x to form wave packets that are located around x_0 on the x - y -lattice in real space [1, 8]

$$\Psi_\nu(x, y) = \frac{1}{\sqrt{2\pi}} \sum_{k_x} \eta_\nu(k_x) \chi_\nu(k_x, y) e^{ik_x(x-x_0)} \Delta k_x. \quad (4.7)$$

The sum runs over all k_x contributing to $\chi_\nu(k_x, y)$, with a discretization of $\Delta k_x = \frac{2\pi}{X}$ for X lattice sites in x -direction. By weighting the states of each group ν with a Gaussian distribution

$$\eta_\nu(k_x) = \frac{1}{(2\pi d^2)^{1/4}} e^{-\frac{(k_x - k_0)^2}{4d^2}} \quad (4.8)$$

of width d , located around the mean value k_0 of the k_x , the momentum cut-off at the ends of the edge state bands is smoothed out.

Although this is the general principle of constructing the wave packets, the real process of calculating and grouping the eigenstates encounters some difficulties. As discussed before, the edge states for a given k_x are at least twofold degenerate and may therefore be superpositions of the two orthogonal spin states residing on opposite edges. At $k_x = 0$, they are even a superposition of all four edge states since the edge state bands cross at $k_x = 0$. In addition to these effects due to degeneracies, hybridization of edge states from opposite edges in a finite system opens a small gap at $k_x = 0$ and mixes the different spin states in the vicinity of $k_x = 0$ as well. In order to separate the different spin states, the numerical eigenstates have to be linearly combined. This is done in a *Mathematica* program by applying the following scheme.

First, an energy range around the bulk gap is defined that determines the ends of the edge state bands. Then, for a given k_x , the edge states are picked from all eigenstates within this energy range. When the Hamiltonian is shifted in energy so that the crossing of the edge state bands happens at zero energy, the requested edge states are simply the states with the smallest positive and negative absolute energy values, respectively. For $k_x < 0$, edge states with positive energy have negative group velocity and vice versa. Now, linear combinations of these edge states are created to get edge states that are localized only at one edge and have the correct group velocity.

As a start, a $k_{x0} < 0$ is chosen that is somewhat in the middle between Dirac point and the ends of the edge state bands. By this, the corresponding edge states are well localized at the edges and the eigenstates are only linear combinations of the two edge states with the same group velocity, residing at different edges. Close to the point where the edge state bands touch the bulk bands, the localization of the edge states gets worse so that it is no longer a valid assumption that an edge state is effectively zero at the opposite edge. However, these ‘‘edge’’ states have to be included into the wave packet to achieve a sufficient momentum width and

an energy overlap beyond the bulk gap. Why this overlap is needed can be seen in section 4.3. At k_{x0} , the two eigenstates of each band are now linearly combined and sorted by the following mechanism.

As group velocity and spin are unambiguously linked to the edge at which an edge state resides, the edge can be used in place of the spin to sort edge states. The edge state with a higher weight in the left half ($1 \leq y \leq \frac{Y}{2}$) is therefore associated with this edge and the other state with the opposite edge. At k_{x0} , it is reasonable to assume that an edge state has to be effectively zero at the other edge. Hence, to remove contributions of the right state from the left state, the right state is multiplied with the relative weight in one of the four orbitals of the two edge states at the rightmost lattice site and then subtracted from the left state. To get the best result, the orbital with the highest absolute value on the right side of the left state is chosen. After normalizing the new state, this is done in reverse order, removing unwanted contributions from the left side of the right edge state.

From there on, as there is always a set of already prepared edge states for the previous k_x , linear combinations are created based on the overlap with these states. Starting from k_{x0} , k_x runs in small steps first in positive and then in negative direction to a maximal and minimal value, determined by the defined energy range and the dispersion. The new edge states ψ_i , picked from all eigenstates of the Hamiltonian, and the desired states ϕ_j can then be combined in a system of linear equations $\psi = \mathbf{C}\phi$ with $C_{ji} = \langle \phi_j | \psi_i \rangle$. Under the assumption that the edge states vary slowly as a function of k_x , C_{ji} is replaced with $C_{ji} = \langle \phi'_j | \psi_i \rangle$, where the ϕ'_j are the members of the four groups of sorted edge states with momentum closest to the one currently investigated. ϕ can then be obtained by multiplication with the inverse of \mathbf{C} , i.e. $\phi = \mathbf{C}^{-1}\psi$.

This scheme can be applied for all remaining values of k_x , even if the eigenstates are fourfold degenerate (Dirac point) and have contributions from different spin states at the same edge. When there are only two edge states within the defined energy range around the bulk gap, only ϕ'_j from the same edge state bands are invoked. Due to the particle hole asymmetry, this is usually the case at one end of each band.

The algorithm depicted in this section works for all parameter sets, even in the case of multiple layers in z -direction. Concrete values for lattice dimensions and the width d of the Gaussian distribution will therefore be given in the corresponding sections. In the case of multiple layers in z -direction, all eigenstates and wave packets get an additional z -dependence, which however, changes nothing in the presented algorithm. The weighting factors for the first part are simply just extracted from a single layer.

By invoking symmetries of the Hamiltonian, the computation time and memory requirement can be significantly reduced. For a TI with boundaries in y - (and z -) direction, the Hamiltonian $H(k_x)$ for a given k_x still commutes with the twofold rotation operator around the x -axis, while other symmetries are broken. So, there exists a set of common eigenvectors. In momentum space, this operator is given by $i\tau_3 \otimes \sigma_1$ [44]. As its operation in real space is $x \rightarrow x$, $y \rightarrow -y$, $z \rightarrow -z$, its mixed representation is given by $J_{Y \cdot Z} \otimes (i\tau_3 \otimes \sigma_1)$, where $J_{Y \cdot Z}$ is the $(Y \cdot Z) \times (Y \cdot Z)$ exchange matrix. This matrix has two $2Y \cdot Z$ -times degenerate eigenvalues, corresponding to eigenstates that are either symmetric or anti-symmetric under rotation. These eigenstates are combined into a transformation matrix T , where the first $2Y \cdot Z$ rows

belong to the first eigenvalue and rest to the second. When this transformation matrix is applied to the Hamiltonian, the transformed Hamiltonian $H'(k_x) = THT^\dagger$ separates into two independent sub blocks $H_1(k_x)$ and $H_2(k_x)$ with half the dimension of $H(k_x)$. Eigenstates and eigenvalues of these matrices are then calculated by exact numerical diagonalization. When the Hamiltonian is shifted in energy so that the crossing of the edge state bands happens at zero energy, the requested edge states are simply the states with the smallest positive and negative absolute energy value of each sub block. After resizing these eigenstates to the dimension of $H(k_x)$ by adding zeros, they are transformed back into eigenstates of $H(k_x)$ by applying T^\dagger . These eigenstates are then treated just like before.

Because $H(k_x)$ in the mixed representation transforms as $H(-k_x) = PH(k_x)P^\dagger$ under inversion $P = J_{Y,Z} \otimes (\tau_3 \otimes \mathbb{I}_{2 \times 2})$ [44], it is sufficient to calculate the edge states for $k_x \leq 0$. Edge states with $k_x > 0$ can then be obtained by applying the inversion operator P to these states.

The construction of wave packets from these edge states is performed directly on the GPU device, previous to each time-evolution run. This is much faster than reading the wave packets from a file and allows adjustments of the width d of the Gaussian distribution.

4.2.2 Numerical time-evolution

The numerical time-evolution implemented by Michael Joppe [82] is based on a Taylor expansion of the time-evolution operator. For small time-steps, for which the Hamiltonian is assumed to be constant, the time-evolution operator can be approximated as

$$U(t, t_0) = e^{-\frac{i}{\hbar}H(t_0)(t-t_0)} \approx \sum_{n=0}^{n_{\max}} \frac{\left(-\frac{i}{\hbar}H(t_0)(t-t_0)\right)^n}{n!}, \quad (4.9)$$

where n_{\max} is the expansion order. When applied to an initial state $\psi(t_0)$, the new state $\psi(t)$ can be calculated through the sum

$$\psi(t) = \sum_{n=0}^{n_{\max}} \psi_n, \quad (4.10)$$

where the summands are calculated via a short recursion relation

$$\psi_0 = \psi(t_0), \quad \psi_n = -\frac{i\Delta\tau}{\hbar}H(t_0)\psi_{n-1}. \quad (4.11)$$

In order to achieve convergence, the effective time-step $\Delta\tau = \frac{t-t_0}{\hbar}$ is chosen as $0.5 \frac{1}{\text{eV}}$ or smaller. This corresponds to real time steps of $\Delta t = t - t_0 \lesssim 3.3 \cdot 10^{-16} \text{s}$. The sum is terminated when the norm of the highest order term drops below machine precision, i.e. $\|\psi_{n_{\max}}\| < 10^{-16}$ for double precision.

So, time-evolution of a wave packet is mainly about multiplication of high dimensional matrices and vectors. Due to the tight-binding character of the Hamiltonian, which only involves nearest neighbor hopping, the matrix contains mainly zeros. It is therefore unfavorable and,

because of the size of the Hamilton matrix, even impossible to perform the multiplication in the natural way. The convenient way in such a case would be to save only nonzero matrix elements along with their coordinates. This leads already to a significantly reduced amount of data, but the calculation of the matrix vector product is not easily parallelizable due to possible write conflicts. Write conflicts occur when elements contributing to the same element of the new vector are processed on different threads at the same time.

Here, the fact is used that the action of the Hamilton matrix on a wave packet vector is the same for each lattice site, aside from varying parameters and boundary conditions. This allows to implement the action of the Hamiltonian into the code in a way that each component of the new vector is calculated as a predefined sum over components of the old vector. Instead of saving the Hamilton matrix, varying model parameters and boundary conditions can easily be passed in terms of functions or lists of values with only the dimension of the lattice. As the calculation of each vector component can now easily be assigned to a single thread, no write conflicts can occur and the whole process can be parallelized. Specifically, due to the large size of the lattice and equal arithmetic operations for each lattice site, the calculation can benefit from massive parallelization on a GPU.

Compared to a CPU, which has only few but fast cores, a GPU has a lot more but slower cores (e.g. 512 cores for the *NVIDIA GTX 580* used here). Unlike CPU cores, GPU cores are not independent but grouped into multiple so called streaming multiprocessors, which are restricted to one common operation at a time. Computation on a GPU is therefore only effective if the same arithmetic operations are applied to a large amount of connected data, which is the case here. However, computation on a GPU has some downsides as well. First, all data that is to be saved or processed further on the CPU has to be copied from the GPU device memory to the standard host memory through a rather slow connection. If a lot of these processes are needed, this can significantly reduce the profit gained by the GPU computation. Second, when it comes to calculations of observables, usually sums over vector elements are needed. When the vector is gradually reduced by calculating partial sums, it comes to a point where the GPU is no longer operated at full capacity and thereby loses its advantage. In that case, it is often faster to copy data to the host memory for further processing on the CPU. So, a fast code has to be parallelized both on GPU and CPU, in which one has to trade computation times against copy times. Computations on the CPU are parallelized with *OpenMP*. Third, even though GPUs are great for processing huge amounts of data, the actual system sizes that can be effectively processed on a single GPU are rather limited due to comparatively small device memory. This can partly be overcome by distributing calculations over multiple GPUs. Since the tight-binding model involves only nearest neighbors, the amount of data which has to be exchanged between different GPUs between each expansion step is small. Memory usage as well as GPU computation time therefore scale close to linear with the number of GPUs. Aside from this, computation on GPUs is a rather new field and is still under development. The first official support for scientific computation on GPUs through *NVIDIA* was only released in 2006 [84] and has made enormous progress since then.

Typical computation times for 2D simulations on a single GPU (*NVIDIA GTX 580*) range from less than one minute to a few minutes, depending on the simulation time. 3D calculations need between about 40 minutes for smaller systems and up to about three hours for larger

4 Pure spin current devices and quantum transport calculations

systems and longer simulation times. The largest systems treated in this thesis have a total of 7,372,800 lattice sites, where the two orbital and spin degrees of freedom at each lattice site are represented by 4 complex numbers in double precision.

A quick test with a modified program version solely running on the CPU revealed an about 43 times faster computation for the GPU code (single GPU) compared to a computation on a single CPU core (*Intel Xeon E5620* with 2.4GHz), already for a 2D lattice. For larger (3D) lattices, the advantage may be even larger because the GPU is better utilized and the impact of computations and instructions on the CPU side, which are largely independent of the lattice size, is reduced. On a single computer with eight CPU threads, computation times for the pure CPU code scaled about linear with the number of CPU threads up to four threads.

4.2.3 Boundary conditions

Devices studied by quantum transport calculations in this thesis inhabit two kinds of boundary conditions. First, there are surfaces or edges of the device material where it is in contact with vacuum. These boundaries are handled with open boundary conditions. Numerically, this is realized by evaluating only lattice indices contributing to the device and initializing the vector components of all other lattice sites with zeros so that they do not contribute to the predefined sums. The vector representing the scattering area always covers a complete rectangular cuboid in which the device structure is embedded. Out of bound indices are handled by referring to additional vector elements containing zeros. By this, the arithmetic operations are the same for each GPU thread.

A second kind of boundary condition is needed at the ends of the device with periodic boundaries. During time-evolution, a wave packet may dissolve or split into multiple parts due to scattering. Thus, in order to detect all parts of the wave packet leaving the device through edge state channels, long propagation times may be needed. As already detected parts of the wave packet must not reenter the device, either the size of the device has to be increased along with the propagation time or the wave packet must somehow be absorbed at the device ends. The first method would result in a memory requirement linear in propagation time and a computation time quadratic in propagation time, which is impracticable. As already mentioned above, the solution is to add a small negative imaginary potential [85]

$$V_{\text{abs}}(x) = -iV_i(x) \mathbb{I}_{4 \times 4} \quad (4.12)$$

to the Hamiltonian at both device ends, which is capable of absorbing incoming wave packets. The potential strength $V_i(x)$ has to be designed in a way that combines good absorption with small reflection probability. If the potential is too small, the wave packet is not completely absorbed, but if it is too steep, part of the wave packet will be reflected. To make things worse, the lattice structure of a tight-binding model breaks every potential down into a series of potential steps. Following Refs. [82, 85], the potential is chosen to increase linearly on an interval

$[x_0, x_0 + \Delta x]$ towards the ends of the TI stripe

$$V_i(x) = \begin{cases} V_{\max} \frac{\Delta x (\frac{1}{2} \pm \frac{1}{2}) \pm (x_0 - x)}{\Delta x}, & \text{if } x_0 \leq x \leq x_0 + \Delta x \\ 0, & \text{else,} \end{cases} \quad (4.13)$$

where the \pm sign belongs to the left/right edge, and V_{\max} determines the maximal value of the potential.

Absorption parameters, V_{\max} and Δx , for efficient absorption can in principle be estimated from the dispersion of the surface states [82, 85]. However, to get an optimal absorption behavior, further parameter tuning is required. For the 2D transport calculations, the absorption parameters $V_{\max} = 1.2\text{eV}$ and $\Delta x = 20$ are taken from Ref. [82]. These parameters are relatively robust since backscattering due to the imaginary potential is still forbidden. When the z -direction is included into the transport calculations, the imaginary potential can cause backscattering, so the potential slope has to be shallower. In that case, the dispersion estimation was of no big help. Sufficient absorption results are obtained with $V_{\max} = 0.15\text{eV}$ and $\Delta x = 30$ for Sb_2Te_3 and $V_{\max} = 0.20\text{eV}$ and $\Delta x = 40$ for Sb_2Te_3 on an insulating substrate and for Bi_2Se_3 .

4.2.4 Observables

During time-evolution, a wide variety of observables can be calculated from propagating wave packets after each time-step. Besides the norm of the wave packet, which is used to measure the stability of the time-evolution, the most important observables are the energy dependent scattering matrix and the non-equilibrium local density of states (LDOS). Together they provide the necessary information for constructing spintronic devices. While the square of the absolute value of the scattering matrix provides detailed information on the probabilities for an incoming electron of certain spin, movement direction and energy to be scattered into defined exit channels, the LDOS shows the path it takes.

Given the time-dependent overlap [1, 8]

$$C_{\beta,\alpha}(t) = \langle \Phi_{\beta}(x, y) | U(x, y, t) | \Psi_{\alpha}(x, y) \rangle \quad (4.14)$$

of a propagating wave packet Ψ_{α} with exit wave packets Φ_{β} , calculated for discrete time-steps during time-evolution, the energy dependent scattering matrix $S_{\beta,\alpha}(E)$ is calculated through a discrete Fourier transformation in time. The corresponding scattering probabilities of a wave packet Ψ_{α} into exit channels Φ_{β} are then given by the square of the absolute value of the scattering matrix [1, 8]

$$|S_{\beta,\alpha}|^2(E) = \frac{v^2(E)}{(2\pi)^4 \eta^4(E)} \left| \sum_t C_{\beta,\alpha}(t) e^{iEt/\hbar} \Delta t \right|^2. \quad (4.15)$$

Here, a prefactor removes the afore introduced weighting factor $\eta(E)$ and dependencies on the density of states, through the absolute value $v(E)$ of the group velocity. $\eta(E)$ is obtained

4 Pure spin current devices and quantum transport calculations

from Eq. (4.8) by substituting

$$k_x(E_{\pm}) = \mp \arcsin\left(\frac{E_{\pm} - a}{b}\right), \quad (4.16)$$

which is the inverse of the edge state dispersion

$$E_{\pm}(k_x) = a \pm b \sin k_x \quad (4.17)$$

for an arbitrary parameter set. The sign hereby equals the propagation direction, in consistency with the wave packet index ν , and a is the position of the Dirac point. In general, a and b have to be obtained by fitting the numerical dispersion of edge states, but in the case of the 2D model, $a = -\frac{M_0 C_2}{M_2}$ and $b = A_0 \sqrt{1 - \frac{C_2^2}{M_2^2}}$ can be read from Eq. (3.42). Because $k_x(E_{\pm})$ and k_0 have always the same relative sign for a given index ν and the absolute values are independent of ν ,

$$\eta(E) = \frac{1}{(2\pi d^2)^{1/4}} e^{-\frac{(\arcsin(\frac{E-a}{b}) - k_0)^2}{4d^2}} \quad (4.18)$$

is independent of ν . For the chosen sign convention, k_0 has to be calculated for a wave packet with positive group velocity. As a function of energy, the absolute value of the group velocity evaluates to

$$\begin{aligned} v(E) &= \left| \frac{1}{\hbar} \frac{\partial E(k_x)}{\partial k_x} \right| = \left| \pm \frac{b}{\hbar} \cos k_x \right| \\ &= \frac{b}{\hbar} \sqrt{1 - \left(\frac{E-a}{b}\right)^2}, \end{aligned} \quad (4.19)$$

where k_x has again been substituted by Eq. (4.16) after replacing $\cos k_x$ with $\sqrt{1 - \sin^2(k_x)}$. As long as energy is conserved during time evolution, i.e. for time-independent Hamiltonians, the sum over all exit channels β for a given start wave packet α must satisfy

$$\sum_{\beta} |S_{\beta,\alpha}|^2(E) \leq 1 \quad \forall E. \quad (4.20)$$

This condition can be used as an initial quality check of the time-evolution. Because the scattering matrix is only sensitive to edge states, the sum can always be smaller than one if scattering into bulk states happens.

LDOS at the Fermi energy E_F for electrons entering through channel α are proportional to the time-integral over the propagating wave packet [8]. The LDOS

$$|\psi_{E_F}|^2(x, y) = \left| \frac{1}{\eta(E_F)T} \int_0^T U(x, y, t) \Psi_{\alpha}(x, y) e^{iE_F t/\hbar} dt \right|^2 \quad (4.21)$$

gives the probability to find an electron with energy E_F that enters through channel α at a certain position. Without absorbing boundaries, the probability to find the electron anywhere in the device is one. Via the factor $e^{iE_F t/\hbar}$, the Fermi energy can be chosen within the energy range of the wave packet. This can be shown by expressing the wave packet $\Psi_\alpha = \sum_j c_j \psi_j$ in terms of eigenvectors ψ_j of H :

$$\begin{aligned}
 & \lim_{T \rightarrow \infty} \frac{1}{T} \int_0^T U(x, y, t) \Psi_\alpha(x, y) e^{iE_F t/\hbar} dt \\
 &= \lim_{T \rightarrow \infty} \frac{1}{T} \int_0^T e^{-iHt/\hbar} \sum_j c_j \psi_j e^{iE_F t/\hbar} dt \\
 &= \lim_{T \rightarrow \infty} \sum_j \frac{1}{T} \int_0^T e^{-iE_j t/\hbar} c_j \psi_j e^{iE_F t/\hbar} dt \\
 &= \lim_{T \rightarrow \infty} \sum_j c_j \psi_j \frac{1}{T} \int_0^T e^{i(E_F - E_j)t/\hbar} dt \\
 &= \sum_j c_j \psi_j \delta_{E_F, E_j}.
 \end{aligned}$$

The integrand is one only if $E_j = E_F$ and oscillates in the complex plane in all other cases so that the integral approaches a Kronecker delta for long times. In the case of discrete times, Eq. (4.21) reads

$$|\psi_{E_F}|^2(x, y) = \left| \frac{1}{\eta(E_F) T} \sum_t U(x, y, t) \Psi_\alpha(x, y) e^{iE_F t/\hbar} \Delta t \right|^2. \quad (4.22)$$

Multiple calculations for different E_F can be performed during one time-evolution run.

4.3 2D transport calculations

From the dispersion relations shown in section 4.1, possible edge state channels can already be identified. Local and time-dependent effects, however, e.g. at interfaces of sections with different dispersion, cannot be extracted. In order to get information about the path an electron with certain spin, energy and propagation direction takes through a given device structure, numerical quantum transport calculations are performed according to the scheme presented in the previous sections. Simulations shown in this section are based on the tetragonal Hamiltonian Eq. (3.11) in the 2D approximation, and resulting scattering probabilities have in parts already been shown by Michael Joppe in his master thesis [82]. Results of this section which are relevant for the pure spin current devices in section 4.4 have been published in Ref. [1].

The overall lattice size is 1024×128 lattice sites with a scattering region of size 128×128 in the middle. Taking the in-plane lattice constant $a = 4.14 \text{ \AA}$ of Bi_2Se_3 , this corresponds to real sizes of $424 \text{ nm} \times 53 \text{ nm}$ and $53 \text{ nm} \times 53 \text{ nm}$, respectively. Wave packets are constructed

4 Pure spin current devices and quantum transport calculations

$\frac{1024}{5}$ lattice sites away from the lattice ends with a Gaussian distribution function (Eq. (4.8)) of width $d = \frac{k_{\max} - k_{\min}}{8\sqrt{2}}$, where $k_{\max} - k_{\min} \approx 0.156$ is the momentum range of the involved edge states. Time-steps are $\Delta\tau = 0.25 \frac{1}{eV}$.

In a device without any modifications in the scattering region, i.e. no FEF etc., a wave packet will only propagate along the edge it started on, and the probability to detect it in the corresponding exit channel should therefore be one. Even though no new physically relevant information will result from such a simulation, it can be used to determine the feasible energy range of the scattering matrix. Results for a simulation of the start wave packet Ψ_{\downarrow}^+ are shown in Fig. 4.8. The shown energy range is the full energy spectrum of the wave packets. Inside the bulk gap, which is indicated by vertical black lines, the wave packet is perfectly transmitted along the lower edge of the device, i.e. $|S_{\downarrow+, \downarrow+}|^2 = 1$. Outside the bulk gap, however, $|S_{\downarrow+, \downarrow+}|^2$ shows some oscillations and even exceeds unity before it drops at the outer edges. This effect is known as Gibbs phenomenon. It emerges due to a Fourier transformation at a jump discontinuity and is therefore an effect of the finite energy range of the wave packet or steep changes in the scattering probability. By increasing the energy range beyond the bulk gap, it is possible to push oscillations originating from the finite energy range out of the bulk gap, but it is not possible to completely remove them. As a result, no quantitative assumptions can be made based on scattering probabilities outside the bulk gap. Outside the bulk gap, the scattering probability may also be reduced due to scattering into the coexisting bulk states. However, as the overlap of edge and bulk states is small, scattering is marginal in the absence of any perturbations.

4.3.1 Out-of-plane field

As discussed in section 2.2, FEFs can be induced into the TI either through the proximity effect, by capping with a ferromagnetic insulator, or via doping with transition metal atoms. This can lead to different spatial inhomogeneities. For the beginning, however, the FEFs are considered homogeneous within magnetic domains. Spatial inhomogeneities of a proximity field will be studied in section 4.5.5.

In section 4.1, it has been shown that an FEF of sufficient strength perpendicular to the surface (in z -direction) of a 2D TI in contact with vacuum removes only edge states with one spin direction, leaving the other edge states basically untouched. At an interface with a TI, either without FEF or with FEF of opposite polarization, additional edge states emerge. The pseudo-spin of the edge states thereby depends on the interface type. Considering for example an FEF in positive z -direction, edge states with spin-up exist at the interface with vacuum or a trivial insulator and edge states with spin-down at the interface with a TI. If the FEF is now restricted to a small area of the TI device where it is in contact with the device boundary (vacuum) on one side and with a pure TI on all other sides, it is expected that a spin-down wave packet moves around this area, while a spin-up wave packet should pass straight through. Quantum transport calculations largely confirm these assumptions. According to section 4.1, an FEF of $|V_z| = 0.34\text{eV}$ is needed to achieve these effects for the whole bulk gap and is therefore chosen for the following simulations. By looking at LDOS, it can be clearly seen that a spin-down wave packet (Ψ_{\downarrow}^+) encountering such a positive FTI leaves the edge

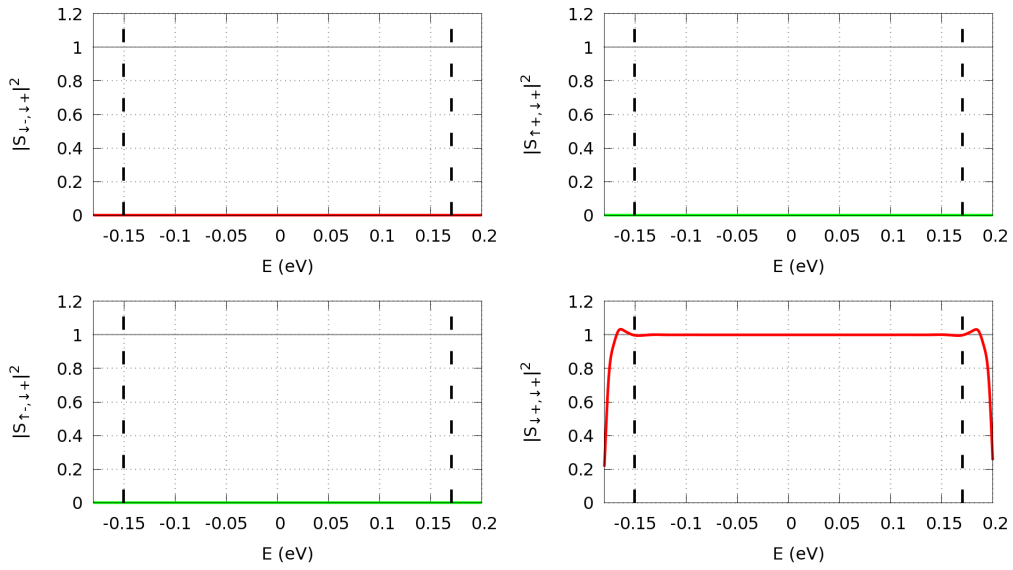


Figure 4.8: Scattering probabilities of the wave packet Ψ_{\downarrow}^+ in a TI strip without scattering region after an evolution time of $\tau = 1000 \frac{1}{eV}$. The shown energy range is that covered by the edge states contributing to the wave packets. The range of the bulk gap is indicated by vertical black lines. Even though there are no perturbations present, $|S_{\downarrow, \downarrow+}|^2$ deviates from unity at the edges of the energy range and has even values bigger than one. This effect, called Gibbs phenomenon, arises due to the Fourier transformation at the energy cut-off of the wave packet and can therefore not be completely removed.

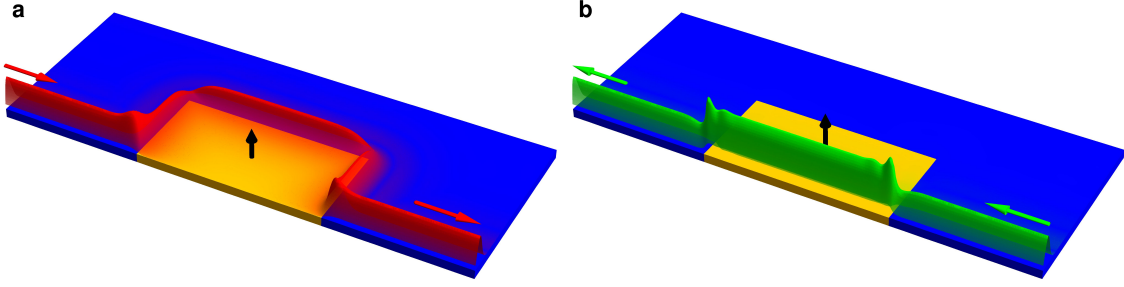


Figure 4.9: LDOS at a local FEF (orange) of strength $V_z = 0.34\text{eV}$ in positive z -direction (indicated by black arrows) located at the lower edge of a TI stripe (blue). **(a)** A spin-down wave packet (Ψ_{\downarrow}^+) takes a detour around the FTI as no spin-down channel exists at the FTI-vacuum interface. **(b)** A spin-up wave packet (Ψ_{\downarrow}^-) coming from the opposite direction at the same edge moves straight through the FTI. Arrows in the color of the wave packet show the propagation direction. The Fermi energy is chosen as $E_F = 0\text{eV}$, about in the middle of the bulk gap. Figures taken from Ref. [1].

and moves around the FTI (Fig. 4.9a). On the other hand, a spin-down wave packet (Ψ_{\uparrow}^-) coming from the opposite direction moves straight through the same FTI (Fig. 4.9b), just as expected. However, LDOS show only the path for one specified energy, which is chosen as $E_F = 0$, approximately in the middle of the bulk gap. To get a quantitative, energy dependent measure of the device efficiency, one has to look at the scattering probabilities. Inside the bulk gap, the spin-down wave packet is perfectly transported from left to right (see Fig. 4.10). Outside the bulk gap, the transmission probability $|S_{\downarrow+, \downarrow+}|^2$ now drops instantly to very low values, meaning that scattering into bulk states is strongly enhanced compared to Fig. 4.8. The reason for this is that the momentum of the wave packet is changed at every corner of the FTI, making scattering into the much more numerous bulk states more likely. As the density of states is higher below the bulk gap, the effect is more prominent. Any part of the wave packet that is scattered into bulk states remains basically undetected as the scattering matrix is insensitive to bulk states. As a consequence, no notable scattering probability is measured for the other exit channels. Scattering into spin-up channels is even completely forbidden because spin-up and spin-down states are completely decoupled in the 2D Hamiltonian as long as there is no in-plane FEF. In the following, therefore, only spin-up or spin-down channels will be shown as long as the Hamiltonian forbids spin-flip scattering.

The transition probability of the spin-up wave packet Ψ_{\uparrow}^- through the FTI is one for the biggest part of the bulk gap as well (see Fig. 4.11). Only at the lower edge of the bulk gap, it drops rapidly. As has been seen in Fig. 4.4, a positive FEF gives rise to additional edge states with pseudo-spin up at the FTI-TI interface. So, at the two points where the wave packet enters and leaves the FTI, it is scattered into this additional channel going around the FTI. A very low group velocity with momentum dependent sign results in long dwell times in this channel. Only for very long evolution times (at least ten times longer than shown), the

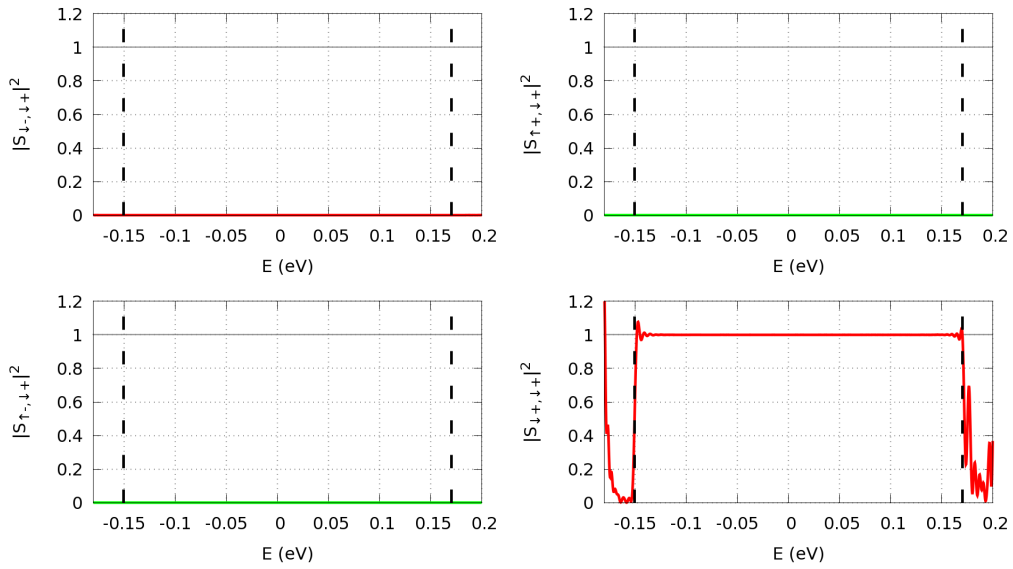


Figure 4.10: Scattering probabilities corresponding to the setup shown in Fig. 4.9a after an evolution time of $\tau = 2000 \frac{1}{\text{eV}}$. Inside the bulk gap, the wave packet is perfectly transferred around the FTI into the Φ_{\downarrow}^{+} exit channel. Outside of the gap, the probability drops instantly to nearly zero due to increased scattering into bulk states at all corners of the FTI. These parts remain basically undetected since the scattering matrix is insensitive to bulk states. The steep drop in the scattering probability causes Gibbs oscillations inside the bulk gap. No notable scattering into other exit channels is measured.

4 Pure spin current devices and quantum transport calculations

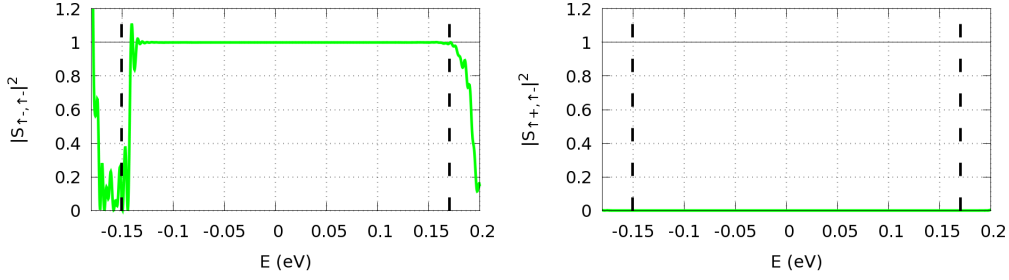


Figure 4.11: Scattering probabilities corresponding to the setup shown in Fig. 4.9b after an evolution time of $\tau = 2000 \frac{1}{\text{eV}}$. As spin-flip scattering is forbidden by the Hamiltonian, only spin-up channels are shown. Over the vast majority of the bulk gap, the wave packet is perfectly transferred through the FTI into the Φ_{\uparrow}^- exit channel. Only at the lower end of the bulk gap, the transmission probability drops rapidly due to scattering into the additional edge states at the FTI-TI interface (see Fig. 4.4).

transmission probability approaches one for the whole bulk gap. Scattering into bulk states for energies above the bulk gap is less prominent compared to Fig. 4.10 because the propagation direction of the wave packet is conserved at the FTI area.

When the FTI is extended towards the opposite edge of the TI strip, the incoming spin-down wave packet Ψ_{\downarrow}^+ is no longer transferred into the Φ_{\downarrow}^+ exit channel because the spin-down path is now removed from the other edge of the FTI as well. Instead, it moves along the edge of the FTI towards the opposite edge and then in negative x -direction, leaving the device through the Φ_{\downarrow}^- exit channel (Fig. 4.12a). Reflection into the counter propagating channel is now logically perfect inside the bulk gap as there is no spin-down channel inside the FTI. Inverting the polarization of the FEF closes the main path at the FTI-TI interface and opens that at the FTI-vacuum interface. Hence, the spin-down wave packet can now pass through the FTI and leaves through the Φ_{\downarrow}^+ exit channel (Fig. 4.12b). Transmission through the FTI is again perfect for the biggest part of the bulk gap (see Fig. 4.13). Only at the lower bulk gap edge, the wave packet is still reflected into the counter propagating channel because of the additional edge states at the FTI-TI interface. The low group velocity in these states requires again long propagation times (about $\tau = 10000 \frac{1}{\text{eV}}$) in order to detect the majority of the reflected wave packet.

The dispersion at the interface of two FTIs is similar to that of an FTI-TI interface. As a result, at such an interface, spin-up and spin-down wave packets propagate in the same direction (Fig. 4.14). Propagation into the opposite direction happens at the FTI-vacuum interfaces, like in Fig. 4.12b. Interchanging the magnetization directions of the two domains changes the paths, i.e. propagation from left to right happens along the domain wall and from right to left at the vacuum interfaces. Scattering probabilities are similar to Fig. 4.13, i.e. reflection happens only at the lower edge of the bulk gap.

The observation of chiral fermion modes at such a domain wall is consistent with the existence of similar states at a domain wall on the surface of a 3D TI [17]. Here, an instant

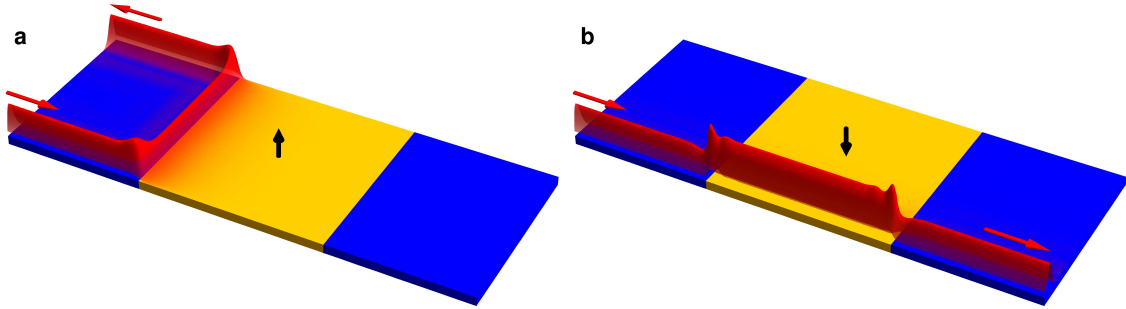


Figure 4.12: LDOS at $E_F = 0\text{eV}$ of the spin-down wave packet Ψ_{\downarrow}^+ encountering an FEF of strength $V_z = \pm 0.34\text{eV}$ that is spanning the whole width of the TI strip. (a) If the FEF is directed in positive z -direction, the wave packet is reflected into the counter propagating Φ_{\downarrow}^- exit channel. (b) An FEF in negative direction can be traversed by the spin-down wave packet, just like the positive FEF can be traversed by a spin-up wave packet (Fig. 4.11). Thus, the incoming wave packet remains at the same TI edge and leaves through the Φ_{\downarrow}^+ exit channel. Figure (a) taken from Ref. [1].

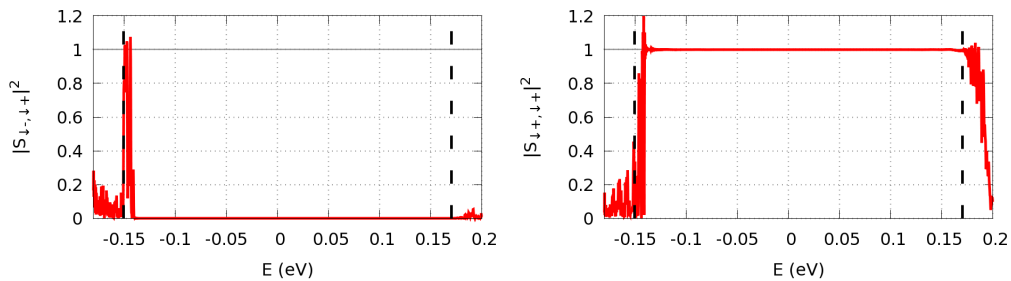


Figure 4.13: Full reflection- (left) and transmission-spectrum (right) of the spin-down wave packet Ψ_{\downarrow}^+ at a negative FEF that spans the full width of the TI strip, as shown in Fig. 4.12b. At the lower edge of the bulk gap, the wave packet is reflected by the FTI into the counter propagating spin-down channel at the opposite edge, while the rest of the bulk gap shows perfect transmission. The scattering matrix was calculated after a propagation time of $\tau = 10000 \frac{1}{\text{eV}}$. At lower propagation times, only a small part of the reflected wave packet is detected due to the low group velocity in edge states at the FTI-TI interface.

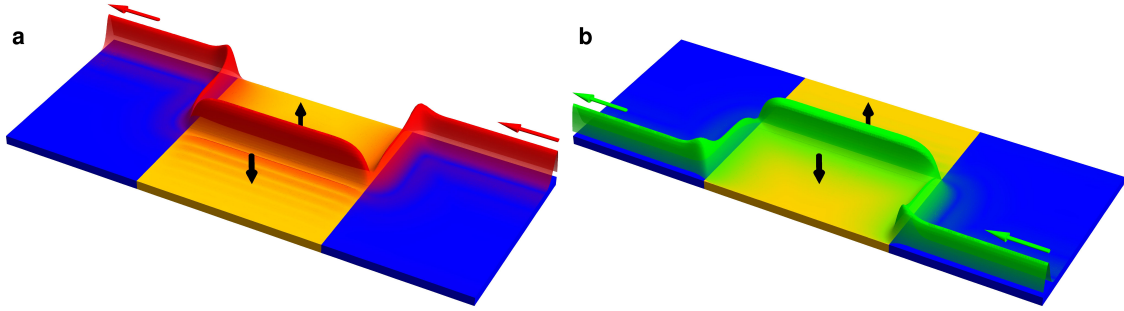


Figure 4.14: At a domain boundary, both spin-down (a) and spin-up (b) wave packets can only propagate in one direction along the boundary. Propagation into the opposite direction happens along the FTI-vacuum interface, analog to Fig. 4.12b. Figure (b) taken from Ref. [1].

inversion of the magnetization at the domain wall was assumed. The effect of a rotation via an in-plane magnetization is discussed in section 4.5.1.

4.3.2 In-plane field

So far, only FEFs perpendicular to the surface plane were considered in transport calculations, i.e. devices with a local QAH state. In such a device, the two pseudo-spin states are completely decoupled. As has been shown in Fig. 4.6, an in-plane field opens a gap in the edge state dispersion and couples the afore decoupled pseudo-spin states in the Hamiltonian. A local FEF with in-plane polarization may therefore give rise to spin-flip scattering and can block wave packets of both spin states due to the gap opening.

The scattering probabilities of the spin-down wave packet Ψ_{\downarrow}^+ encountering a local FEF with $V_y = 0.5M_{2D}$ are shown in Fig. 4.15. As has been shown in Fig. 4.6b, such a field reduces the bulk gap to about half its original size. Outside this reduced bulk gap, the wave packet is strongly scattered into bulk states and partly detected, through re-scattering into edge states, in all four exit channels. In this energy range, the scattering probabilities diverge because of a Fourier transformation of strongly varying values in combination with a large normalization factor. It is therefore a numerical artifact and of no physical meaning. Inside the reduced bulk gap, the scattering probabilities basically split into two parts. In the upper part of the bulk gap, the FEF opens a gap in the edge state dispersion, so the wave packet cannot pass. It is therefore reflected at the TI-FEF interface (Fig. 4.16a+b). However, in contrast to the case with an out-of-plane FEF, there are no edge states at the TI-FEF interface. So, the wave packet changes its spin and is almost completely scattered into the Φ_{\uparrow}^- exit channel. Only a tiny part tunnels through the FEF (Fig. 4.16a) because edge states penetrate significantly into the FEF on a length scale bigger than half the FEF width of 128 lattice sites so that edge states from opposite sides of the FEF overlap.

Below this gap, the wave packet is still mainly transferred through the FEF with small energy dependent reflections of increasing amplitude towards the gap. These Fabry-Pérot type

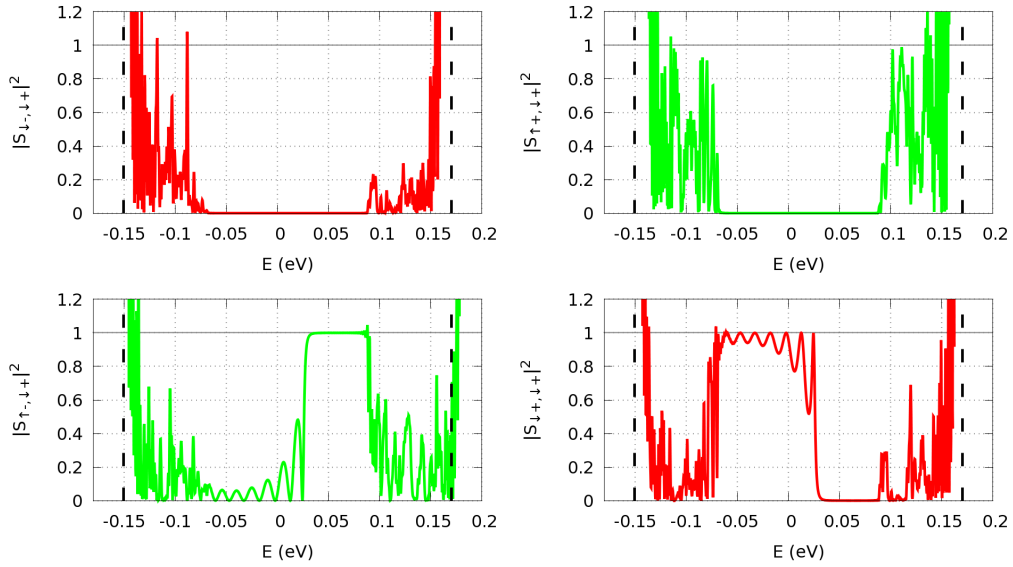


Figure 4.15: Scattering probabilities of the incoming wave packet Ψ_{\downarrow}^+ at a local FEF with $V_y = 0.5M_{2D}$. Inside the reduced bulk gap, scattering happens only into the two exit channels at the bottom edge. For energies within the edge state band gap, the wave packet is reflected with spin-flip into the Φ_{\uparrow}^- exit channel at the same edge. Below this gap, the wave packet is mainly transmitted through the FEF into the Φ_{\downarrow}^+ exit channel. Outside the reduced bulk gap, the wave packet is scattered into bulk states and is in parts detected in all exit channels. Values bigger than one are artifacts of a Fourier transformation of strongly varying values. The evolution time was $\tau = 5000 \frac{1}{\text{eV}}$.

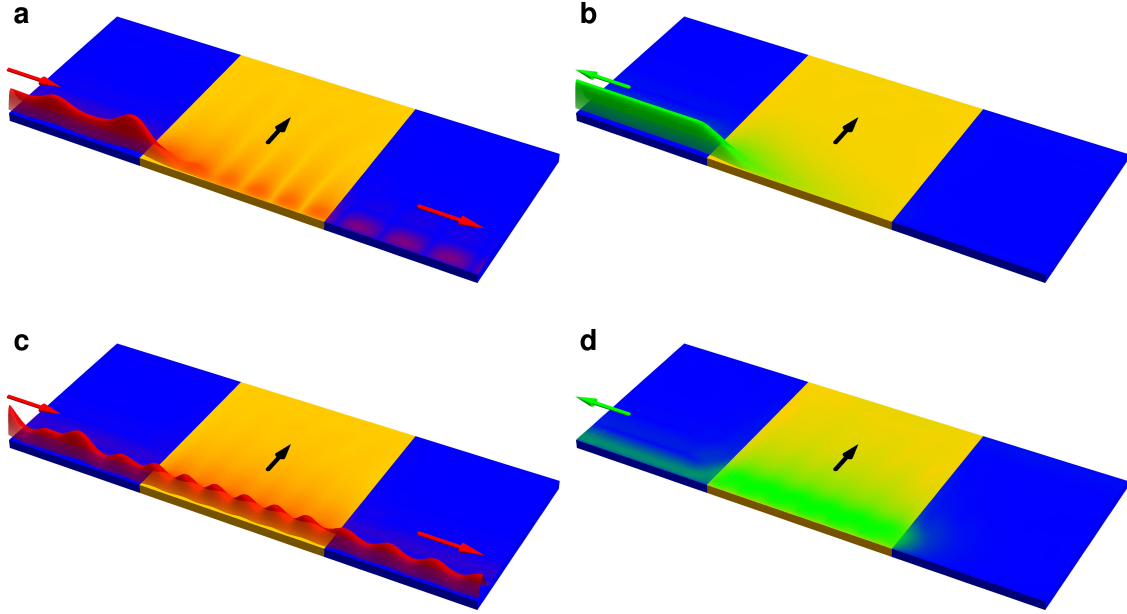


Figure 4.16: LDOS at an FEF with y -magnetization of strength $V_y = 0.5M_{2D}$. (a)+(b) The Fermi level is chosen as $E_F = 0.05\text{eV}$, within the edge state band gap. Due to an overlap of edge states, part of the wave packet tunnels through the FEF. (c)+(d) At the Fermi level $E_F = -0.05\text{eV}$, the wave packet is largely transferred through the FEF. Especially inside the FEF, interferences of the repeatedly reflected wave packet can be clearly seen.

resonances originate from interferences of reflected parts of the wave packet within the FEF [8, 82, 83], as can also be seen in the LDOS in Fig. 4.16c+d. The peak positions of the transmission spectrum coincide with discrete energy levels within the FEF and therefore narrow with increasing width of the FEF.

The above observations are quantitatively independent of the sign of the FEF and qualitatively independent of the in-plane direction of the field (see Fig. 4.17). Additionally, the FEF acts in the same way on spin-up and spin-down states. A spin-up wave packet Ψ_{\uparrow}^+ moving from left to right at the upper edge shows the same energy dependence in reflection and transmission as the spin-down wave packet at the lower edge, of course with opposite spin. The same holds for wave packets coming from the right.

4.3.3 Parameter stability

So far, only one parameter set for Bi_2Se_3 was investigated, and the question is whether or not the observed effects are independent of the parameter set. This investigation, however, will be restricted to the QAH phase.

Taking the other parameter set for Bi_2Se_3 ((a) in Tab. 3.1), the effective 2D parameter

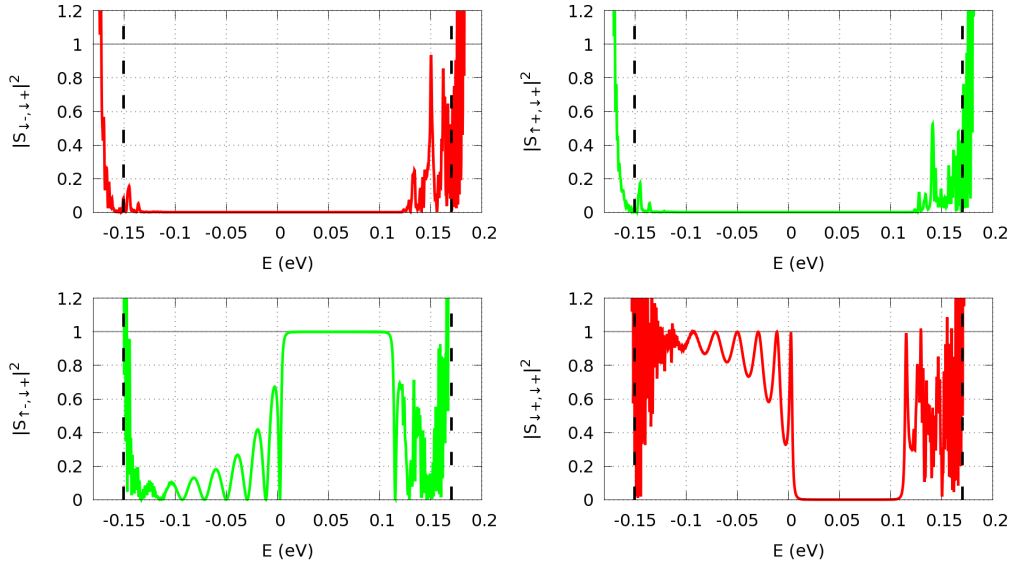


Figure 4.17: Scattering spectrum of the spin-down wave packet Ψ_{\downarrow}^+ at an FEF with x -magnetization of strength $V_x = 0.3M_{2D}$. The spectrum is qualitatively the same as that of the y -magnetized FEF shown in Fig. 4.15, only with an increased gap size and larger resonance amplitudes. The evolution time was $\tau = 5000 \frac{1}{\text{eV}}$.

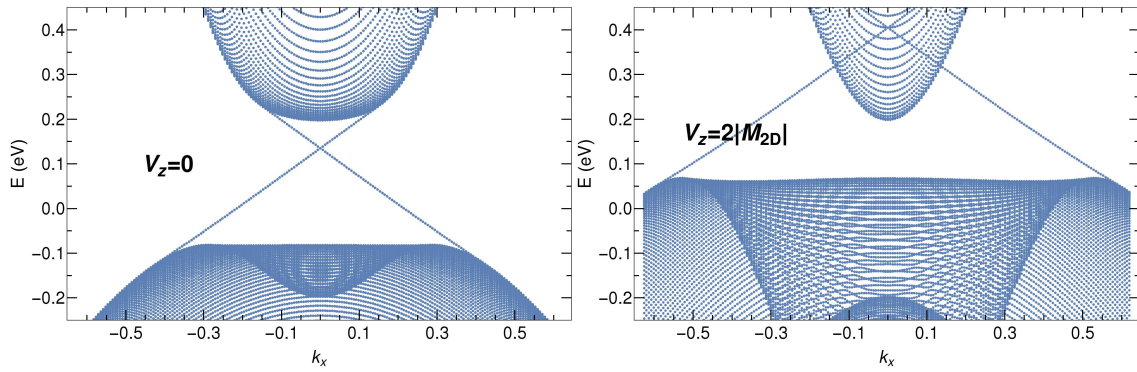


Figure 4.18: Numerical dispersion of a 2D Bi_2Se_3 sheet (parameter set (a)) in the normal state ($V_z = 0$) and QAH state ($V_z = 2|M_{2D}| \approx 0.4\text{eV}$). In the QAH state, bulk states from the valence band are pushed up in energy with increasing FEF.

4 Pure spin current devices and quantum transport calculations

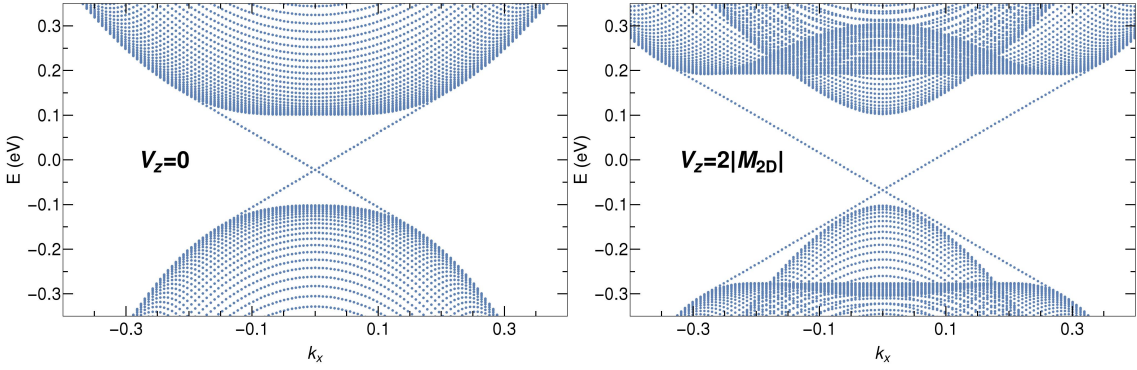


Figure 4.19: Numerical dispersion of a 2D Sb_2Te_3 sheet in the normal state ($V_z = 0$) and QAH state ($V_z = 2 |M_{2D}| \approx 0.2\text{eV}$).

Eq. (3.19) for M_0 is $M_{2D} = M_0 + M_1 \left(\frac{\pi}{L_z}\right)^2 \approx -0.198\text{eV}$ for $L_z = 15$. The first difference between parameter set (a) and (b) can be seen in the dispersion (Fig. 4.18). Without FEF, the edge state dispersion is basically the same, only that most of the bulk bands of the valence band now have a minimum at $k_x = 0$. When the material is driven into the QAH state by adding an FEF of strength $V_z = 2 |M_{2D}|$, the bulk gap spans only the upper half of the original bulk gap and the crossing of the edge state bands happens at higher energies, inside the conduction band. An increase of the FEF pushes the valence bands up even further and makes the overlap of the gaps of QSH and QAH state even worse. Another difference can be found by looking at the edge states. For the parameter set (b), edge states moving clockwise had only contributions from orbital $1 \uparrow$ and $2 \downarrow$, where $1 \uparrow$ was dominant. Now, these states have only contributions from $1 \downarrow$ and $2 \uparrow$, where $2 \uparrow$ is dominant, i.e. the direction of the pseudo spin remains the same. This is consistent with the analytical approximation in section 3.2. The degree of spin polarization $p = |C_2/M_2| \approx 0.68$ is much higher than for the other parameter set. As analog changes apply to all other edge states, changes in a quantum transport calculation are only a matter of the deviating dispersion. For $V_z = -2 |M_{2D}|$, a wave packet starting at the position Ψ_{\downarrow}^+ is only transferred through the magnetic barrier for energies within the smaller gap. For all other energies, it is scattered into bulk states. Interestingly, for $V_z = 2 |M_{2D}|$, the wave packet is perfectly reflected towards the opposite edge by a barrier spanning the full TI width, although the gap at the TI-FTI interface has about the same size as that at the vacuum interface.

For Sb_2Te_3 , the effective 2D parameter for a sheet thickness of 15 layers would be only $M_{2D} \approx -0.0096\text{eV}$, resulting in a very tiny gap. Therefore, the thickness is increased to 20 layers, resulting in $M_{2D} \approx -0.1\text{eV}$. For these parameters, the dispersions (Fig. 4.19) are very similar to those of the Bi_2Se_3 parameter set (b). In the QAH phase, all bulk states are removed from the initial bulk gap and the crossing of the edge state bands happens inside the gap. Higher fields now result in an even larger gap. Consequently, simulations with these material parameters show perfect transmission and reflection properties. Concerning the spin of the edge states, clockwise moving edge states have only contributions from orbital $1 \downarrow$ and

2 ↑. The dominance of the first orbital, however, now results in a negative pseudo spin for these states, with an absolute value of $p \approx 0.22$.

Results for in-plane fields are qualitatively equal to those in section 4.3.2 for both parameter sets.

The effective parameter M_{2D} , which originates from a quantum well approximation of a thin TI sheet, accounts only for the bulk gap and in that decreases with decreasing sheet thickness. So, when M_{2D} changes sign, the material becomes a trivial insulator. On the other hand, the hybridization gap of surface states from the z -surface should increase with decreasing thickness (see Ref. [46]). This seems to be a contradiction and raises the question, to what extent or in what thickness range this parameter yields a realistic effective gap size for the thin sheet. To overcome this issue and to get a more realistic picture, TI sheets with a finite thickness that do not need a quantum well approximation will be studied in section 4.5.2.

4.4 Pure spin current devices

Now that it is known how electrons in edge states propagate in the presence of local FEFs, this information can be used to construct spintronic devices. Specifically, the goal is to construct devices that create, detect and switch pure spin currents. For that purpose only local FEFs with out-of-plane polarization are used since they conserve pseudo spin and bulk gap size. The size of device structures is only a matter of the spatial extend of edge states. In the present case, edge states are extended over about 50 lattice sites (Fig. 4.3) and the width of the TI strips was correspondingly chosen as $Y = 128$ lattice sites with FEFs of size 128×128 or 128×64 , corresponding to edge lengths of about 26.5nm – 53nm. Some newly detected 2D materials with large band gaps show edge states with a spatial extend of only about 1nm [51], potentially allowing very small device structures. The presented devices have been published in Ref. [1].

4.4.1 Generator

Any electron propagating in topological edge states carries a defined (pseudo) spin so that a charge current has always a superimposed spin current. Depending on the direction of the charge current, the spin current transports either spin-up or spin-down, where, in the case of Bi_2Se_3 , a clockwise current transports spin-up and a counterclockwise current spin-down. Thus, by driving charge currents of equal magnitude in both directions along the edge, the total charge current sums to zero, while a net spin transport remains, i.e. a pure spin current.

A possible device for creating pure spin currents in such a way is shown in Fig. 4.20. Charge currents are injected into and extracted from the TI (blue) via three metallic electrodes (gray). The extracting electrode in the middle is grounded. So, when a voltage V_g is applied between this electrode and the two outer injecting electrodes, charge currents will flow from the negative, injecting electrodes to the extracting one. By placing two FTIs (orange) of opposite z -polarity (denoted by black arrows) in front of the injecting electrodes, these currents are spin filtered and forced into the paths along the outer edge of the TI sheet. Only spin-down electrons can pass the lower, negative polarized FTI. They propagate counterclockwise through

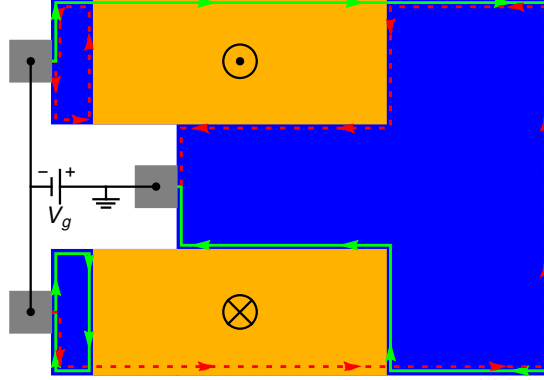


Figure 4.20: Schematic of the spin current generator. A voltage V_g , applied between two injecting and one extracting metallic electrode (gray) attached to a TI sheet (blue), gives rise to charge currents flowing along the edges of the TI. Two FTIs (orange) of opposite z -polarity act as spin filters on the injected currents and thereby block the direct current flow between electrodes. The resulting charge currents along the outer edge cancel each other but produce a net spin current flow. Spin-up and spin-down electron paths are indicated by green solid and red dashed arrow lines, respectively. The direction of the out-of-plane polarization of the FEFs is shown by black arrows. Taken from Ref. [1].

the device and then along the outer edge of the other, positive polarized FTI into the absorbing electrode. The same holds for spin-up electrons injected through the upper metallic electrode. In both cases, electrons of opposite spin are reflected by the FTI and then scattered with spin-flips at the metallic contacts. If the FTI is extended towards the metallic contact, only electrons with correct spin are injected in the first place. However, if the FEF is induced via the proximity effect, it is probably easier to produce devices with this small TI area to avoid an overlap of ferromagnetic insulator and metallic electrode.

The direct conversion of charge currents into spin currents makes the proposed device very efficient. Two electrons with a total charge of $2e$, flowing from the two injecting electrodes to the extracting one, transport a total spin of $p\hbar$ along the outer edge of the device, where $0 \leq p \leq 1$ is the spin polarization of the edge states. Thus, the conversion efficiency of the device [1]

$$\Theta = \frac{ej_s}{\hbar j_c} = 0.5p \quad (4.23)$$

is given by a quotient of spin current density j_s and charge current density j_c . This conversion efficiency can be compared to the spin Hall angle Θ_{SH} , which is used to quantify the conversion efficiency of the spin Hall effect. Taking the relatively low edge state polarization $p = C_2/M_2 \approx 0.35$ of the model used here, the conversion efficiency is $\Theta \approx 0.175$. This is already better than the best conversion efficiency of $\Theta_{SH} \sim 0.1$ [66] achieved with the spin Hall effect. Considering reported spin polarizations for different TI materials, ranging between about 0.3 and 1 for surface states on the top surface [39–42, 86–93], even much higher ef-

iciencies could be achieved. To give an accurate estimate of the efficiency, the actual spin polarization, especially for the side surfaces, has to be clarified. The other material parameters presented in Tab. 3.1 yield $\Theta \approx 0.34$ ($p \approx 0.68$) for Bi_2Se_3 (a) and $\Theta \approx 0.11$ ($p \approx 0.22$) for Sb_2Te_3 .

The spin currents are also very robust regarding spin-flip scattering. As long as there are no time-reversal symmetry breaking perturbations, spin-flip scattering is forbidden. However, in real devices there will always be perturbations like impurities or the Rashba effect (see further sections 4.5.3 and 4.5.4). These effects become especially relevant when devices get larger than the spin-flip mean free path of topological edge states, which is reported to be about $2\mu\text{m}$ [29, 63]. But even in these cases, where a single current along an edge may be destroyed, the pure spin currents remain very robust. First of all, whenever there are FTIs, channels for spin-up and spin-down electrons are spatially separated and spin-flip scattering is therefore not possible, even if there are impurities. Aside from FTIs, spin-flip scattering can happen, but the scattering probability of spin-up and spin-down electrons is the same due to reciprocity. So, the loss in spin-up electrons is the gain in spin-down electrons and vice versa. If there is only one scattering site, this is intuitively clear. Consider therefore two scattering sites with scattering probabilities γ_1 and γ_2 . An electron encountering a scattering site i is scattered with probability γ_i and transmitted with probability $(1 - \gamma_i)$. So, for electrons encountering the two scattering sites from the left, the fractions of all electrons moving to the left, in the middle and to the right after each scattering event are given by the following scheme (columns indicate the position, arrows the direction):

$$\begin{array}{ccc}
 \begin{array}{c} \leftarrow \\ \gamma_1 \end{array} & \begin{array}{c} \rightarrow \\ (1 - \gamma_1) \end{array} & \begin{array}{c} \rightarrow \\ (1 - \gamma_1)(1 - \gamma_2) \end{array} \\
 \begin{array}{c} \leftarrow \\ (1 - \gamma_1)^2 \gamma_2 \end{array} & \begin{array}{c} \leftarrow \\ (1 - \gamma_1) \gamma_2 \end{array} & \\
 & \begin{array}{c} \rightarrow \\ (1 - \gamma_1) \gamma_1 \gamma_2 \end{array} & \begin{array}{c} \rightarrow \\ (1 - \gamma_1)(1 - \gamma_2) \gamma_1 \gamma_2 \end{array} \\
 \begin{array}{c} \leftarrow \\ (1 - \gamma_1)^2 \gamma_1 \gamma_2^2 \end{array} & \begin{array}{c} \leftarrow \\ (1 - \gamma_1) \gamma_1 \gamma_2^2 \end{array} & \\
 & \begin{array}{c} \rightarrow \\ (1 - \gamma_1) \gamma_1^2 \gamma_2^2 \end{array} & \begin{array}{c} \rightarrow \\ (1 - \gamma_1)(1 - \gamma_2) \gamma_1^2 \gamma_2^2 \end{array} \\
 \vdots & \vdots & \vdots
 \end{array}$$

As the same diagram, with γ_1 and γ_2 interchanged, holds for electrons coming from the right,

4 Pure spin current devices and quantum transport calculations

the sum over all fractions of electrons moving from left to right between the scattering sites is:

$$\begin{aligned}
& (1 - \gamma_1) \sum_{n=0}^{\infty} (\gamma_1 \gamma_2)^n + (1 - \gamma_2) \gamma_1 \sum_{n=0}^{\infty} (\gamma_1 \gamma_2)^n \\
&= \sum_{n=0}^{\infty} (\gamma_1 \gamma_2)^n - \sum_{n=0}^{\infty} (\gamma_1 \gamma_2)^{n+1} \\
&= \sum_{n=0}^{\infty} (\gamma_1 \gamma_2)^n - \sum_{n=0}^{\infty} (\gamma_1 \gamma_2)^n + (\gamma_1 \gamma_2)^0 \\
&= 1
\end{aligned}$$

Analogously for the sum right to both scattering sites:

$$\gamma_2 + \gamma_1 (1 - \gamma_2)^2 \sum_{n=0}^{\infty} (\gamma_1 \gamma_2)^n + (1 - \gamma_1) (1 - \gamma_2) \sum_{n=0}^{\infty} (\gamma_1 \gamma_2)^n = \dots = 1$$

The results for the opposite directions are obtained by interchanging γ_1 and γ_2 . As this scheme can be easily extended to arbitrary numbers of scattering sites, spin-flip scattering does not affect the pure spin currents. It only increases the resistance of the device and thus the required voltage to drive these currents. The only condition is that the scattering probability of each scattering site is less than one.

4.4.2 Detector

As pure spin currents cannot be detected directly by measurement instruments, they have to be transformed into charge currents. Usually, this is done by the inverse spin Hall effect. In the present case, however, where the spin current results from charge currents in two counter-propagating spin channels, a simpler way is to split the spin current back into its two parts. These parts can be measured separately by conventional measurement instruments as voltage drops with respect to the common ground with the spin current generator. The detector shown in Fig. 4.21 is therefore basically an inverted version of the generator. Two FTIs of opposite z -polarization separate one spin component each by blocking the other one. A positive FTI blocks the spin-down component, and the spin-up component can be measured as a voltage drop $V_{d\uparrow}$. Analogously, the spin-down component yields a voltage drop $V_{d\downarrow}$ when the spin-up component is blocked by a negative FTI. Local measurements of this kind have already been successfully performed on 2D TIs [94] and FTIs [20, 56, 57]. A pure spin current is characterized by $V_{d\uparrow} = V_{d\downarrow}$, and the net spin transport can be calculated from the voltage drop with additional information on device resistance and edge state spin polarization. Again, the small TI areas right to the FTIs are not generally necessary. When they are present, the metallic electrodes enable spin-flip scattering processes and thereby inject electrons with opposite spin into the TI. However, only electrons with the correct spin can reenter the rest of the device since the FTI blocks the other component.

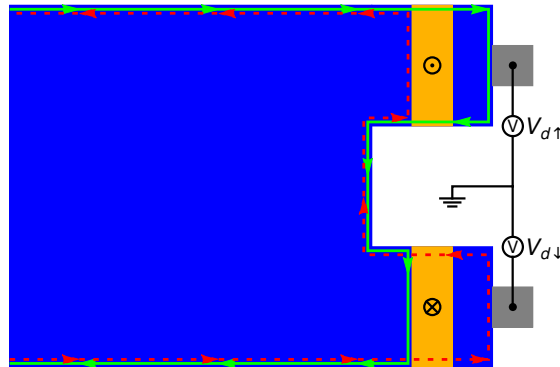


Figure 4.21: Schematic of the spin current detector. The detector works like an inverted generator. A spin current is split into its two counter propagating spin parts by local z -polarized FTIs of opposite polarity. By this, the charge flow in spin-up and spin-down channels can be measured separately as voltage drops $V_{d↑}$ and $V_{d↓}$ with respect to the common ground with the generator. For a pure spin current, these voltages have to be equal. Taken from Ref. [1].

4.4.3 Transistor

Having a generator and detector for pure spin currents, the last device needed for applications is a transistor. A transistor for pure spin currents must be switchable between two states. In the “off”-state, it has to reflect both spin components, and in the “on”-state, it must be transmitting. Both states must preserve the spin current in the rest of the device. To realize this by using only out-of-plane FEFs, at least four domains in two blocks are needed. A single block with either positive or negative z -polarization can only block spin-down or spin-up electrons, respectively. So, for realizing the “off”-state, a sequence of two blocks with opposite polarization is needed. These blocks may be spatially separated to avoid domain wall structures. In Fig. 4.22a, the left block has negative z -polarization and blocks the spin-up part of the spin current. The right block has positive z -polarization and blocks the remaining spin-down part. To make these two blocks passable in the “on”-state, a half of each block has to be switchable to the opposite polarization such that the blocks form domain walls in the middle, like in Fig. 4.14. It is thereby unimportant which half of each block is switched. Consider for example the case where the top domains of both blocks have positive and the bottom domains negative polarization (Fig. 4.22b). Then, electrons in both spin states can propagate from left to right along the outer edges of the device and from right to left along the common channel at the domain wall.

Since spin-up and spin-down channels are not separated at the domain wall, scattering between these channels, e.g. by magnetic impurities, is possible. However, the scattering rates from spin-up into spin-down channels and vice versa should be the same and therefore compensate each other. Examples that include scattering processes between these two channels are shown in section 4.5.1 and 4.5.4.

A simple idea for simultaneously switching both magnetic domains is shown in Fig. 4.22c. A

4 Pure spin current devices and quantum transport calculations

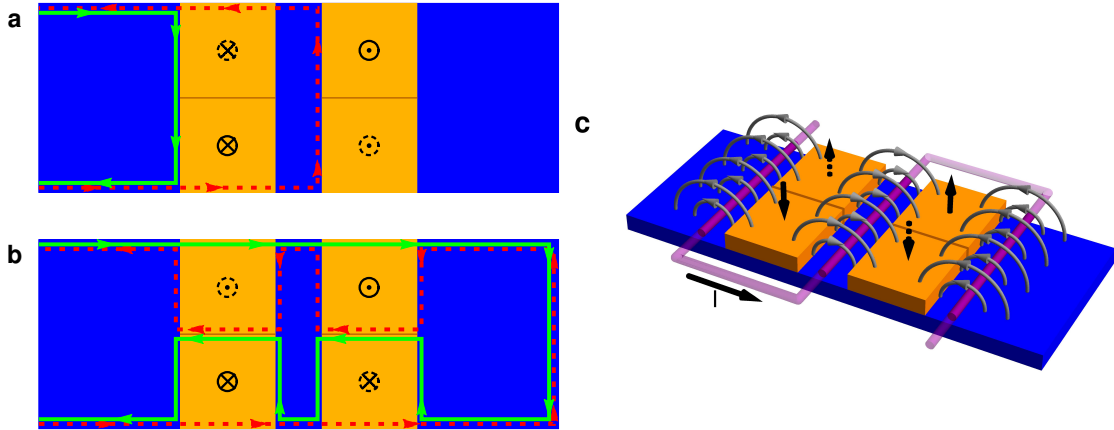


Figure 4.22: The spin transistor device has two states. **(a)** In the “off”-state, two spatially separated FTI blocks of opposite z -polarization block both spin components of the spin current. **(b)** By inverting the magnetization of a half of each FTI block, the barriers become passable in both directions for both spin components. The polarization of switchable domains is indicated by dashed black arrows. Domains with solid arrows are fixed. **(c)** The magnetic domains may be switched simultaneously by the magnetic field (gray), induced by a current through the wire (purple). Taken from Ref. [1].

current through a wire wound around the two FTI blocks induces a magnetic field of opposite polarity for the two switchable domains, so both domains can be switched at the same time. For that purpose, the polarity of the other two domains has to be fixed, i.e. they have to have a higher coercive field. A conventional way to achieve this is exchange bias pinning with an antiferromagnetic material [95].

The magnetic field at a distance x to a wire with current I is $H(x) = \frac{I}{2\pi x}$. Assume a distance of $d = 25\text{nm}$ between wire and FTIs, which have a width of $d = 25\text{nm}$ as well. So, the effective field created by two wires on both sides of an FTI is $H_{\text{eff}}(x) = \frac{I}{2\pi} \left(\frac{1}{x} + \frac{1}{3d-x} \right)$ with the field minimum $H_{\text{min}} = \frac{I}{2\pi} \frac{4}{3d}$ in the middle of the FTI. Reported coercive fields are $H_c \approx 1440 \frac{\text{A}}{\text{m}}$ for EuS (a ferromagnetic insulator) on Bi_2Se_3 [60] and $H_c \approx 8000 \frac{\text{A}}{\text{m}}$ for Fe on Mn doped Bi_2Te_3 [96]. To create fields of such strength by a single wire loop, a relatively high current of $I = \frac{3\pi d}{2} H_{\text{min}} \sim 0.2\text{mA} - 1\text{mA}$ is required, potentially causing heat problems.

Alternatively, the domains can be switched by an external field, e.g. with a write head like in a hard disk drive. This may, however, be slower if the write head has to move from transistor to transistor, and if it is not possible to switch both domains at the same time, charge currents will flow along the right edge of the transistor device during the switching process. It is therefore worth thinking about alternatives for the transistor device that can ideally be switched all electrically.

A possibility would be to use a single FEF block with in-plane magnetization, which has energy dependent transmission properties. By applying a gate voltage, the Fermi level could

then be shifted within the bulk gap between the transmitting and reflecting part. However, because of the resonances in the transmitting part, the transistor would be less efficient than the one using only out-of-plane fields, and as the already reduced bulk gap is split into two parts, the maximal operation temperature is much smaller. If only the reflecting part of an in-plane FEF is to be used as an insulating barrier, the FEF has to be disengageable to make the barrier transmitting in the “on”-state. Generally, a problem could be that TIs of the Bi_2Se_3 class show out-of-plane ferromagnetic anisotropy [56], so it may be problematic to achieve a stable in-plane FEF.

A new class of materials called topological crystalline insulators is protected by mirror symmetry. This symmetry can be broken by simply applying a gate voltage and thereby opening a gap in the edge state dispersion [97]. If spin current generator and detector can be realized in these materials as well, they might be a great alternative.

4.5 Towards more realistic modeling

In the previous sections, it has been shown that FEFs can be used to steer currents in edge states of 2D TIs by means of the QAH effect and that this can be used to create, switch and detect pure spin currents. However, these results were obtained with ideal conditions, and the question is how more realistic device modeling affects the obtained results. Real devices will contain domain wall structures (section 4.5.1) whenever two magnetic domains are in contact and will also have material imperfections that result in locally varying electrostatic potentials and edges (section 4.5.3). Aside from neglecting such effects, a big simplification was that the TI was modeled by a real 2D Hamiltonian under the assumption of inversion symmetry. Since materials of the Bi_2Se_3 class are 3D TIs that show 2D behavior only in thin films where the surface states from the top and bottom surfaces hybridize, simulations with a finite thickness, based on the full 3D Hamiltonian should be more accurate (section 4.5.2). This 3D modeling further enables the examination of effects like broken structural inversion symmetry by an insulating substrate (section 4.5.4) and spatially inhomogeneous exchange fields due to the proximity effect (4.5.5). Except for a 2D domain wall structure, these effects have not been studied in Ref. [1].

4.5.1 Domain walls

Whenever two magnetic domains of opposite magnetization are in contact, a domain wall structure forms at their interface. At the domain wall, the magnetization rotates continuously over a finite length scale from one direction to the other. Different variables thereby determine whether the rotation happens more in the domain wall plane ($\downarrow \otimes \uparrow$ or $\downarrow \odot \uparrow$, Bloch-type) or perpendicular to the plane ($\downarrow \rightarrow \uparrow$ or $\downarrow \leftarrow \uparrow$, Néel-type) [98]. Concerning the spin current transistor, where two ferromagnetic domains with opposite z -polarization touch, the FEF will have in-plane components in between. As an in-plane FEF is known to open a gap in the edge state dispersion and to give rise to spin-flip scattering, this may alter the functioning of the device. Here, it is shown that, although spin-flip scattering happens, the overall device functioning is unaffected by a domain wall structure.

4 Pure spin current devices and quantum transport calculations

The following results have been discussed in the supplementary material of Ref. [1], however with the wrong representation of the spin matrices Σ_x and Σ_y for the used Hamiltonian. Here, as the Hamiltonian contains the real spin, the spin matrices are correct. A direct comparison of the different results shows that the Néel wall features presented in Ref. [1] equal those of the Bloch wall presented here and vice versa.

In the transistor device, a domain wall is located at $y = y_0$ parallel to the x -axis, where the z -magnetization switches from negative ($y < y_0$) to positive ($y > y_0$). The position dependent direction vector of the FEF then reads [99]

$$\mathbf{n}_B(y) = \left(\pm 1 / \cosh \frac{y - y_0}{\xi}, 0, \tanh \frac{y - y_0}{\xi} \right) \quad (4.24)$$

for a Bloch wall and

$$\mathbf{n}_N(y) = \left(0, \pm 1 / \cosh \frac{y - y_0}{\xi}, \tanh \frac{y - y_0}{\xi} \right) \quad (4.25)$$

for a Néel wall. Depending on the \pm sign, rotation of the magnetization is either via a positive or negative in-plane magnetization. As the main results, i.e. dispersion and scattering rates, are independent of the sign, it is chosen to be $+$. The width of the domain wall, characterized by ξ , is according to Wakatsuki *et al.* [99] only a few lattice sites and is adapted to be $\xi = 4$. The results, however, are qualitatively independent of the domain wall width as long as it is small compared to the spatial extend of the edge states.

Dispersions for both types of domain walls are shown in Fig. 4.23. In both cases, there is a twofold degenerate edge state band with positive slope that belongs to the outer interface of the TI with vacuum and is unaffected by the domain wall. Other edge state bands, i.e. those with negative slope, are located at the domain wall. For a Bloch wall, the edge state band is again twofold degenerate and not much different from that without in-plane field. However, the edge states are no longer z -polarized as they have contributions from all four orbitals, as shown exemplarily for $k_x = 0$ in Fig. 4.24. So, the pseudo spin of an electron entering the domain wall is no longer conserved. In the case of a Néel wall, the edge state bands at the domain wall split and additional bands emerge at the lower bulk gap edge. Band separation as well as the number of additional bands increases with increasing domain wall width ξ . The edge states have again contributions from all orbitals.

Wave packets propagating along the domain wall are scattered into both exit channels with the same propagation direction (dashed and dotted lines in Fig. 4.25 and 4.26). The exact energy dependence of the individual scattering probabilities thereby depends on the length of the domain wall. Because spin-up and spin-down wave packets are scattered symmetrically, the total transmission into the two exit channels (solid lines) still sums to unity for almost the full energy range of the bulk gap. Only at the lower bulk gap edge, reflection into the two exit channels with opposite propagation direction happens due to the additional edge states at the FTI-TI interface (compare Fig. 4.4) and, in the case of the Néel wall, also at the domain wall. All in all, a domain wall structure leaves the functioning of the proposed transistor device basically unaffected.

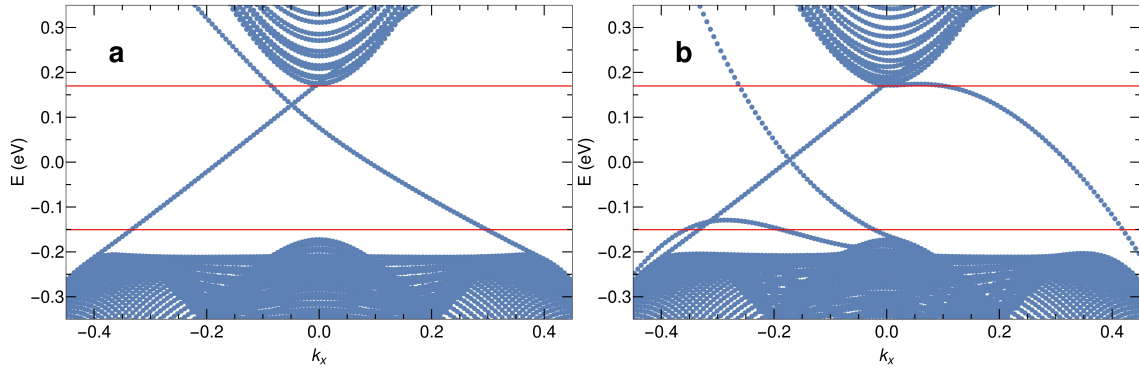


Figure 4.23: Though a domain wall features in-plane polarizations, no gap opens in the edge state dispersion. The dispersion of a Bloch wall is shown in **(a)**. It has two twofold degenerate bands of edge states, from which those with positive slope are located at the FTI-vacuum interface and those with negative slope at the domain wall. The dispersion of a Néel wall shown in **(b)** is somewhat more complex. Edge state bands spanning the bulk gap with a positive slope are again the twofold degenerate edge states at the vacuum interface. The degeneracy of the states at the domain wall is now lifted, but they still have only negative slope inside the bulk gap. At the lower bulk gap edge, additional states emerge that are only weakly located at the domain wall. Red lines indicate the bulk gap of a pure TI.

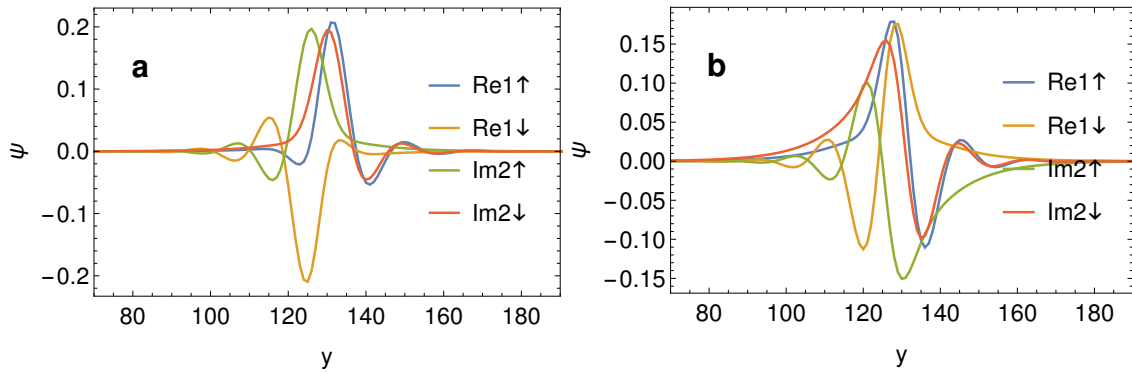


Figure 4.24: Edge states at a Bloch wall, exemplarily shown for $k_x = 0$. **(a)** and **(b)** correspond to edge states of the two degenerate bands. As these edge states have contributions from all orbitals, i.e. not only $1 \uparrow$ and $2 \downarrow$ or $1 \downarrow$ and $2 \uparrow$, they are no longer z -polarized. Only nonzero components are shown.

4 Pure spin current devices and quantum transport calculations

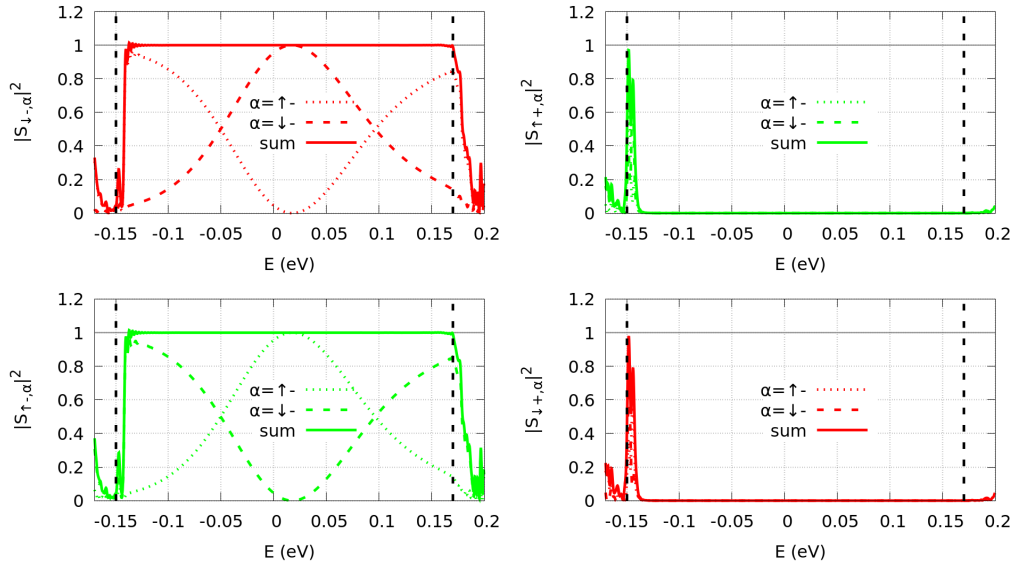


Figure 4.25: Scattering probabilities of the wave packets Ψ_{\downarrow}^{-} and Ψ_{\uparrow}^{-} at a Bloch wall of width $\xi = 4$. As these wave packets are scattered symmetrically, the total transmission, i.e. the sum, is unaffected by the domain wall. At the lower bulk gap edge, both wave packets are largely reflected by the FEF.

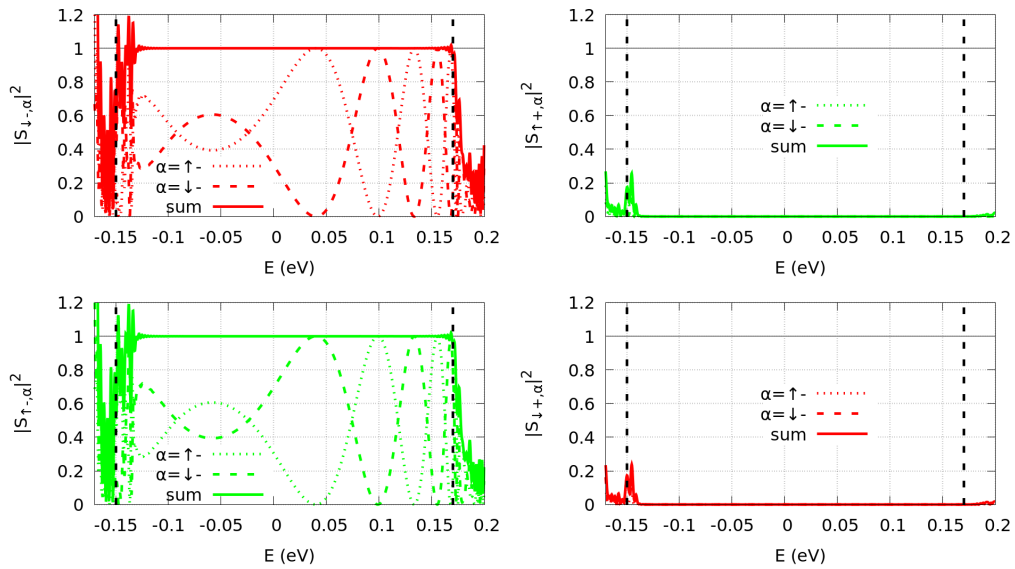


Figure 4.26: Scattering probabilities at a Néel wall, analogous to Fig. 4.25. As the additional bands at the domain wall reach deeper into the bulk gap than those at the FTI-TI interface, scattering happens on a wider energy range. Reflection, however, seems to be reduced.

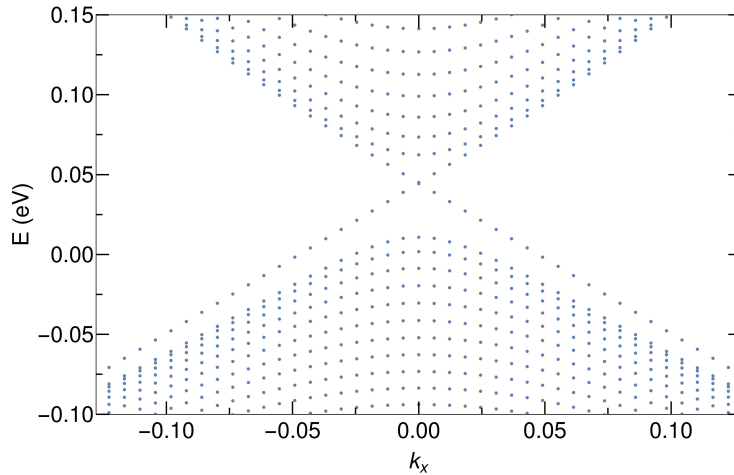


Figure 4.27: Numerical Dispersion of 15 mono-layers of Bi_2Se_3 (parameter set (b)). The surface states located at the z -surfaces are hybridized and opened a gap of about 52meV. Due to the finite width of 256 lattice sites in y -direction, the 1D edge states inside this gap show a small hybridization gap as well.

4.5.2 Finite thickness

So far, all calculations were performed with a strictly 2D Hamiltonian, where the k_z wave vector was replaced by its mean value $\langle k_z \rangle = 0$ for a symmetric quantum well potential [55]. This had the consequence that the Hamiltonian was completely decoupled into two sub blocks, forming the two pseudo spin states. In reality, however, TIs of the Bi_2Se_3 class are 3D TIs. Only in a finite range of thicknesses, when surface states of top and bottom surface are hybridized but the material is still topologically nontrivial, they become 2D TIs within the hybridization gap. For Bi_2Se_3 , Y. Zhang *et al.* [46] showed by ARPES measurements that surface states hybridize below 6 quintuple layers (QL) and vanish at 2 QL, i.e. the TI becomes a trivial insulator. The biggest nontrivial hybridization gap of 0.138eV is achieved at 3 QL, i.e. 15 mono-layers. This is less than half the bulk gap of the effective 2D Hamiltonian. Thus, using the full 3D Hamiltonian Eq. (3.11) in real space with 15 layers in z -direction should give a more realistic description of the thin TI sheets considered here.

For Bi_2Se_3 (parameter set (b)), the numerical dispersion (Fig. 4.27) for 15 mono-layers shows a hybridization gap of only about 52meV, i.e. less than half the measured gap but consistent with calculations by Linder *et al.* [47]. It has, however, to be considered that the model is based on a free standing TI, i.e. a TI surrounded by vacuum on all sides. In measurements, however, the TI resides on a substrate and is subjected to residual gas atoms in the vacuum. How this may affect band structure and transport properties is discussed in section 4.5.4.

Unfortunately, the other parameter set for Bi_2Se_3 shows no edge states in this thin film limit, independent of the film thickness. To examine the reason for this absence, the absolute values of parameter set (a) are linearly tuned into those of parameter set (b) while keeping

4 Pure spin current devices and quantum transport calculations

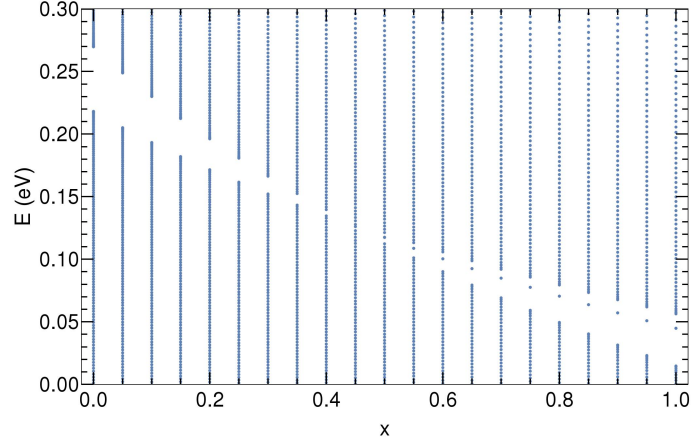


Figure 4.28: Numerical eigenvalues of a 15 mono-layer Bi_2Se_3 system at $k_x = 0$ as the parameters are linearly tuned from set (a) ($x = 0$) to (b) ($x = 1$). Only the sign is kept corresponding to set (a). The width of the system is $Y = 1024$ lattice sites. At about $x \approx 0.45$, the system undergoes a quantum phase transition from a topologically trivial to a nontrivial phase.

the signs. When A is a parameter of set (a) and B the corresponding parameter of set (b), the tuned parameter is given by $C(x) = \text{sign}(A)(|A|(1-x) + |B|x)$. Figure 4.28 shows the corresponding numerical eigenvalues at $k_x = 0$ of a system with 15 mono-layers and $Y = 1024$ lattice sites when the parameters are tuned from (a) ($x = 0$) to (b) ($x = 1$). At about $x \approx 0.45$, the hybridization gap closes and reopens at higher values with edge states inside the gap. So, the two parameter sets represent two topologically distinct phases in the thin film limit, where parameter set (a) is topologically trivial. Other theoretical work investigating the thin film properties using the model by Zhang *et al.* [32] used the same parameter set (b) [47–49]. Experimental data supporting the existence of edge states could not be found.

In the following, the focus will be on Sb_2Te_3 , which has multiple reasons. First, the QAH effect has been measured in doped $(\text{Sb,Bi})_2\text{Te}_3$ [56, 57], which should have more resemblance to Sb_2Te_3 than to Bi_2Se_3 . For Bi_2Se_3 , there are no known measurements of topological edge states in the 2D limit or a QAH effect. So, as one of the parameter sets yields a topologically trivial behavior, it would be wise to first check whether or not Bi_2Se_3 thin films feature protected edge states. However, the main reason is that Bi_2Se_3 (parameter set (b)) is computationally somewhat difficult. The edge state bands in Bi_2Se_3 touch the conduction bands in close vicinity to the gap edge, making the localization of edge states inside the hybridization gap worse than in Sb_2Te_3 . To compensate this, the width of the TI sheet has to be increased. Additionally, the overlap of edge and bulk states at the upper gap edge has to be chosen relatively small, and therefore, the scattering spectrum inside the gap is stronger distorted by the Gibbs phenomenon. Apart from this distortion, the results are qualitatively consistent with those for Sb_2Te_3 .

The hybridization gap of Sb_2Te_3 ($\sim 43\text{meV}$) is even smaller than that of Bi_2Se_3 , but the Dirac point is placed approximately in the middle of the gap, and the edge state bands touch

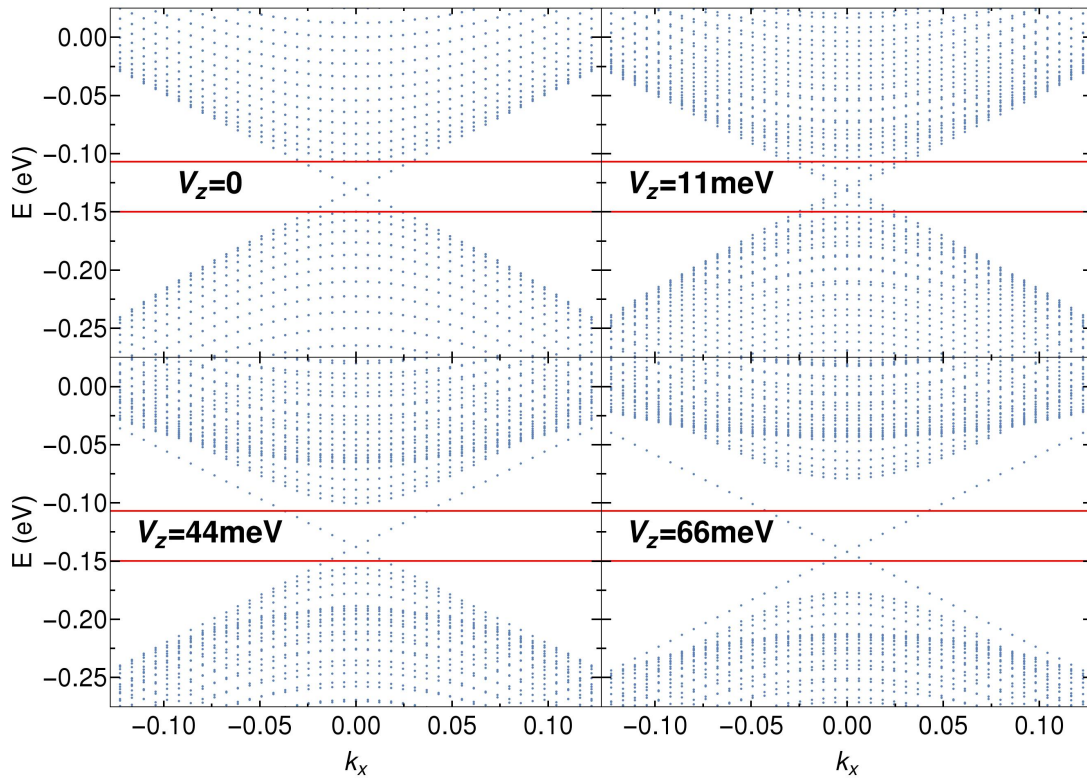


Figure 4.29: Numerical dispersion of 15 layers Sb_2Te_3 with varying out-of-plane FEFs V_z . Without FEF, the hybridization gap has a size of about 43meV (marked by red lines). With FEF, two of the four edge state bands open a gap, while the other two remain basically unchanged. In contrast to the 2D case, the system enters a QAH state already at arbitrarily small fields. When the FEF exceeds the size of the hybridization gap, two of the four edge states are completely removed from the gap. Even higher fields result in an increased gap size.

4 Pure spin current devices and quantum transport calculations

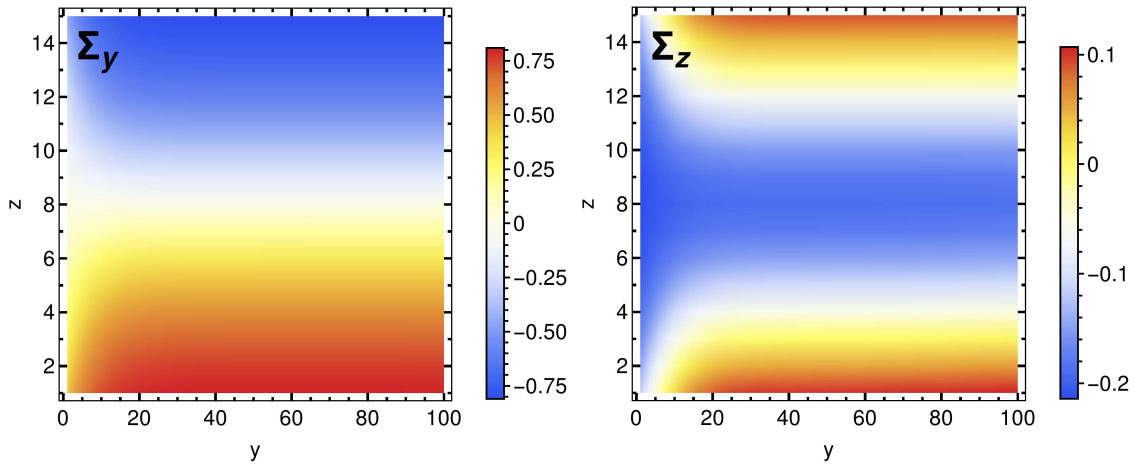


Figure 4.30: Local spin expectation values of an Sb_2Te_3 edge state in the upper band at $k_x \approx -0.031$. The edge state is located at the lower edge ($y = 0$) and moves in negative x -direction (clockwise movement). The expectation value of Σ_x is zero. Note, that the shown Σ_z expectation value resembles a pseudo spin as the two orbitals have opposite spin. The sum of the absolute values of both orbitals sums to one with the Σ_y expectation value.

the bulk bands in greater distance to the gap edges (see Fig. 4.29). So, the edge states are better localized. Wang *et al.* [37] examined thin films of Sb_2Te_3 via ARPES, but the hybridization gap could not be measured because the Fermi level was located approximately in the middle of the bulk gap. For applications, however, it is beneficial that the Fermi level lies inside the gap without the need of further tuning via chemical doping or application of a gate voltage. The spin of the edge states is now not strictly oriented in z -direction but has a y -component that depends on the k_x -momentum as well as the spatial coordinates y and z (see Fig. 4.30). At the edge and for central z -layers, the spin is mainly in z -direction with a pseudo spin in quantitative agreement with the 2D case. For larger y -values, a y -component emerges that is tilted from a negative to a positive component as one goes from one z -surface to the other. Along with this, the total z -spin is reduced and the z -pseudo spin changes to a positive value towards the z -surfaces. When k_x is changed, the overall picture remains the same with small changes of the absolute values. Edge states moving in the opposite direction at the same edge have a reversed spin at each lattice site. Even though the main direction of the pseudo spin is opposite compared to the 2D Bi_2Se_3 states, the notation of spin-up and spin-down states for the start and exit positions of the wave packets will be kept as in Fig. 4.7.

As can be seen in Fig. 4.29, the transition into the QAH phase now happens differently compared to the 2D model. In the 2D model, a small FEF splits the edge state bands of opposite pseudo spin but does not open a gap. Only if the FEF exceeds half the size of the bulk gap, a phase transition happens. Now, already an arbitrarily small FEF opens a gap in the dispersion of edge states with pseudo spin antiparallel to the field, while the other edge states remain basically unaffected. This is in better agreement with experimental realizations

of the QAH state where only small FEFs were achieved up to now [20, 56, 57]. When V_z exceeds the size of the hybridization gap, these states are removed from the gap, and the gap size increases with increasing field strength.

In the case of Bi_2Se_3 , another phase transition happens for high fields. For $V_z > |M_0|$ the bulk gap hosts again four non-degenerate edge state bands, however all with approximately the same spin. Whether this is a model artifact or a real effect cannot be said as FEFs induced in $(\text{Sb,Bi})_2\text{Te}_3$ up to now are way too small to reach this transition. In V doped $(\text{Sb,Bi})_2\text{Te}_3$, the achieved effective excitation gap in the edge state dispersion is only about $50\mu\text{eV}$, due to an overlap with the bulk valence band, while the real excitation gap may be 2-3 times as large [57]. In Fe doped Bi_2Se_3 , the induced gap in the surface state dispersion can reach up to 50meV [52].

Wave packets in 3D are constructed analogously to those in 2D with some changes regarding the involved momenta. Due to the small gap, the number of edge states in the gap as well as the spanned momentum range is very small. In order to achieve a sufficiently localized wave packet, the energy range of involved edge states is strongly extended beyond the hybridization gap. To increase the number of edge states per wave packet and to get a good overlap of consecutive edge states in the creation process, the eigenstates are calculated with a discretization of $\Delta k_x = \frac{4096}{2\pi}$. This is a fourth of the previous discretization. Due to the strong localization of the wave packet and periodic boundary conditions in x -direction, the actual system size of the simulated device can be chosen differently. Here, the device is composed of three parts, rowed along the x -direction. Incoming and outgoing wave packets are placed in the two outer parts with a length of $X = 384$ lattice sites, and the time-dependent overlap is only calculated within these parts. For a start, width and height are $Y = 256$ and $Z = 15$, respectively. The middle part is the scattering area and can have arbitrary dimensions. Its size is chosen to be $256 \times 256 \times 15$ with an FEF of size $128 \times 256 \times 15$ in the middle. The FEF has therefore the same length in x -direction as before. Only the width and height have been adjusted to the new device dimensions. The width of the Gaussian distribution Eq. (4.8) is chosen as $d = \frac{k_{\max} - k_{\min}}{5.5\sqrt{2}}$, where $k_{\max} - k_{\min} \approx 0.156$ defines the momentum range of the involved edge states. Since the transport calculations for 15 layers of Sb_2Te_3 without any further modifications show no significant deviations from the real 2D calculations, only a few examples are presented in the following to show minor differences.

Without FEF (Fig. 4.31), basically no scattering happens. Only near the Dirac point, which is located at about -0.13eV , a small fraction of the wave packet is constantly transferred to the opposite edge. As there is a constant flow towards the opposite edge, the dip in the transmission curve and the peak in the reflection curve become more pronounced when the device length is increased. When the device width is increased to $Y = 384$ lattice sites, the effect vanishes. The reason for this flow towards the opposite edge is that the real eigenstates of the device with a width of $Y = 256$ lattice sites slightly differ from those in the wave packet. Near the Dirac point, eigenstates from opposite edges hybridize due to an overlap in the finite system so that eigenstates located at one side have a small contribution from the opposite side. In the 2D simulations this effect was not present because the edge states were stronger localized at the edge due to the larger gap. Due to the smaller energy overlap at the gap edges compared to the 2D case, the Gibbs phenomenon cannot be entirely removed from the

4 Pure spin current devices and quantum transport calculations

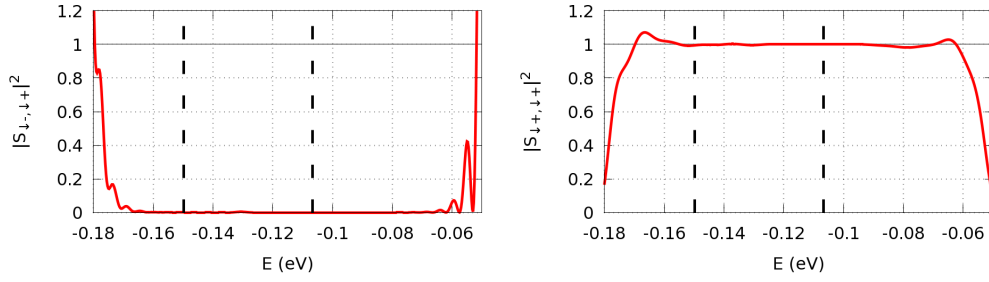


Figure 4.31: Scattering probability into spin-down states of the wave packet Ψ_{\downarrow}^+ in a 15 layer Sb_2Te_3 system without FEF. Black vertical lines indicate the hybridization gap. Due to the overall small energy range, the Gibbs phenomenon cannot be entirely removed from the hybridization gap at the lower end of the gap. Residual contributions to the backscattering channel Φ_{\downarrow}^- in the vicinity of the Dirac point, located at about -0.13eV , can be attributed to a hybridization of edge states from different edges.

hybridization gap at the lower end of the gap, and therefore, the transmission appears to be lower than one. Scattering into spin-up states does not happen and is therefore not shown in Fig. 4.31.

To get rid of the flow towards the opposite edge, the device width is increased to $Y = 384$ lattice sites for all device parts in all following simulations if not stated otherwise. The wave packets, however, can still be constructed from the edge states of the smaller lattice. When the edge states are linearly combined according to the overlap with previous edge states, the small effect of the hybridization at the Dirac point is automatically removed, i.e. the edge states are independent of the device width as long as the device is wide enough.

With an FEF in z -direction, the results of the real 2D devices are basically reproduced. In Fig. 4.29, it has been shown that the excitation gap in the edge state dispersion reaches the size of the hybridization gap for $V_z = 44\text{meV}$, so perfect reflection should be expected. However, from the scattering probabilities in Fig. 4.32a, it can be seen that a small fraction of the wave packet traverses the magnetic barrier in the vicinity of the Dirac point, located at about -0.13eV . Due to an overlap of edge states located at opposite sides of the barrier, electrons can tunnel through the barrier. This can be overcome by either increasing the width of the barrier or, like shown in Fig. 4.32b, by increasing the FEF. A larger FEF increases the gap size and thereby reduces the spatial extent of edge states at the edges of the magnetic barrier. Outside the hybridization gap, scattering into bulk states, or more precisely the hybridized surface states, results in a gradually decreasing reflection probability.

When the FEF is switched to $V_z = -66\text{meV}$, transmission through the magnetic barrier becomes almost perfect inside the hybridization gap and again drops gradually outside of the gap (see Fig. 4.33). Only at the lower end of the gap, the transmission probability drops slightly already inside the gap, hinting towards a reduced gap size at the TI-FTI interface. Simulations with $V_z = -44\text{meV}$ and $V_z = -100\text{meV}$ show the same scattering spectra inside the hybridization gap, so this effect seems to be independent of the field strength in this range.

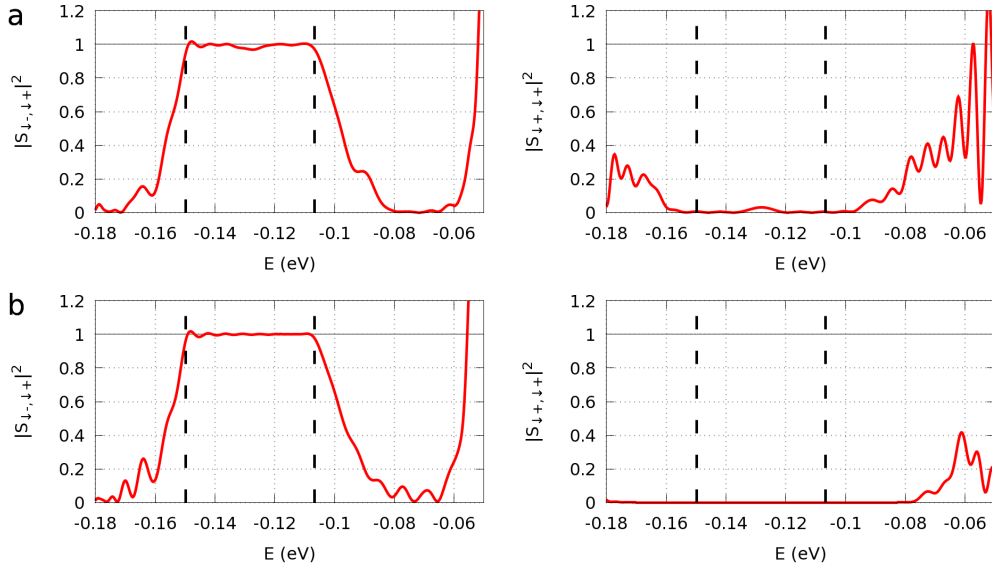


Figure 4.32: Scattering probabilities of the wave packet $\Psi_{\downarrow}^{\dagger}$ into spin-down exit channels for a positive z -polarized FEF in the middle of the device. **(a)** The FEF ($V_z = 44\text{meV}$) has about the same size as the hybridization gap. Near the Dirac point, a small fraction of the wave packet tunnels through the magnetic barrier, while the rest is reflected within the energy range of the hybridization gap. **(b)** When the FEF is increased to $V_z = 66\text{meV}$, the penetration length into the barrier is reduced and reflection becomes perfect.

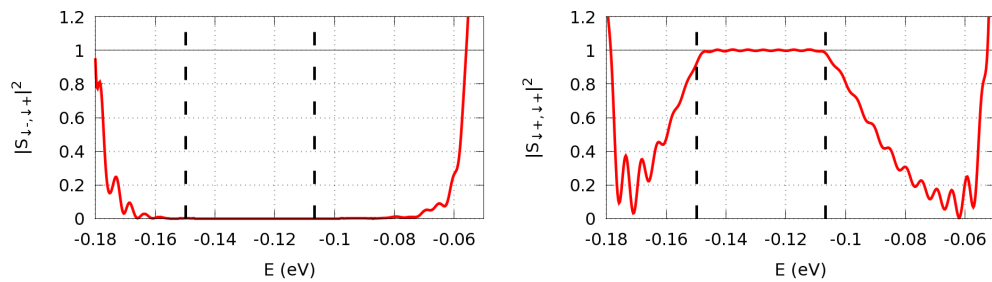


Figure 4.33: When the sign of the FEF is reversed ($V_z = -66\text{meV}$), the wave packet $\Psi_{\downarrow}^{\dagger}$ is perfectly transferred through the magnetic barrier for almost the full energy range of the hybridization gap.

4 Pure spin current devices and quantum transport calculations

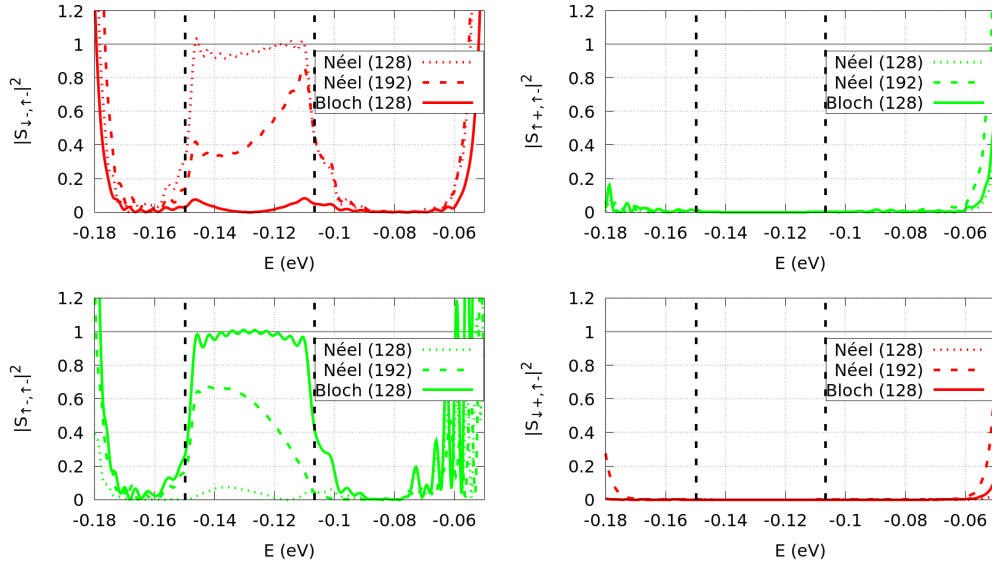


Figure 4.34: Scattering probabilities of the wave packet Ψ_{\uparrow}^{-} at domain walls of Néel and Bloch type with $\xi = 4$ (compare section 4.5.1). The two magnetic domains have field strengths of $V_z = \pm 66\text{meV}$. The scattering probabilities for Ψ_{\downarrow}^{-} are complementary, so the total transmission probabilities of both wave packets sum to one in both exit channels. Numbers in brackets specify the lengths of the domain walls.

In all cases, no scattering into spin-up states happens even though the two pseudo spin states are no longer strictly decoupled.

As already arbitrary small FEFs open a gap in the dispersion of one spin type, the FEF does not need to exceed the gap size to achieve this kind of switching behavior, like it was the case in the 2D calculations. However, for smaller fields, the reflection is restricted to the energy range of this excitation gap and a much wider barrier is needed to avoid tunneling because the localization of edge states at the TI-FTI interface becomes worse when the field is reduced.

For a domain wall, the results are also very similar to the 2D case (compare section 4.3.1 and 4.5.1). Without rotation via an in-plane component (not shown), the wave packets are perfectly transferred along the domain wall without spin-flip scattering for energies inside the gap. Outside the gap, the transmission probability drops rapidly. When the field is rotated via an x - or y - polarization from one z -polarization to the other (Fig. 4.34), the spin of the propagating wave packet can change along the domain wall. Still, the sum of both transmitted wave packets is one for both forward-moving exit channels and no scattering into back-moving channels happens. For the Néel wall, the energy dependence of the individual transmission probabilities changes when the length of the domain wall is changed. In the case of the Bloch wall, the scattering spectrum is independent of the domain wall length, and generally, only small fractions of the wave packets are transmitted into the exit channel with spin different from the initial spin. To achieve a sufficient spatial separation of exit wave packets and wave packets

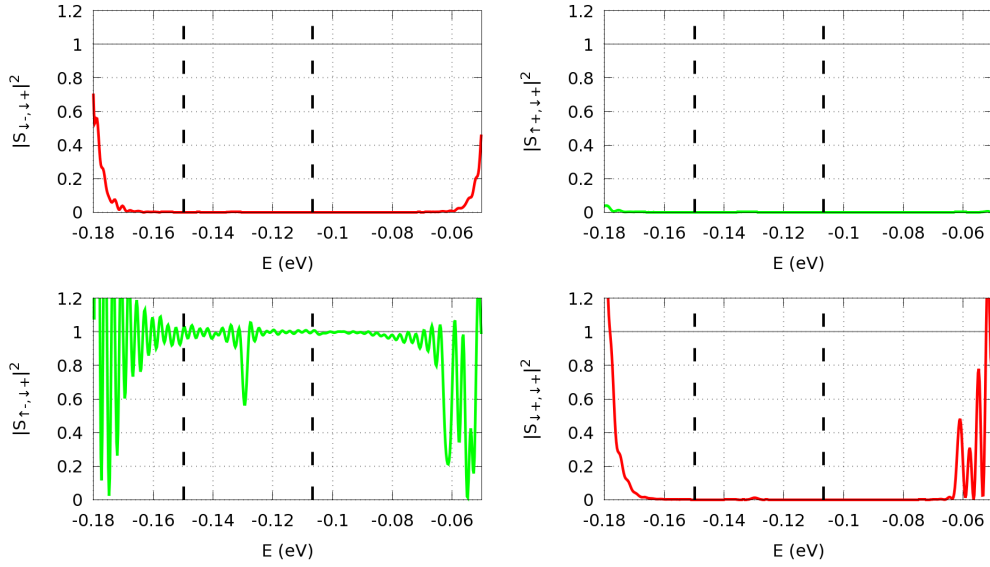


Figure 4.35: Scattering spectrum of the wave packet Ψ_{\downarrow}^+ encountering an FEF of strength $V_x = 66\text{meV}$ in x -direction. The wave packet is reflected with a spin-flip for almost the full energy range of the gap. A dip near the Dirac point, but at the same energy nearly no contributions in all other exit channels, indicates that part of the wave packet gets trapped in a flat band at the TI-FEI interface.

propagating along the FEFs, the length of the scattering area was increased to $X = 512$ lattice sites.

Major differences arise for the case of an in-plane FEF. In the 2D case, an in-plane FEF opened a gap in the edge state dispersion at the TI-vacuum interface and at the TI interface of a local FEF no edge states existed at all (Fig. 4.6). The scattering spectra, therefore, showed transmission for some energies and reflection with spin-flip for other energies (Fig. 4.15 and 4.17). Figure 4.35 shows the scattering spectrum for a device with 15 layers and $V_x = 66\text{meV}$. The wave packet is now perfectly reflected with a spin-flip for the whole energy range of the hybridization gap with only a narrow dip around the Dirac point. At the energy of the dip, only very small peaks show up for all other exit channels. So, the missing part of the wave packet has to be trapped somewhere in the device. A look at the time-resolved absolute value of the wave packet shows that, after the main part of the wave packet has been absorbed at the device ends, a small part still remains at the edge of the FEF at the position where it impacted. On long time scales, this part of the wave packet propagates very slowly along the TI interface of the FEF. At the same time, the wave packet becomes wider and diffusion between the two TI interfaces of the FEF happens. All of this hints towards the existence of slightly banded flat bands at the TI-FEF interfaces and a gap of at least the size of the hybridization gap at the vacuum interface.

When the FEF is further increased (Fig. 4.36a), the dip in the reflection spectrum becomes wider and the wave packet at the FEF edge moves faster, probably due to an increased

4 Pure spin current devices and quantum transport calculations

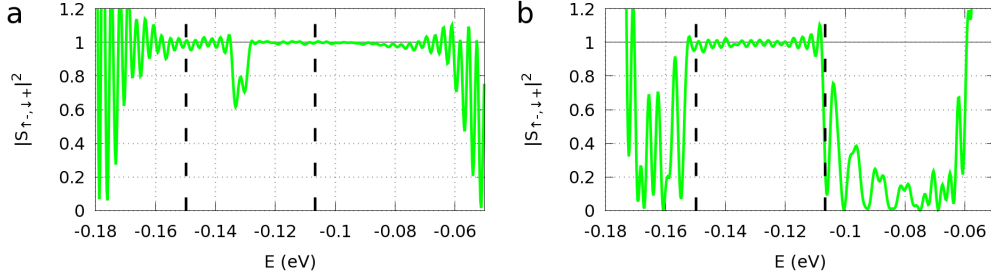


Figure 4.36: Reflection spectrum analogous to Fig. 4.35 for $V_x = 100\text{meV}$ (a) and $V_x = 22\text{meV}$ (b). For higher fields, the dip becomes wider, while it vanishes for small fields.

bending of the flat band. Besides, the stronger field results in a stronger focused wave packet at the edge of the FEF and a strongly reduced diffusion between the two edges. When the FEF is reduced, the dip gets narrower and eventually vanishes. For small fields like $V_x = 22\text{meV}$ (Fig. 4.36b), the wave packet is completely reflected for the whole energy range of the hybridization gap. To reduce tunneling through the FEF, especially for small fields, the lengths of the scattering area and the FEF have been increased to $X = 512$ and $X = 256$, respectively.

Simulations with FEFs in y -direction of various strength, ranging from $V_y = 22\text{meV}$ to $V_y = 100\text{meV}$, show only diffuse scattering into all exit channels for the whole hybridization gap. All simulations with an in-plane field are independent of the sign of the field and of the start wave packet in the sense that all wave packets are scattered in the same way.

4.5.3 Material imperfections

Despite all efforts to produce TIs as perfect as possible, any real device will always feature some imperfections. First, there may be impurities in the crystal, which result in spatially varying potentials. Secondly, in order to produce certain device structures, etching processes are required. These etching processes lead to rather random positions of edge atoms instead of clean edges [8].

Following Ref. [8], the electrostatic impurity potential at the lattice position $\mathbf{r} = (x, y, z)^T$ is modeled as

$$U_{\text{imp}}(\mathbf{r}) = \sum_n U_n e^{-\frac{|\mathbf{r}-\mathbf{r}_n|^2}{2\rho^2}}, \quad (4.26)$$

where the sum runs over all lattice positions \mathbf{r}_n so that the impurities are Gaussian correlated on the length scale ρ . The random potentials U_n are created Gaussian distributed as well, with a mean value U_0 defined by $\langle U_{\text{imp}}^2(\mathbf{r}) \rangle = U_0^2$. U_0 is adopted to be 2meV , while the correlation length is chosen to be 10 lattice sites. Note that by choosing a correlation length in terms of lattice sites, the actual correlation length in terms of meters is different for different spatial directions due to different lattice constants. To reduce the computational effort, the sum is

terminated at 3ρ in each spatial direction. With these parameters, the impurity potential has local maximal values of about $\pm 8\text{meV}$, i.e. about 20% of the hybridization gap.

Random edge positions are created by successively removing atoms from the lattice with a probability depending on the number of occupied neighbor lattice positions. The maximal deviation from the clean edge is given by the number of removing cycles, which is chosen to be 10.

The effect of these material imperfections is tested in multiple simulations for Sb_2Te_3 without FEF and with FEF of strength $V_z = \pm 66\text{meV}$ or $V_x = 66\text{meV}$. The dimensions of the scattering area and the FEF are again $256 \times 384 \times 15$ and $128 \times 384 \times 15$, respectively. As the effects are randomly generated, multiple calculational runs are performed for each configuration.

Random variations of the edge positions seem to have no impact on the scattering spectra, which is no big surprise since topological edge currents are supposed to be insensitive to the exact device geometry. A local potential, on the other hand, can locally change the energy of edge and bulk states so that edge states may be scattered into puddles of bulk states. Due to the smaller overlap with surrounding edge states, electrons will usually be scattered multiple times inside these puddles before they reenter the edge states. As these elastic scattering processes still conserve the spin, electrons leave the puddle with the same spin and propagation direction, though within the puddle, the spin states are mixed by spin-orbit coupling. Due to the finite dwell time inside these puddles, the scattering spectra are sometimes somewhat lower at the hybridization gap edges on an energy scale corresponding to the impurity potential extrema (see Fig. 4.37a). Outside the gap, where edge and bulk states coexist, a stronger effect of the potential is observed because edge states are no longer protected from elastic scattering processes. With z -field ($V_z = \pm 66\text{meV}$), the effect inside the gap is less pronounced. In the case of an x -field (Fig. 4.37b), the impurity potential has an impact on the dip in the reflection spectrum, originating from a flat band at the TI-FEF interface. Though the depth of the dip, i.e. the probability that an electron enters the flat band, is changed, it never completely vanishes, indicating a robustness of the flat band with respect to this kind of perturbation. However, it can have some impact on the propagation along the TI-FEF interface. In one calculational run, the wave packet remained more focused at the impact position and showed no collective motion along the interface.

Changing the correlation length does not change the qualitative effect of the impurity potential. A larger correlation length makes it only more likely that puddles get large enough to have an effect, i.e. a notable effect is observed more often.

Essert *et al.* [100] showed in transport calculations for HgTe/CdTe quantum wells that, when dephasing is included into the transport calculations, up to 50% of the wave packet is reflected with spin-flip by such a puddle. The reflection probability depends both on the dephasing time and the dwell time in the puddle.

4.5.4 Broken structural inversion symmetry

Up to now, it was assumed that the TI is surrounded by vacuum on all sides, which is an insulator with an infinite gap. In reality, however, the TI resides on a substrate, i.e. an insulator with a finite gap. This finite gap allows TI states to penetrate into the substrate and changes

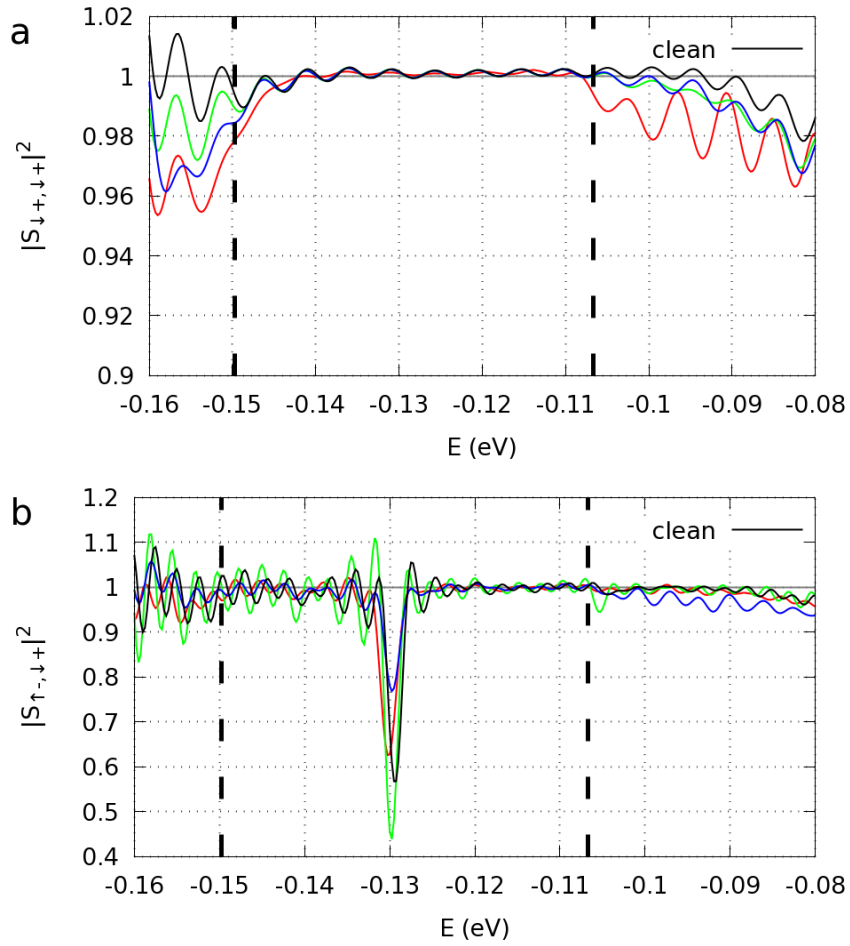


Figure 4.37: Transmission probability of the wave packet Ψ_{\downarrow}^{+} with impurity potential and random edge positions. Each of the three colored curves corresponds to a different random impurity potential, generated with the same parameter set. The black curve is a reference curve without impurities. **(a)** Without FEF after an evolution time of $\tau = 2000 \frac{1}{\text{eV}}$. **(b)** With FEF $V_x = 66 \text{meV}$ after an evolution time of $\tau = 3000 \frac{1}{\text{eV}}$. Note the changed axes scales.

the dispersion of states close to the interface. It has been shown by ARPES measurements that in thin films of Bi_2Se_3 , grown by molecular beam epitaxy, the hybridized surface states on the top surface show a Rashba-type spin-orbit splitting. This splitting is attributed to a potential gradient induced by structural symmetry breaking due to the SiC substrate [46]. With Rashba effect, spin-up and spin-down bands are relatively shifted by $\pm\alpha k_{\parallel}$, where α is the Rashba coupling parameter and k_{\parallel} the in-plane momentum. Split bands cross at $k_{\parallel} = 0$ [101]. For Sb_2Te_3 thin films, no Rashba splitting was observed, but only the lower part of the Dirac cone was measured [37].

Additionally, the TI may be capped by an insulating layer to prevent the surface from aging or because the FEF is introduced via the proximity effect. So, there might be insulating layers below and above the TI, potentially with different gap sizes. A Rashba spin splitting of conduction bands in 3D Bi_2Se_3 due to deposition of donor atoms or absorption of gas molecules on the surface has been observed with SARPES as well [101]. So, when the structural inversion symmetry of the TI is broken by an insulating layer below or on top of the TI, the band structure and, more importantly, the transport properties may be altered.

In the following, the effect of an insulating layer on one or both sides of the TI layer will be studied in transport calculations. The TI is again modeled as 15 layers of Sb_2Te_3 . Insulating layers are modeled using the same parameters except for the parameter M_0 . To make the material insulating, the sign of M_0 is reversed. Varying gap sizes, which are given by $2M_0$, can then be achieved by changing the value of M_0 for the insulating layer. The SiC substrate used in Ref. [46] has a gap of about 3eV [102], corresponding to $M_0 \approx 1.5\text{eV}$.

The left panel of Fig. 4.38 shows the 2D projection of the square of the absolute value of the propagating wave packet without insulator (left) and with insulator (right). Brighter colors represent higher values, where black is about zero and yellow the maximum. It can be seen from the side view that the wave packet penetrates into the insulating layer below the TI and from the top view that its spatial extend in the surface plane is reduced, indicating an increased gap size. This is confirmed by the dispersion shown in the right panel. Compared to the hybridization gap of the free standing TI, indicated by red lines, the gap has increased at the upper edge by about a factor of two from $\sim 43\text{meV}$ to $\sim 88\text{meV}$. Additionally, the conduction and valence bands, i.e. the hybridized surface states of top and bottom surface, show Rashba splitting. This was not observed in ARPES measurements on Sb_2Te_3 thin films [37]. However, only the lower part of the Dirac cone was observed in those measurements and the substrate was different from that in the Bi_2Se_3 measurements. Besides, the calculated splitting in the valence band is less pronounced than in the conduction band, especially compared to calculations for Bi_2Se_3 (see below). As the dispersion does not resolve the k_y momentum component, the Rashba coupling parameter α cannot easily be resolved. Anyways, a quantitative analysis of the Rashba effect is not meaningful due to the phenomenological modeling of the insulator. The spatial extend of the edge states as well as the gap size depend on the size of insulator gap. A smaller insulator gap results in a larger hybridization gap and stronger localized edge states.

For Bi_2Se_3 , the effect of the insulator is different in the sense that the gap size remains basically the same with only a small energy shift (see Fig. 4.39). Furthermore, significant Rashba splitting can now not only be observed for the bulk states but also for edge states

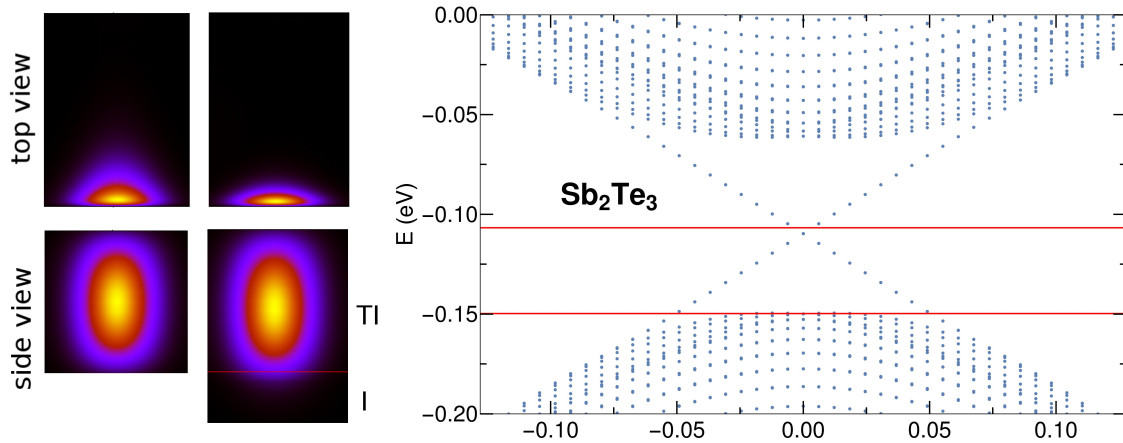


Figure 4.38: Comparison of free standing Sb_2Te_3 and Sb_2Te_3 on an insulator with 3eV gap. The left panel shows the 2D projection of the square of the absolute value of the wave packet without insulator (left) and with insulator (right). Brighter color means a higher value, i.e. black color corresponds to about zero and yellow is the maximum. The shown width (x -direction) is about 200 lattice sites, the depth (y -direction) in the top view 256 lattice sites and the height (z -direction) of TI and insulator (I) in the side view 15 and 5 lattice sites, respectively. The right panel shows the corresponding dispersion of 15 layers Sb_2Te_3 on 5 layers insulator with 3eV gap. Red lines indicate the gap of the free standing Sb_2Te_3 (compare Fig. 4.29). For details see main text.

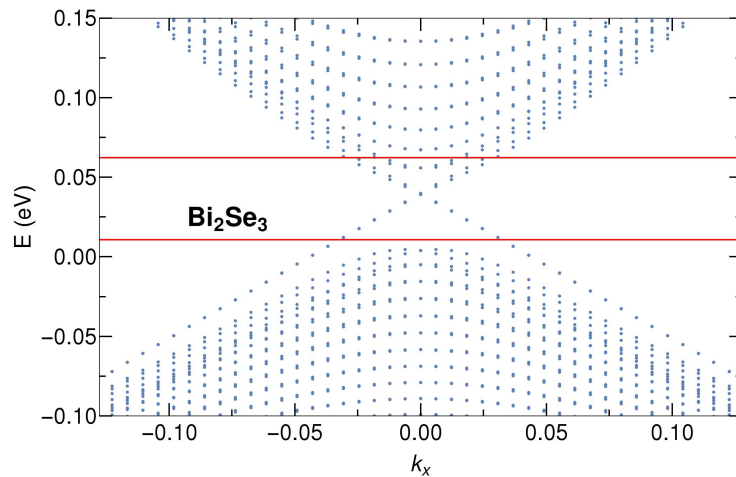


Figure 4.39: Dispersion of 15 layers Bi_2Se_3 on 5 layers insulator with a gap of 3eV. Red lines mark the hybridization gap of the free standing TI. Unlike in Sb_2Te_3 , the gap has about the same size as before. Besides the Rashba splitting of the hybridized surface states that was present for Sb_2Te_3 , there is now significant splitting of the edge states above the Dirac point as well.

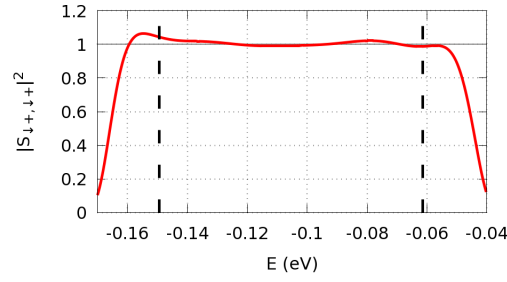


Figure 4.40: Scattering probability of $\Psi_{\downarrow}^{\uparrow}$ into $\Phi_{\downarrow}^{\uparrow}$ without barrier. Even though transmission is perfect, i.e. no scattering happens, the probability could not be tuned to one for the whole gap.

above the Dirac point. Here it is important to note that the insulating layers for Sb_2Te_3 and Bi_2Se_3 are not the same except for the gap size. All other model parameters are chosen equivalent to those of the TI. It may therefore be that the hybridization gap of Bi_2Se_3 increases as well when the material parameters of Sb_2Te_3 are used for the insulator. So, to get a more quantitative picture of the effect of the substrate, real model parameters for the insulating layer as well as its coupling to the TI are needed. It can, however, be summarized that an insulating layer most likely induces Rashba splitting and may affect the hybridization gap. Therefore, the effect of the insulating layer on the transport properties of Sb_2Te_3 is examined in the following.

For that purpose, new edge states are generated and an insulating layer is added below the whole device structure. Due to the broken inversion symmetry, neither the twofold rotation operator along the x -direction nor the inversion operator can be used to reduce the dimension of the eigenvalue problem. However, the system still has twofold rotation symmetry along the z -direction so that only edge states for $k_x \leq 0$ have to be calculated. Since the increased gap size involves much better localized edge states, a device width of $Y = 256$ is sufficient. The width of the wave packet was chosen as $d = \frac{k_{\max} - k_{\min}}{5\sqrt{2}}$, where $k_{\max} - k_{\min} \approx 0.166$. Depending on the length of the FEFs, the length of the scattering area is either $X = 256$, for an FEF with length $X = 128$, or $X = 512$, for longer FEFs.

Even though the conditions seem to be better with the increased gap size, it was not possible to tune the wave packet so that the scattering spectrum is normalized to one. Already the scattering spectrum without barrier (Fig. 4.40) shows variations from unity of the order of 5% for the whole gap so that an error of this magnitude has to be considered in all following results. Scattering into other exit channels is not present without barrier even if material imperfections are added.

The perfect transmission or reflection behavior changes when an FEF is introduced. Figure 4.41 shows the scattering spectrum of the wave packet $\Psi_{\downarrow}^{\uparrow}$ for an FEF of strength $V_z = 90\text{meV}$ (about the size of the gap) spanning the whole width of the TI strip. The barrier has a length of $X = 128$ and is only added to the top 15 layers, i.e. only to the TI. It can be seen that the broken structural inversion symmetry, due to the insulating layer below the TI, destroys the perfect reflection behavior. About 10% of the wave packet is scattered into the spin-up exit channels with about 5% per channel. Only the other spin-down channel has

4 Pure spin current devices and quantum transport calculations

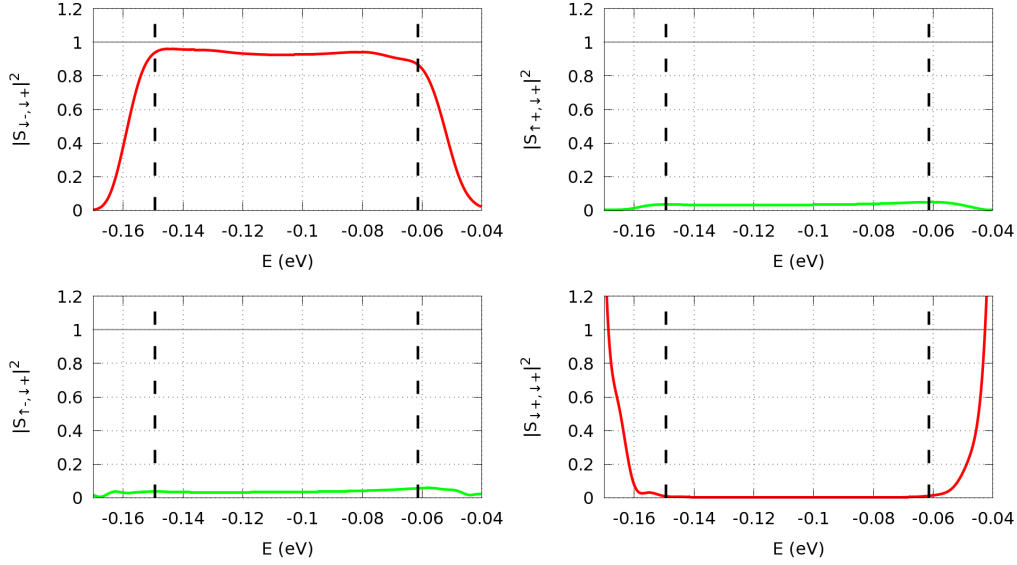


Figure 4.41: Scattering spectrum of the wave packet Ψ_{\downarrow}^+ for an FEF of strength $V_z = 90\text{meV}$ spanning the full width of the TI strip. About 10% of the wave packet is scattered into spin-up exit channels with about 5% per channel. There is basically no scattering into the Φ_{\downarrow}^+ exit channel.

basically no contributions. From the time-resolved absolute value of the wave packet, it can be seen that these scattering processes happen at the points where the wave packet encounters and leaves the FEF. Simulations with a negative FEF ($V_z = -90\text{meV}$) or with other start wave packets show qualitatively the same scattering spectrum with about 10% loss into exit channels of opposite spin. Again, impurity potential and random edge positions show no significant effect.

Simulations so far showed that the broken structural inversion symmetry induces spin-flip scattering only in the presence of an FEF. Scattering thereby only happens at the points where the wave packet enters or leaves the barrier because spin-up and spin-down states coexist only in these points at the barrier. In a device where two FEFs of opposite polarity are in contact, however, spin-up and spin-down states coexist along the whole domain wall. Figure 4.42 shows scattering spectra of simulations for a domain wall of length $X = 128$ and FEFs of strength $V_z = \pm 90\text{meV}$ for the top and bottom half of the barrier, similar to previous domain wall simulations. A Bloch or Néel wall like rotation of the field at the domain wall is not considered here. It can be seen that about 5% of each wave packet end up in each of the two reflective exit channels, i.e. only about 90% are effectively transmitted. This increases the resistance of the transistor device but does not destroy a pure spin current because the sum of both wave packets is equal in the spin-up and spin-down channel. In the transmitting channels, the sum of both wave packets is equal as well. However, the incoming spin-up wave packet is mainly transferred into the spin-down channel and vice versa, indicating that the spin of the wave packet changes continuously along the domain wall. Simulations with

4.5 Towards more realistic modeling

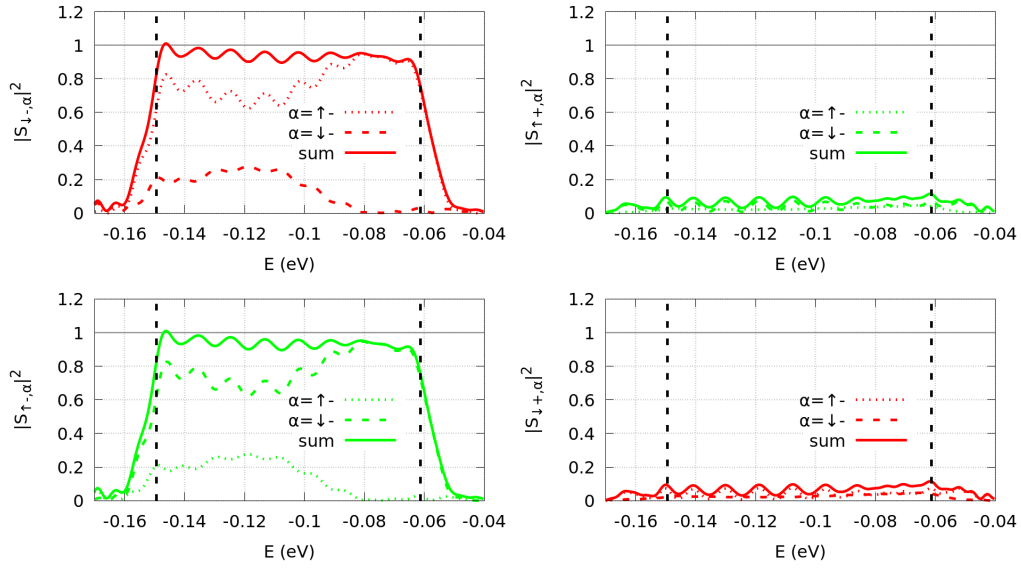


Figure 4.42: Scattering spectra of the wave packets Ψ_{\downarrow}^- and Ψ_{\uparrow}^- at a domain wall of length $X = 128$ with FEFs of strength $V_z = \pm 90 \text{ meV}$. In total, about 10% of each wave packet is reflected by the domain wall, and the transmitted parts of the wave packets largely change their spin. The total transmission and reflection probabilities, i.e. the sum of both wave packets, is the same for spin-up and spin-down exit channels.

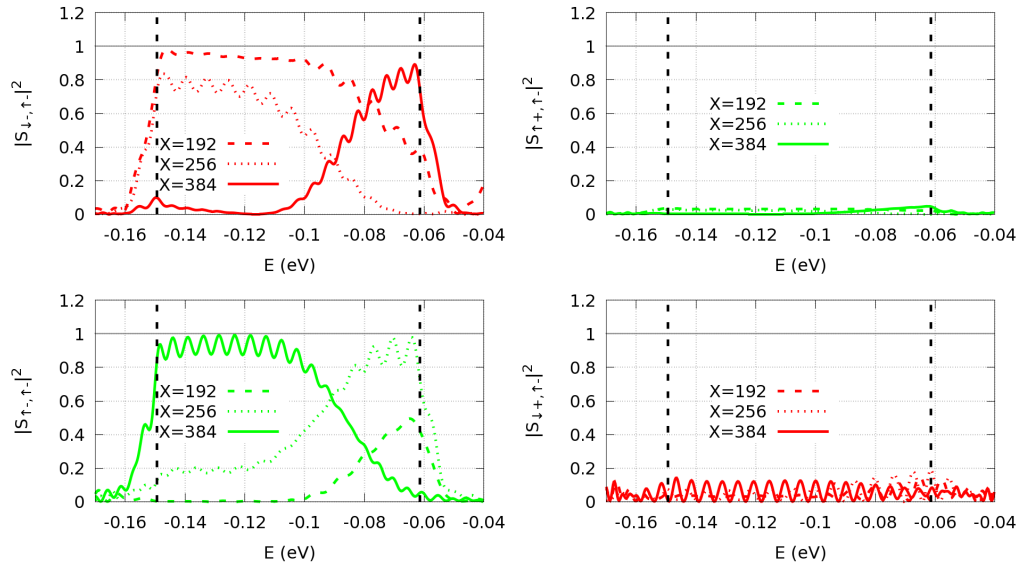


Figure 4.43: Scattering spectra of the wave packet Ψ_{\downarrow}^- at domain walls of various length X with FEFs of strength $V_z = \pm 90 \text{ meV}$. The spin of transmitted electrons depends on the length of the domain wall as well as the electron energy.

4 Pure spin current devices and quantum transport calculations

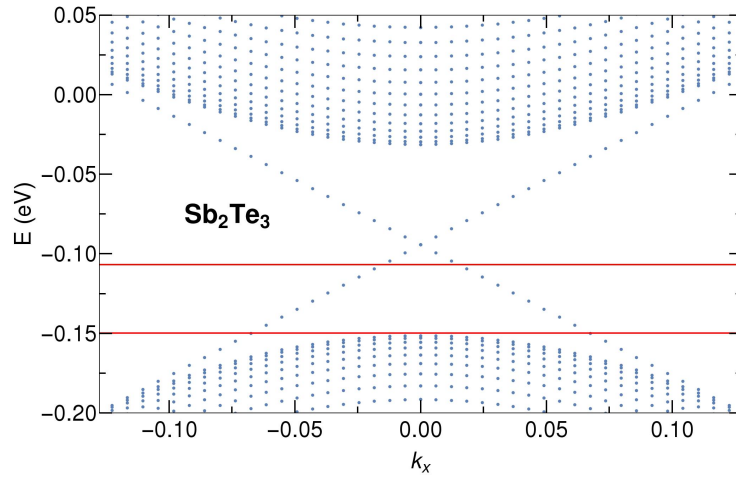


Figure 4.44: Dispersion of 15 layers Sb_2Te_3 sandwiched by 5 layers of an insulator with 3eV gap. Red lines indicate the gap of the freestanding TI. Compared to the case with an insulator only below the TI, the gap has increased to about 120meV. Rashba splitting is no longer present.

different domain wall lengths support this assumption (see Fig. 4.43). When the length of the domain wall is changed, the distribution over the two transmitting channels changes, while the total transmission probability remains about constant. The probability that an electron changes its spin along the domain wall thereby depends on the length of domain wall as well as the electron energy.

If an insulating layer with the same material parameters is added below and above the TI sheet, the structural inversion symmetry is restored. As a consequence, no significant changes of the scattering spectra with respect to the free standing TI appear. Capping the TI with the same material used for the substrate may therefore be reasonable, also with regard to the potentially increased hybridization gap. The dispersion of Sb_2Te_3 with 5 layers of an insulator with a gap of 3eV below and above the TI is shown in Fig. 4.44. Rashba splitting can no longer be observed, and the gap size has increased even further to about 120meV. Since the hybridization gap tends to increase in the presence of an insulator, quantum well structures of Sb_2Te_3 and a similar but topologically trivial material, e.g. Sb_2Se_3 , may be interesting. In addition to the potentially increased gap size, the TI would be decoupled from the substrate, and by this, potential gradients as well as lattice mismatches should be reduced. For Sb_2Te_3 sandwiched by an insulator with the same parameters but reversed sign of M_0 , the hybridization gap has a size of about 117meV. The tendency that a smaller insulator gap results in a wider hybridization gap therefore does not generally extend to the case with two insulating layers.

Even though the broken structural inversion symmetry induces spin-flip scattering, this should have no big effect on the functioning of the proposed spintronic devices. As the scattering processes are the same for spin-up and spin-down electrons, the loss in spin-up electrons should in most cases compensate that in spin-down electrons and vice versa. Deviations from

the perfect behavior can only arise, when the number of scattering sites is different for spin-up and spin-down channels. This is, however, only the case for the transistor in the “off”-state, where the different spin channels are blocked by two consecutive magnetic barriers. As the blocking is no longer perfect, the device can have residual charge currents along the right edge, where no current should flow at all.

4.5.5 Inhomogeneous exchange field

FEFs are induced in TIs either by doping with transition metal atoms [19, 56, 57] or by a ferromagnetic insulator via the proximity effect [60, 61]. Here, however, the FEF was considered homogeneous within the magnetic domains. So, the question is how inhomogeneous FEFs change the device properties or rather under what conditions they reproduce the desired properties. While the homogeneous field should be a valid approximation for the doping case, it clearly does not well represent the proximity induced field, which has a finite penetration depth d_p and may break structural inversion symmetry. Assuming a strictly exponentially decaying field strength, the proximity field at a distance d to the surface of the TI is given by

$$V_p = V_0 e^{-\frac{d}{d_p}}, \quad (4.27)$$

where V_0 is the field maximum at the surface layer. For EuS the penetration depth is about 1nm-2nm [61, 62], i.e. about 5-10 mono-layers. Here, $d_p = 5$ will be used, however with significantly increased field strength compared to EuS. The scattering area has an increased size of $512 \times 384 \times 15$ with an FEF of size $256 \times 384 \times 15$ in the middle to reduce tunneling processes through the magnetic barrier that can be attributed to weakly localized edge states at the TI-FEF interface. Insulating layers, representing the ferromagnetic insulator or the substrate, are not included in this section because the material parameters, which are necessary to produce quantitatively representative results, are lacking.

The scattering spectrum of the wave packet Ψ_{\downarrow}^+ , when a z -polarized proximity field is applied only from the top, is shown in Fig. 4.45 for $V_z > 0$ and in Fig. 4.46 for $V_z < 0$. Starting with the positive field, the first thing to mention is that, for the field strength used for the homogeneous field ($V_z = 66\text{meV}$), a huge part of the wave packet passes the magnetic barrier. Two narrow peaks with about 100% transmission appear near the gap edges and a broader, smaller one around the Dirac point. The field is now too weak to completely remove the edge states from the gap, therefore the two narrow peaks. As a smaller field results in a weaker localization of the edge states at the TI-FEF interface, the wave packet can tunnel through the barrier for energies around the Dirac point. By increasing the width of the barrier, the broader peak may therefore be removable. When the field strength is increased by about a factor of two, both effects vanish. Besides these spin conserving effects, in both cases also scattering into exit channels with opposite spin is present. For the higher field strength, about 10%-20% of the wave packet is scattered into these exit channels, depending on the position inside the gap. Again, the effect is bigger for smaller fields. For the negative field, the scattering probabilities into exit channels with opposite spin are the same as for the positive field. Reflection without spin-flip is nearly absent, already for the smaller field strength.

4 Pure spin current devices and quantum transport calculations

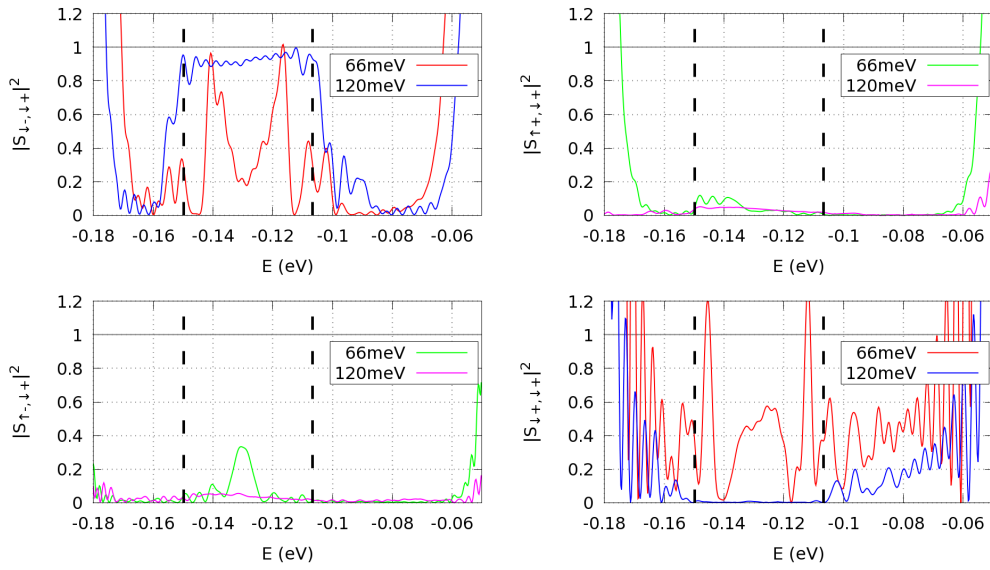


Figure 4.45: Scattering spectrum of the wave packet Ψ_{\downarrow}^+ at a positive z -polarized proximity field of varying strength decaying only from the top layer. For small fields, a huge part of the wave packet traverses the magnetic barrier into the Φ_{\downarrow}^+ exit channel and the spin-up exit channels have significant contributions, too, especially near the Dirac point. A better result is achieved with an about two times higher field. Then, there is nearly no tunneling into the Φ_{\downarrow}^+ exit channel. Still, about 10%-20% of the wave packet is scattered about equally into both spin-up exit channels.

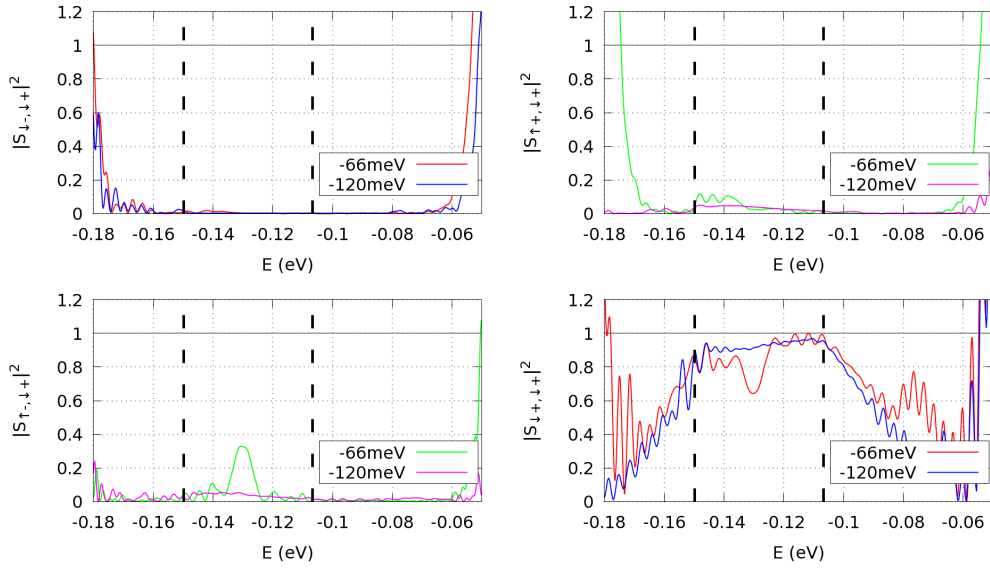


Figure 4.46: Scattering spectrum of the wave packet Ψ_{\downarrow}^+ at a negative z -polarized proximity field of varying strength decaying only from the top layer. The scattering probabilities into spin-up exit channels are basically the same as for the positive field. Contributions to the Φ_{\downarrow}^- channel are insignificant.

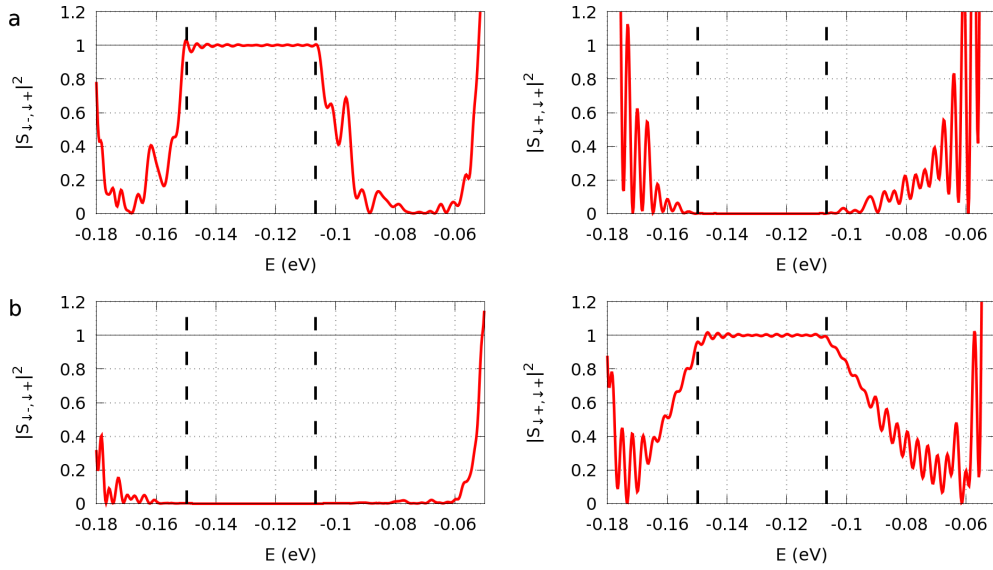


Figure 4.47: Scattering probabilities of the wave packet Ψ_{\downarrow}^+ into spin-down exit channels for proximity fields of the same sign decaying from the top and the bottom. (a) $V_z = 66\text{meV}$ and (b) $V_z = -66\text{meV}$. This configuration reproduces the mean field result already for the same small field strength, provided the barrier is wide enough.

4 Pure spin current devices and quantum transport calculations

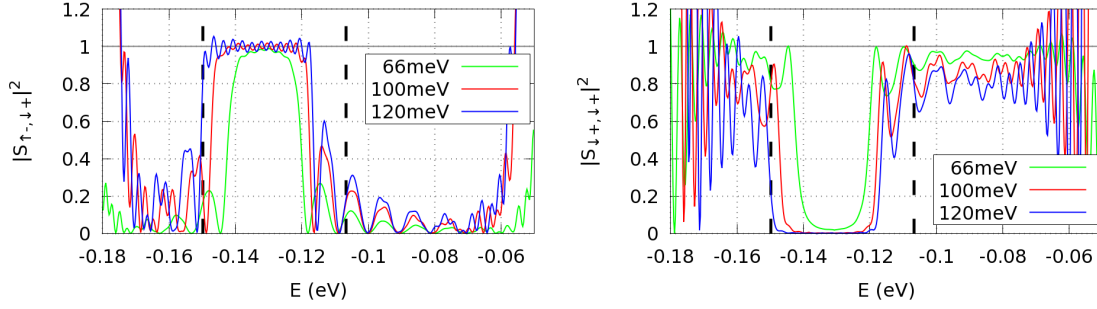


Figure 4.48: Reflection (with spin-flip) and transmission probability of the wave packet Ψ_{\downarrow}^+ for proximity fields of opposite z -polarization from the top and the bottom. For a broad energy range, the wave packet is almost completely reflected by the barrier with a change of its spin. No scattering into the other exit channels happens. The spectrum is similar to that of a small homogeneous x -field.

Spin-flip scattering is an effect of the broken structural inversion symmetry, and can therefore be removed by simultaneously adding proximity fields from the top and the bottom. It is, however, questionable whether or not a TI can be grown directly on top of a ferromagnetic insulator. Fields added from the top and the bottom result in a field that is overall stronger, and for a sufficiently wide barrier, the switching properties of the homogeneous field are already achieved at $V_z = \pm 66 \text{ meV}$ (see Fig. 4.47). In the middle of the TI layer, the field in this case has a minimal value of only about 26.7 meV . This value is much smaller than the minimal homogeneous field strength of 44 meV that is required to remove all edge states from the hybridization gap (compare Fig. 4.29).

Another interesting observation is that, by adding proximity fields of opposite z -polarization from the top and the bottom, a reflective behavior similar to a homogeneous x -field can be achieved (see Fig. 4.48). It is thereby unimportant which proximity field has which orientation. So, if it is possible to create such a device structure, it would be very useful for TI based spintronic devices. If one of the ferromagnetic insulators has a higher coercive field, e.g. by antiferromagnetic pinning, the device structure with two proximity fields can be switched between three different states (both fields up/down/different) by applying magnetic fields of varying direction and strength. The same reflective behavior can be achieved with fields that are homogeneous in the top and bottom half of the TI layer.

When the magnetic moments of the donor atoms or the ferromagnetic insulator are aligned by an external magnetic field, a misalignment of device and external field may result in small deviations of the resulting FEF from the desired orientation. As this can add an in-plane component to an otherwise out-of-plane field, the switching properties of devices based on the QAH effect may be altered. Besides, the in-plane anisotropy of ferromagnetic insulators like EuS results in an in-plane component inside the TI as well (see discussion in section 2.2). Calculations with a tilt of up to 20° away from a perfect z -orientation show that the effect is rather small. In the case of a tilt into x -direction about 5%-20% of a wave packet is transferred into exit channels with opposite spin (see Fig. 4.49). Nearly nothing is transferred into the

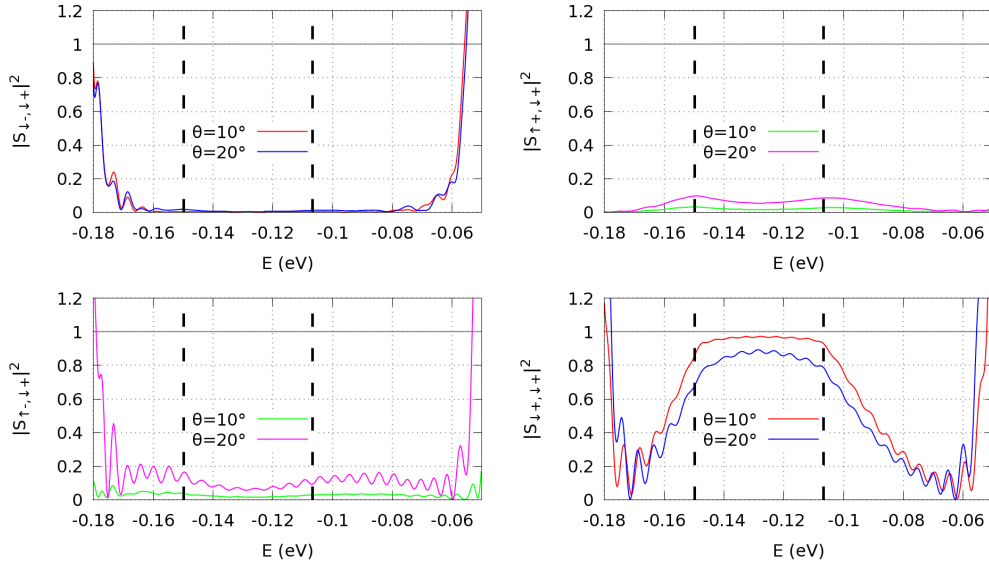


Figure 4.49: Scattering spectrum of the wave packet Ψ_{\downarrow}^+ encountering an FEF of strength $V_z = -66\text{meV}$ that is tilted by θ degrees into x -direction. Only a relatively small fraction of about 5 – 20% of the wave packet is scattered into exit channels with opposite spin orientation.

other exit channel with the same spin. For a tilt into y -direction, the effect is much smaller with less than 5% off-scattering at a 20° tilt. Changes of the scattering rates are approximately the same for positive and negative z -fields. Random impurity potentials and rough edges show no big influence on the scattering spectra.

4.6 Summary

By numerical time-evolution of wave packets in 2D TIs with local FEFs, it has been shown that these structures can be used to steer spin polarized edge currents. In the absence of in-plane fields, the edge state pseudo spin is conserved and a 100% steering efficiency can be obtained. Using only out-of-plane fields, which are naturally stable in the Bi_2Se_3 class of TIs, devices were conceived, which are capable of creating, switching and detecting pure spin currents with high efficiency. Because charge currents are directly converted into spin currents, these devices can be more efficient than other state of the art concepts. The large bulk gap of the 2D TI model promises even operation at room-temperature, provided that the induced FEFs are just as strong. As the size of device structures is only dictated by the spatial extent of edge states, they can be reduced to a very small scale in large gap TIs.

More realistic calculations were performed using thin films of 3D TIs. These calculations showed smaller bulk gaps but a QAH effect already for arbitrary small FEFs, in consistence with experimental observations. Even though some realistic effects can change the spin of

4 Pure spin current devices and quantum transport calculations

propagating electrons, the pure spin current devices were shown to be very stable because scattering events in different electron channels largely compensate each other. Sizable deviations of 10%-20% arise only due to a breaking of structural inversion symmetry or a global in-plane field component. These effects may, however, be avoidable by careful device engineering. If they are present, they can cause a small residual charge current at the right side of the spin current transistor in the “off”-state because the number of scattering sites for spin-up and spin-down current is unequal in that case.

Due to the rather small size of the hybridization gaps and currently achievable magnetic excitation energies, measurements of the proposed devices will require relatively low temperatures. To achieve room temperature applicability, other materials with larger 2D gaps have to be considered and the excitation gaps have to be enhanced.

5 Meservey Tedrow method

Due to their intrinsic locking of momentum and spin, TIs make interesting candidates for spintronic applications. In many cases, e.g. when combined with ferromagnets [2, 64, 65] or in the spin current devices discussed in the previous chapter, the efficiency of TI based devices strongly depends on the surface state spin polarization. Thus, to give a quantitative measure of the efficiency of TI based spintronic devices, it is crucial to get a precise picture of the surface state spin texture of TI materials. Currently the most prominent method for measuring the surface state spin is spin- and angle-resolved photoemission spectroscopy ((S)ARPES). In ARPES measurements, photoelectrons emitted by a crystal due to irradiation with a strong monochrome light source, e.g. a laser, are analyzed in terms of their energy and emission angle, which are in direct connection to the vacuum momentum. By applying energy and momentum conservation laws, the dispersion of the initial electrons in the crystal can be determined from this information [103]. SARPES additionally determines the spin of photoelectrons, which is assumed to be conserved in the photoemission process [104].

For 3D TIs of the Bi_2Se_3 class, it was theoretically predicted that the spin lies mainly in the surface plane and is orthogonal to the momentum. Due to a hexagonal deformation of the Fermi surface, some of these materials also feature a small out-of-plane polarization, which increases with momentum. SARPES measurements confirm these predictions. However, where theoretical calculations predict in-plane spin polarizations of about 50%-65% [42, 87, 88], values reported by SARPES measurements show no uniform result but vary between about 45% and up to 100% [38, 39, 42, 43]. The reason for this discrepancy is that the spin polarization of emitted photoelectrons in SARPES measurements can be manipulated by the photon energy and the geometry of the setup. Hence, it can deviate from the spin of the original electrons in topological surface states, i.e. for TIs, the spin is not necessarily conserved in the photoemission process [39, 42, 104, 105]. An alternative approach for measuring the spin polarization would therefore be useful to verify SARPES measurements and theoretical predictions. This alternative could be based on spin polarized tunneling. Liu *et al.* [24] investigated topological surface states in a spin Hall effect like fashion, using spin polarized electrons tunneling from a ferromagnet. However, they did not determine the surface state spin polarization, only the charge spin conversion efficiency. A closer look at such a device is taken in chapter 6. Here, another method, developed by Meservey and Tedrow [21, 22], based on quantum tunneling from a thin superconducting film, will be investigated regarding its applicability to TIs.

It was shown by Meservey, Tedrow and Fulde [106] that a strong parallel magnetic field splits the quasiparticle states of spin-up and spin-down electrons in thin (approximately 50\AA) superconducting aluminum (Al) films. In a magnetic field of strength B , the BCS energy spectra of opposite spin are shifted by $\pm\mu_B B$ with respect to the spectrum without magnetic field. So, the total spectrum, i.e. the sum of both, shows four peaks (see Fig. 5.1). μ_B is the

5 Meservey Tedrow method

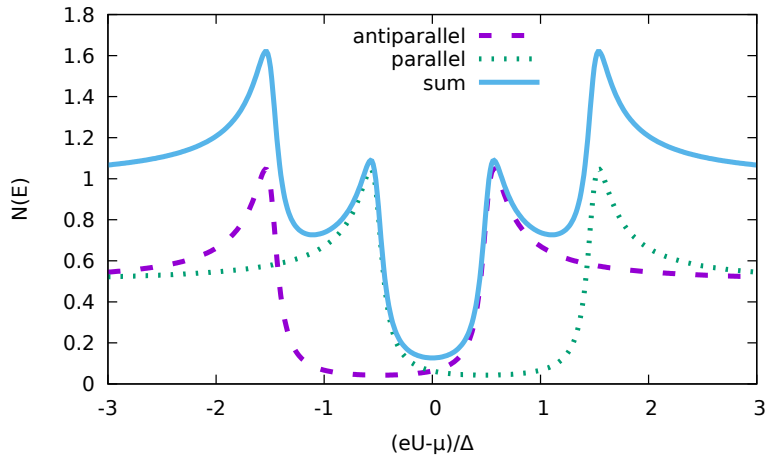


Figure 5.1: In a strong parallel magnetic field, the BCS density of states of a thin layer of superconducting aluminum splits. Electron states are shifted either in positive or negative direction with respect to the chemical potential μ , depending on whether their spin is parallel or antiparallel to the applied field. The sum of both spectra features four peaks whose relative height can be used to measure spin polarizations in tunneling experiments.

Bohr magneton. As the spin of electrons tunneling from this superconducting layer, through an insulating layer (I), into the surface of a third material is conserved in the tunneling process [21], such a device structure can be used to measure the polarization of this material.

If the material is ferromagnetic, electron spins in the ferromagnet and the superconducting aluminum film are aligned either parallel or antiparallel because of the strong magnetic field. So, when the conductance of this tunnel junction is measured, the polarization of the ferromagnet can be calculated from how the different densities of states of spin-up and spin-down electrons in the ferromagnet change the relative height of the four peaks in the split BCS spectrum. When the ferromagnet is unpolarized, i.e. a normal metal, the conductance of the junction simply reproduces the split BCS spectrum shown in Fig. 5.1 because the densities of states of spin-up and spin-down electrons are equal at the Fermi level. Different densities of state of spin-up and spin-down states result in an asymmetric tunnel spectrum, where the BCS density of states of spin-up states is reduced and that of spin-down states increased or vice versa, depending on the sign of the polarization. Consequently, the spectrum of a fully polarized ferromagnet, which has only states of one spin type at the Fermi level, would show only one of the two shifted spectra.

In a TI, the spin of surface electrons does not align with the magnetic field. Instead, it rotates with momentum around the Fermi surface so that all spin orientations are equally populated. So, when the above scheme would be applied to a TI, the measured polarization would always be zero. In fact, the TI in total is unpolarized in the absence of an electric field. The solution to this issue is to make use of the fact that electrons with opposite spin move in opposite directions. When only electrons moving, e.g., in positive x -direction are measured,

the resulting tunneling spectrum contains information about the surface state spin, which can then be extracted by involving the geometry of the device. The device geometry, in that case, can be expressed by a simple geometrical factor that can also contain effects like spin-flip scattering.

In section 5.1, the process of extracting the surface state spin polarization from a tunnel spectrum is derived, with a subsequent numerical test. Instead of measuring the spin polarization for a given geometry, one can also measure the geometrical factor for a given polarization and extract the spin-flip mean free path, i.e. the length after which an electron loses all information on its original spin. This is done in section 5.2. Part of the concepts used in this chapter have already been published in Ref. [2] but in a different context.

5.1 Derivation

In this section, a method for extracting the spin polarization of topological surface states from the tunneling spectrum of an AI/TI junction is derived. The basis for this is the model Hamiltonian for a hexagonal lattice Eq. (3.20), which provides a more realistic description of the surface state spin texture than the tetragonal lattice. For simplicity, the aluminum film is described using the same Hamiltonian with different parameters. In principle, a magnetic field has an effect on the topological surface states as well. However, while a magnetic field orthogonal to the surface would result in a Landau quantization [44], a parallel field only causes a shift of the Dirac cone in momentum space [107]. The effect of the magnetic field on the surface states is therefore neglected in the following.

Given an initial state $|m\rangle$ and a final state $|n\rangle$ with energies E_m and E_n , the transition rate through an insulating barrier can be calculated by Fermi's golden rule [83]

$$\Gamma_{mn} = \frac{2\pi}{\hbar} \delta(E_n - E_m) |\langle n | H_T | m \rangle|^2, \quad (5.1)$$

provided that the states are only weakly coupled. Fermi's golden rule is obtained by first order time-dependent perturbation theory, where the two states are considered unperturbed for times $t < 0$ and a constant perturbation exists for $t \geq 0$. In tight-binding approximation with nearest neighbor coupling, the transition Hamiltonian [2, 108]

$$H_T = -C_B \sum_{k_x, k_y, \alpha, \sigma} d_{k_x k_y \alpha \sigma}^\dagger c_{k_x k_y \alpha \sigma} + \text{h.c.} \quad (5.2)$$

ouples the last lattice site of the state $|m\rangle$ to the first lattice site of the state $|n\rangle$, leaving spin, orbital and in-plane momentum unchanged. $d_{k_x k_y \alpha \sigma}^\dagger$ creates an electron with in-plane momenta k_x and k_y and spin σ in orbital α of the first lattice site of $|n\rangle$. $c_{k_x k_y \alpha \sigma}$ destroys an electron with the same properties at the last lattice site of $|m\rangle$. The transition matrix element C_B depends on the properties of the insulating layer. However, as it cancels in the final results, the value is somewhat arbitrary. For simplicity, it is chosen to be $C_B = 1\text{eV}$ in numerical calculations. So, if ψ represents the last lattice site of $|m\rangle$ and ϕ the first lattice site of $|n\rangle$, the matrix elements can be calculated as $\langle \psi | H_T | \phi \rangle = -C_B \psi^\dagger \phi$, with the additional condition

5 Meservey Tedrow method

that the in-plane momenta are conserved.

At finite temperature, the probability for an eigenstate with energy E to be occupied is given by the Fermi function

$$f(E) = \frac{1}{1 + e^{\frac{E}{k_B T}}}. \quad (5.3)$$

When a voltage U is applied to the tunnel junction, initial and final states are occupied with probabilities $f(E_m - eU)$ and $f(E_n)$, respectively. So, the tunneling current from the aluminum film into the TI is given by

$$I_{m \rightarrow n}(U) = e \sum_{m,n} f(E_m - eU) [1 - f(E_n)] \Gamma_{mn} \quad (5.4)$$

and in the reverse direction by

$$I_{n \rightarrow m}(U) = e \sum_{m,n} f(E_n) [1 - f(E_m - eU)] \Gamma_{mn}. \quad (5.5)$$

This leads to a net current flow [2]

$$I(U) = I_{m \rightarrow n}(U) - I_{n \rightarrow m}(U) \quad (5.6)$$

$$= e \sum_{m,n} [f(E_m - eU) - f(E_n)] \Gamma_{mn} \quad (5.7)$$

$$= \frac{2\pi e}{\hbar} \sum_{m,n} [f(E_m - eU) - f(E_n)] |\langle n | H_T | m \rangle|^2 \delta(E_n - E_m). \quad (5.8)$$

By differentiating this expression with respect to the applied voltage, the differential conductance (DC) [2]

$$G(U) = \frac{dI}{dU} = \frac{\pi e^2}{2\hbar k_B T} \sum_{m,n} \frac{1}{\cosh^2 \frac{E_m - eU}{2k_B T}} |\langle n | H_T | m \rangle|^2 \delta(E_n - E_m) \quad (5.9)$$

is obtained, which is measured in experiments.

As mentioned above, the surface state spin polarization cannot simply be extracted from the total DC. Instead, one has to make use of the coupling of spin and propagation direction of surface electrons. A simple device to do so is shown in Fig. 5.2. When a voltage is applied between the aluminum electrode (Al) and the two metallic electrodes (M), placed on opposite sides of the aluminum electrode, spin polarized electrons are injected into the TI. Depending on their spin, which is conserved in the tunneling process, these electrons will end up at either of the two metallic electrodes since electrons with opposite spin move in opposite directions. The influence of scattering processes that alter the spin and thereby the propagation direction of surface electrons shall be neglected for the beginning. The DC with respect to a specified electrode can be calculated by introducing a function $f(\varphi)$ into the DC formula. $f(\varphi)$ gives the probability that an electron in topological surface states with initial movement direction defined by the in-plane polar angle φ ends up at the specified electrode [2]. For the case

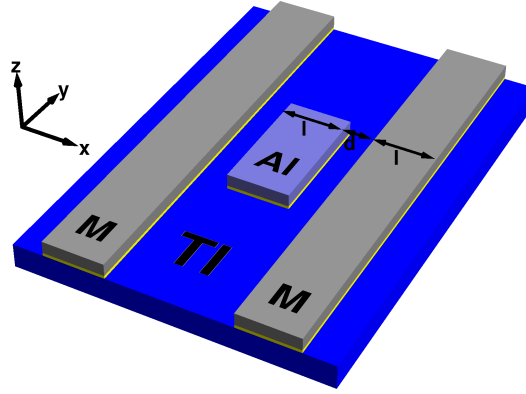


Figure 5.2: Most basic device for applying the method of Meservey and Tedrow to TIs. Electrons injected into the TI through the aluminum (Al) electrode are measured at either of the two metallic electrodes (M), depending on their spin. All electrodes are separated from the TI by an insulating layer (yellow). The large spatial extend of the device in y -direction, compared to the distance of the electrodes d , reduces the impact of boundary effects at the device ends to a negligible amount. For simplicity, the width l is assumed to be equal for all electrodes.

shown in Fig. 5.2, where all electrons with positive group velocity $v_x = \frac{1}{\hbar} \frac{\partial E}{\partial k_x} > 0$ end up at the right electrode, the corresponding angular dependent probability distribution is simply given by the function [2]

$$f(\varphi) = \begin{cases} 1 & \text{for } \varphi \in \left[-\frac{\pi}{2}, \frac{\pi}{2}\right] \\ 0 & \text{else.} \end{cases} \quad (5.10)$$

In order to derive a formula for the spin polarization, the analytical eigenstates and energies of the surface states are expanded up to second order in k_x and k_y . With $k = \sqrt{k_x^2 + k_y^2}$, the coefficients $v_1(k_x, k_y)$ and $v_2(k_x, k_y)$ (Eq. (3.35) and (3.36)) depend only on the in-plane polar angle φ

$$v_1(k_x, k_y) = \pm \frac{k_y + ik_x}{\sqrt{2}k} = \pm \frac{k(\sin \varphi + i \cos \varphi)}{\sqrt{2}k} = \pm \frac{1}{\sqrt{2}} e^{-i(\varphi - \frac{\pi}{2})}, \quad (5.11)$$

$$v_2(k_x, k_y) = \frac{1}{\sqrt{2}} \quad (5.12)$$

5 Meservey Tedrow method

and the eigenstates (Eq. (3.34)) become

$$\psi_{\pm}(\varphi) = \frac{1}{\sqrt{2}N} \begin{pmatrix} \pm \sqrt{\frac{M_1 - C_1}{M_1}} e^{-i(\varphi - \frac{\pi}{2})} \\ \sqrt{\frac{M_1 - C_1}{M_1}} \\ \pm \sqrt{\frac{M_1 + C_1}{M_1}} e^{-i(\varphi - \frac{\pi}{2})} \\ \sqrt{\frac{M_1 + C_1}{M_1}} \end{pmatrix} (e^{-\alpha_1 z} - e^{-\alpha_2 z}). \quad (5.13)$$

Remember, \pm is for eigenstates of the upper and lower part of the Dirac cone, respectively. Equation (5.13) describes surface states where the polarization lies solely in the surface plane and is always perpendicular to the in-plane momentum. As both orbitals have the same sign, these surface states are fully polarized. This is in contrast to the edge states of the 2D Hamiltonian used in the previous chapter, where different polarization directions of the two orbitals lead to an overall reduces polarization. In that case, the polarization was given by $\frac{C_2}{M_2}$. Here, to achieve a finite, tunable spin polarization $-1 \leq p \leq 1$, the sign of the third entry in Eq. (5.13) is reversed so that the orbitals have opposite spin, and the roots are rewritten in terms of the polarization $p = \frac{C_1}{M_1}$. As the spatial dependence is equal for all eigenstates and only the lattice position next to the insulating barrier is relevant for the DC, the spatial dependence can be dropped. Constant prefactors will cancel in the polarization formula, which is a quotient of DCs, and can be neglected as well. In a normalized form, the surface states then read [2]

$$\psi_{\pm}(p, \varphi) = \frac{1}{2} \begin{pmatrix} \pm \sqrt{1 + p} e^{-i(\varphi - \frac{\pi}{2})} \\ \sqrt{1 + p} \\ \mp \sqrt{1 - p} e^{-i(\varphi - \frac{\pi}{2})} \\ \sqrt{1 - p} \end{pmatrix}. \quad (5.14)$$

The corresponding energy eigenvalues are not affected by the sign change because the sign change is only a matter of the spin-orbit coupling term in z -direction, which does not enter into the surface state energy eigenvalues. When expanded up to second order in k_x and k_y , the energies E_{\pm} (Eq. (3.37)) depend only on the absolute value of the in-plane momentum and are independent of φ [2]

$$E_{\pm} = -\frac{C_1 M_0}{M_1} + \left(C_2 - \frac{C_1}{M_1} M_2 \right) k^2 \pm A_0 \sqrt{1 - \frac{C_1^2}{M_1^2}} k. \quad (5.15)$$

Using the same Hamiltonian Eq. (3.20), the aluminum film in the normal phase is modeled using parameters $C_{Al} \equiv C_1 = C_2 = 0.25\text{eV}$, $C_0 = -0.75\text{eV}$ and $A_0 = B_0 = M_0 = M_1 = M_2 = R_1 = R_2 = 0$. These parameters lead to four decoupled, degenerate bands with metallic dispersion. The Fermi level is located approximately in the middle of the bands so that the density of states is nearly constant in the energy range of the TI bulk gap. Eigenstates with

a certain polarization can be constructed by linearly combining the corresponding eigenstates

$$\psi(z, k_z) = \sin z k_z \begin{pmatrix} 1 \\ 0 \\ 0 \\ 0 \end{pmatrix}, \text{ etc.}, \quad (5.16)$$

which are basically those of an infinite one-dimensional potential well. So, for the required polarization in the x - y -surface plane, there are two degenerate eigenstates

$$\psi_{Al}^1(z, k_z, \varphi_{Al}) = \frac{1}{\sqrt{2}} \sin z k_z \begin{pmatrix} e^{-i\varphi_{Al}} \\ 1 \\ 0 \\ 0 \end{pmatrix}, \quad \psi_{Al}^2(z, k_z, \varphi_{Al}) = \frac{1}{\sqrt{2}} \sin z k_z \begin{pmatrix} 0 \\ 0 \\ e^{-i\varphi_{Al}} \\ 1 \end{pmatrix}. \quad (5.17)$$

Here, φ_{Al} is the in-plane polarization angle, and $\sin z k_z$ describes the spatial dependence in z -direction. In the following, $z = 1$, i.e. the surface lattice site, will be used. To assure energy and in-plane momentum conservation in the tunneling process, k_z is expressed in terms of energy E and total in-plane momentum k

$$k_z \approx \arccos \frac{C_0 + C_{Al}(2 + k^2) - E}{2C_{Al}}. \quad (5.18)$$

Equation (5.18) is obtained from the bulk dispersion Eq. (3.21) by expansion up to quadratic order in k_x and k_y and subsequent inversion. From Eq. (5.14) and (5.17), the transfer matrix elements of the junction can be calculated

$$|\langle \psi_{Al}^1 | H_T | \psi_{\pm} \rangle|^2 = \frac{1}{4} C_B^2 \sin^2 k_z(k) (1 + p) [1 \mp \sin(\varphi_{Al} - \varphi)], \quad (5.19)$$

$$|\langle \psi_{Al}^2 | H_T | \psi_{\pm} \rangle|^2 = \frac{1}{4} C_B^2 \sin^2 k_z(k) (1 - p) [1 \pm \sin(\varphi_{Al} - \varphi)]. \quad (5.20)$$

Depending on the polarization p , which was introduced as an asymmetry between the two orbitals, tunneling happens more into one orbital or the other, so that for $p = \pm 1$, the tunneling probability into one orbital vanishes completely. As the two aluminum states are degenerate, the sum of both matrix elements can already be calculated

$$|\langle \psi_{Al} | H_T | \psi_{\pm} \rangle|^2 \equiv |\langle \psi_{Al}^1 | H_T | \psi_{\pm} \rangle|^2 + |\langle \psi_{Al}^2 | H_T | \psi_{\pm} \rangle|^2 \quad (5.21)$$

$$= \frac{1}{2} C_B^2 \sin^2 k_z(k) [1 \mp p \sin(\varphi_{Al} - \varphi)]. \quad (5.22)$$

From this expression it can then be seen that even in the case of $p = \pm 1$, the tunneling probability into all surface states is nonzero except for the case when the polarization of TI and aluminum states is exactly antiparallel. Nevertheless, the probability gradually decreases away from the parallel configuration.

The superconducting phase of aluminum is introduced by multiplying these transfer matrix

5 Meservey Tedrow method

elements with the shifted BCS densities of states [22, 109]

$$N_{\pm}(E) = \text{Re} \frac{|E \pm \mu_B B| - i\Gamma}{\sqrt{(|E \pm \mu_B B| - i\Gamma)^2 - \Delta^2}}, \quad (5.23)$$

where the + (-) sign is for spins oriented antiparallel (parallel) with respect to the applied magnetic field. Both the superconducting gap Δ and the quasiparticle-lifetime broadening Γ depend on the quality of the aluminum film. For the gap $\Delta = 0.35\text{meV}$ was chosen, corresponding to a critical temperature of $T_c = 2.3\text{K}$. In high quality aluminum films, a higher T_c of $2.4\text{K}-2.5\text{K}$ [21, 106] results in slightly larger gap sizes up to $\Delta \approx 0.38\text{meV}$. The quasiparticle-lifetime broadening Γ produces a broadening of the peaks in the BCS density of states due to a finite lifetime of the Cooper pairs. Its value is chosen as $\Gamma = 0.03\text{meV}$ to approximately reproduce the broadening effects considered in Ref. [110]. The exact values for Δ and Γ are rather unimportant for the derivations shown here as long as $\Delta \gg \Gamma$, so that the features of the density of states remain clear.

When Eq. (5.21) and (5.23) are inserted into Eq. (5.9), the sum can be replaced by an integral over k and φ . For electrons with parallel orientation with respect to the magnetic field, the DC then reads

$$G_-(T, U, \varphi_{Al}) = \frac{\text{const.}}{T} \int_0^{k_0} dk k \int_{-\pi}^{\pi} d\varphi \left(f(\varphi) \frac{|\langle \psi_{Al} | H_T | \psi_+ \rangle|^2}{\cosh^2\left(\frac{E_+ - U}{2k_B T}\right)} N_-(E_+) \right. \\ \left. + f(\varphi - \pi) \frac{|\langle \psi_{Al} | H_T | \psi_- \rangle|^2}{\cosh^2\left(\frac{E_- - U}{2k_B T}\right)} N_-(E_-) \right), \quad (5.24)$$

where the two terms under the integral represent the upper and lower Dirac cone, respectively. While φ coincides with the propagation direction of surface electrons for the upper Dirac cone, the propagation direction is rotated by π for the lower Dirac cone. k_0 is a momentum cut-off to restrict the integral to the valid momentum range of the surface state approximation. By making the reasonable assumption that $f(\varphi) = f(-\varphi)$, i.e. the device is symmetric with respect to the x - z -plane, the φ -integral of the lower Dirac cone can be rewritten as

$$\int_{-\pi}^{\pi} d\varphi [1 + p \sin(\varphi_{Al} - \varphi)] f(\varphi - \pi) \\ \stackrel{(\varphi' = \varphi - \pi)}{=} \int_{-2\pi}^0 d\varphi' [1 - p \sin(\varphi_{Al} - \varphi')] f(\varphi') \\ \stackrel{(f(\varphi + 2\pi) = f(\varphi))}{=} \int_{-\pi}^{\pi} d\varphi f(\varphi) [1 - p(\sin \varphi_{Al} \cos \varphi - \cos \varphi_{Al} \sin \varphi)] \\ \stackrel{(f(\varphi) = f(-\varphi))}{=} \int_{-\pi}^{\pi} d\varphi f(\varphi) [1 - p \sin \varphi_{Al} \cos \varphi]. \quad (5.25)$$

As the last steps also apply to the upper Dirac cone, the two φ -integrals are the same. So, $G_-(T, U, \varphi_{Al})$ can be separated into a product of a φ -integral, containing the device geometry

and relative polarization of topological surface states and aluminum film, and a k -integral, denoted by $G'_-(T, U)$, containing the densities of state

$$\begin{aligned}
G_-(T, U, \varphi_{Al}) &= \int_{-\pi}^{\pi} d\varphi f(\varphi) (1 - p \sin \varphi_{Al} \cos \varphi) \frac{\text{const.}}{T} \int_0^{k_0} dk k \\
&\quad \cdot \left(\frac{\sin^2 k_z(k) N_-(E_+)}{\cosh^2 \left(\frac{E_+ - U}{2k_B T} \right)} + \frac{\sin^2 k_z(k) N_-(E_-)}{\cosh^2 \left(\frac{E_- - U}{2k_B T} \right)} \right) \\
&= \int_{-\pi}^{\pi} d\varphi f(\varphi) (1 - p \sin \varphi_{Al} \cos \varphi) G'_-(T, U). \tag{5.26}
\end{aligned}$$

An analogous calculation yields for electrons with spin antiparallel to the magnetic field

$$G_+(T, U, \varphi_{Al}) = \int_{-\pi}^{\pi} d\varphi f(\varphi) (1 + p \sin \varphi_{Al} \cos \varphi) G'_+(T, U), \tag{5.27}$$

where $G'_+(T, U)$ depends on $N_+(E)$ instead of $N_-(E)$. The total DC is then given by the sum of Eq. (5.26) and Eq. (5.27)

$$G(T, U, \varphi_{Al}) = G_-(T, U, \varphi_{Al}) + G_+(T, U, \varphi_{Al}), \tag{5.28}$$

which, in the case of the device geometry Eq. (5.10), equates to

$$G(T, U, \varphi_{Al}) = (\pi - 2p \sin \varphi_{Al}) G'_-(T, U) + (\pi + 2p \sin \varphi_{Al}) G'_+(T, U). \tag{5.29}$$

A numerical solution of Eq. (5.29) is shown in Fig. 5.3 for $T = 0.4\text{K}$, $\varphi_{Al} = \frac{\pi}{2}$, $p = 1$, and $\mu = 0.2\text{eV}$. The chemical potential μ is chosen in the lower Dirac cone, close to the Dirac point, where the hexagonal deformation of the Fermi surface and the out-of-plane polarization are small. For comparison, the DC calculated with numerical eigenstates of the full Hamiltonian Eq. (3.20) is shown as well. These eigenstates were calculated on a hexagonal lattice with 50 lattice sites in z -direction and in-plane momenta k_x and k_y uniformly distributed over the first Brillouin zone with a discretization of $\frac{2}{\sqrt{3}} \frac{2\pi}{N}$. To achieve a sufficient energy resolution, $N = 48000$ was chosen, corresponding to a real space sample width of about $20\mu\text{m}$. The propagation direction of surface electrons was determined from how the energy eigenvalues change with small variations of k_x and k_y , i.e. from a difference quotient. Aluminum states are described by the analytical expressions in Eq. (5.17). The DC is then obtained from Eq. (5.24) and an analogous expression for an antiparallel field by replacing the k - and φ -integral with a sum over all TI eigenstates and aluminum states that satisfy energy and in-plane momentum conservation. Both curves are in good agreement with only small deviations due to the simplifications made in the analytical surface state approximation.

Now that an analytical expression for the DC is known, a formula for the spin polarization can be derived. Assume that the densities of states of the TI and the aluminum film are constant as a function of energy for the energy scale of the superconducting gap, aside from the BCS density of states. Then, $G'_-(T, U)$ and $G'_+(T, U)$ can be expressed in terms of an unsplit

5 Meservey Tedrow method

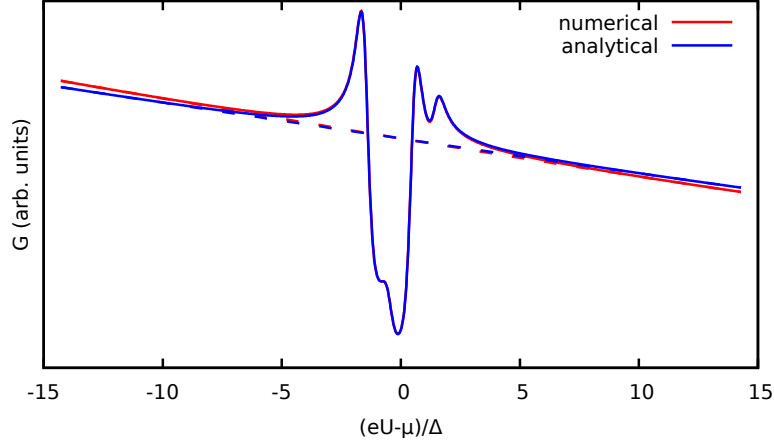


Figure 5.3: Calculated total DC of an AI/IT junction with respect to the right electrode of the device shown in Fig. 5.2. Parameters are $B = 3\text{T}$, $T = 0.4\text{K}$, $\varphi_{Al} = \frac{\pi}{2}$, $p = 1$, and $\mu = 0.2\text{eV}$. The red curve is obtained from numerical integration of Eq. (5.29), while the blue curve is calculated from numerical eigenstates of the full Hamiltonian, including out-of-plane polarization terms. Dashed lines are third order polynomials $h(U)$, fitted to the outermost tenth on each side of the DC curves.

DC $G'(T, U)$, in analogy to Ref. [22]. It is also assumed that there is no significant spin-orbit coupling, which is small for thin aluminum films. With spin-orbit coupling, the separate densities of state are no longer symmetric around μ , while the unsplit density of states is symmetric [111]. This effect, however, is neglected in this thesis. When effects like spin-orbit coupling are included into the determination of the polarization of ferromagnets, this is done by a comparison of theoretical and experimental curves [110], which should be applicable here as well.

As can be seen in Fig. 5.3, the densities of state are clearly not constant in the present case because of the Dirac cone like dispersion of the topological surface states. This issue can be easily solved by fitting a low order polynomial $h(U)$ to the DC (dashed lines in Fig. 5.3), while sparing out the part with strong influence of the BCS density of states, and then multiplying the whole DC with the inverse $\frac{1}{h(U)}$ (see Fig. 5.4). After this procedure, the small deviations of the two DC curves in Fig. 5.4 are no longer present, indicating that Eq. (5.28) is a good approximation.

In terms of the unsplit DC $G'(T, U)$ and

$$F_{\pm}(\varphi_{Al}) = \int_{-\pi}^{\pi} d\varphi f(\varphi) (1 \pm p \sin \varphi_{Al} \cos \varphi), \quad (5.30)$$

the four peaks of the total DC in Fig. 5.4 can then be written (in analogy to Ref. [22]) from left

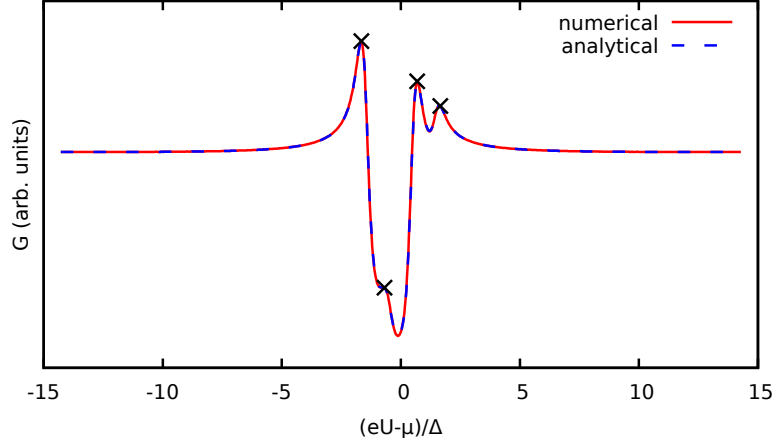


Figure 5.4: DC curves shown in Fig. 5.3 after multiplication with $\frac{1}{h(U)}$. Analytical approximation (blue, dotted) and numerical calculation (red, solid) are now in very good agreement. Black crosses mark the positions of the four peaks of the analytical approximation. For details see main text.

to right as

$$g_1 = F_+(\varphi_{Al}) G'(T, -x + b) + F_-(\varphi_{Al}) G'(T, -x - b), \quad (5.31)$$

$$g_2 = F_+(\varphi_{Al}) G'(T, -x + 3b) + F_-(\varphi_{Al}) G'(T, -x + b), \quad (5.32)$$

$$g_3 = F_+(\varphi_{Al}) G'(T, x - b) + F_-(\varphi_{Al}) G'(T, x - 3b), \quad (5.33)$$

$$g_4 = F_+(\varphi_{Al}) G'(T, x + b) + F_-(\varphi_{Al}) G'(T, x - b). \quad (5.34)$$

Here, $ex \sim \Delta + \mu_B B$ is the energy difference between an outer peak (g_1 or g_4) and the chemical potential μ . $eb \sim \mu_B B$ is the shift of the BCS density of states in a magnetic field. Note that these values for x and b and therewith the peak positions are only approximate values. Therefore, not all peaks may be met exactly by Eq. (5.31)-(5.34) due to broadening effects of the BCS density of states. In principle, the positions can be chosen arbitrarily as long as they are chosen symmetric around the chemical potential μ . To reduce errors, it is therefore best to choose the positions so that the slope of the DC curve is small at these positions. In Fig. 5.4, the positions (crosses) are chosen so that the highest outer and inner peak are met exactly. The two remaining peak positions are then given by the symmetry requirement.

By using the symmetry $G'(T, U) = G'(T, -U)$ with respect to the chemical potential μ , $G'(T, U)$ cancels when calculating the following quotient:

$$\frac{(g_4 - g_2) - (g_1 - g_3)}{(g_4 - g_2) + (g_1 - g_3)} = \frac{F_+(\varphi_{Al}) - F_-(\varphi_{Al})}{F_+(\varphi_{Al}) + F_-(\varphi_{Al})} = p \sin \varphi_{Al} \frac{\int_{-\pi}^{\pi} d\varphi f(\varphi) \cos \varphi}{\int_{-\pi}^{\pi} d\varphi f(\varphi)}. \quad (5.35)$$

5 Meservey Tedrow method

This expression can then be solved for the polarization p

$$p = \frac{(g_4 - g_2) - (g_1 - g_3) \frac{\gamma}{\sin \varphi_{Al}}}{(g_4 - g_2) + (g_1 - g_3) \frac{\gamma}{\sin \varphi_{Al}}}. \quad (5.36)$$

Calculation of the polarization p thus only requires knowledge of the relative height of the four peaks in the total DC and a factor [2]

$$\gamma = \frac{\int_{-\pi}^{\pi} d\varphi f(\varphi)}{\int_{-\pi}^{\pi} d\varphi f(\varphi) \cos \varphi}, \quad (5.37)$$

accounting for the geometry of the device. The geometrical factor γ can be calculated for arbitrary devices as long as $f(\varphi) = f(-\varphi)$, and some interesting device examples are shown in section 5.1.2. For the basic device (Eq. (5.10)) shown in Fig. 5.2, $\gamma = \frac{\pi}{2}$ is obtained. When this value is inserted into Eq. (5.36) along with the height of the four peaks in Fig. 5.4, the resulting polarization values are $p \approx 0.9995$ for the analytical expression and $p \approx 1.0038$ for the full numerical calculation. Numerical calculations for the other metallic electrode on the opposite side of the aluminum electrode yield $p \approx -1.0038$, consistent with the locking of spin and momentum.

The absolute values are in good agreement with the actual in-plane spin polarization of (about) 100%, however with the wrong sign. As the spin of surface states in the lower Dirac cone rotates counterclockwise around the Fermi surface, according to Eq. (5.13), surface states with positive propagation direction must have negative spin. Additionally, in the derivation of Eq. (5.36), the surface state spin polarization was always perpendicular to the momentum. As this may not always be the case, it is useful to rewrite the formula so that it contains the relative orientation of spin polarization and applied magnetic field $\Delta\varphi_{Al}$ instead of the absolute field orientation φ_{Al}

$$p = \frac{(g_1 - g_3) - (g_4 - g_2) \frac{\gamma}{\cos \Delta\varphi_{Al}}}{(g_1 - g_3) + (g_4 - g_2) \frac{\gamma}{\cos \Delta\varphi_{Al}}}. \quad (5.38)$$

So, by maximizing the DC, i.e. minimizing $\Delta\varphi_{Al}$, the direction of the surface state spin polarization is obtained. For $\Delta\varphi_{Al} = 0$ and $\gamma = 1$, Eq. (5.38) coincides with that of Tedrow and Meservey [22]. $\gamma = 1$ is obtained for 2D devices with propagation only along one axis, i.e. $f(\varphi) = \delta(\varphi)$. In that case, all electrons reaching the metallic electrode have the same spin. Real 2D setups that investigate the edges of a thin TI sheet are difficult to realize, especially because of the out-of-plane spin of the edge states. A device for approximating a 2D device on a 3D surface is presented in section 5.1.2.

5.1.1 Influence of the out-of-plane polarization

By application of an additional gate voltage, the chemical potential of the TI can be changed and the energy dependence of the spin polarization may be studied. Figure 5.5 shows the obtained polarization values based on the full Hamiltonian for chemical potentials throughout the bulk gap. Only values near the Dirac point are missing because the kink in the density of

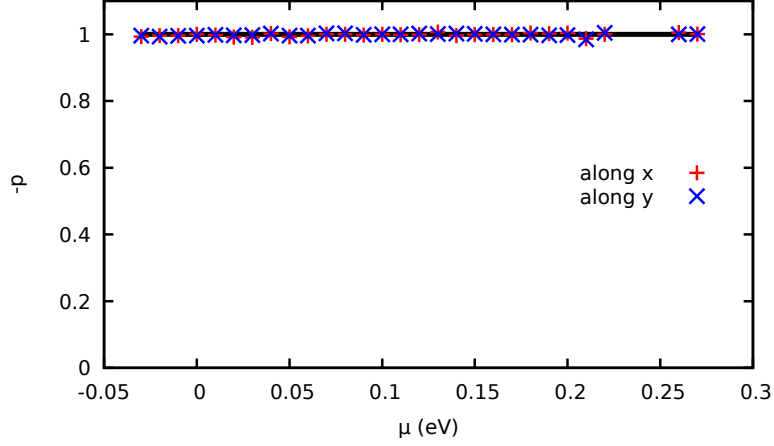


Figure 5.5: Dependence of the spin polarization on the chemical potential μ . Polarization values (crosses) are obtained from numerical DC curves based on the full Hamiltonian for $T = 0.4\text{K}$ and $B = 3\text{T}$. There are no systematic deviations from $p = -1$ (black line) for all μ as well as different crystal orientations.

states of the surface states prohibits a direct fit of the DC curve, which is necessary to remove energy dependencies of the densities of states. "Measurements" are shown for two different orientations of the TI crystal with respect to the device geometry, i.e. one measurement has been performed along the x -direction, like before, and one along the y -direction. Except for small random deviations, both measurements yield $p \approx -1$, independent of μ . Due to the hexagonal deformation of the Fermi surface along with an out-of-plane polarization component, this is not intuitively clear. To estimate the impact of the out-of-plane polarization onto the measured in-plane polarization, the analytical surface state approximation is extended to include an out-of-plane tilt of the surface state spin.

The out-of-plane polarization $q(E, \varphi)$ depends on energy and oscillates around the Fermi surface with an alternating sign in steps of $\Delta\varphi = \frac{\pi}{3}$. Assuming that the in-plane polarization remains perpendicular to the in-plane momentum, the surface states are approximated as

$$\psi'_{\pm}(p, q_0, \varphi) = \frac{1}{2} \begin{pmatrix} \pm\sqrt{1 \pm q_0 \cos 3\varphi} \sqrt{1 + p} e^{-i(\varphi - \frac{\pi}{2})} \\ \sqrt{1 \mp q_0 \cos 3\varphi} \sqrt{1 + p} \\ \mp\sqrt{1 \pm q_0 \cos 3\varphi} \sqrt{1 - p} e^{-i(\varphi - \frac{\pi}{2})} \\ \sqrt{1 \mp q_0 \cos 3\varphi} \sqrt{1 - p} \end{pmatrix}, \quad (5.39)$$

with spin expectation values

$$p'_x = \langle \psi'_{\pm} | \Sigma_x | \psi'_{\pm} \rangle = \pm\sqrt{1 - q_0^2 \cos^2 3\varphi} p \sin \varphi, \quad (5.40)$$

$$p'_y = \langle \psi'_{\pm} | \Sigma_y | \psi'_{\pm} \rangle = \mp\sqrt{1 - q_0^2 \cos^2 3\varphi} p \cos \varphi, \quad (5.41)$$

$$p'_z = \langle \psi'_{\pm} | \Sigma_z | \psi'_{\pm} \rangle = \pm q_0 \cos 3\varphi, \quad (5.42)$$

5 Meservey Tedrow method

satisfying $n = \sqrt{p_x'^2 + p_y'^2 + p_z'^2} = p$. $q_0(E)$ is the maximum of the out-of-plane polarization at energy E (the energy dependence is omitted in most equations) and $\cos 3\varphi$ the angular dependence. The quality of this approximation is shown later in section 6.2. With this new approximation, the matrix elements become

$$|\langle \psi_{Al}^1 | H_T | \psi_{\pm}' \rangle|^2 = \frac{1}{4} C_B^2 \sin^2 k_z(k) (1+p) \left[1 \mp \sqrt{1 - q_0^2 \cos^2 3\varphi} \sin(\varphi_{Al} - \varphi) \right], \quad (5.43)$$

$$|\langle \psi_{Al}^2 | H_T | \psi_{\pm}' \rangle|^2 = \frac{1}{4} C_B^2 \sin^2 k_z(k) (1-p) \left[1 \pm \sqrt{1 - q_0^2 \cos^2 3\varphi} \sin(\varphi_{Al} - \varphi) \right], \quad (5.44)$$

and their sum is

$$|\langle \psi_{Al} | H_T | \psi_{\pm}' \rangle|^2 = \frac{1}{2} C_B^2 \sin^2 k_z(k) \left[1 \mp p \sqrt{1 - q_0^2 \cos^2 3\varphi} \sin(\varphi_{Al} - \varphi) \right]. \quad (5.45)$$

Under the assumption of low temperature, so that $q_0(E) \approx q_0(U)$, $\sqrt{1 - q_0^2 \cos^2 3\varphi}$ can be handled as an additional factor to p in the next calculation steps because $\cos^2 3\varphi$, like $f(\varphi)$, is symmetric around $\varphi = 0$. Accordingly, the factors $F_{\pm}(\varphi_{Al})$ simply change into

$$F'_{\pm}(\varphi_{Al}) = \int_{-\pi}^{\pi} d\varphi f(\varphi) \left(1 \pm p \sqrt{1 - q_0^2 \cos^2 3\varphi} \sin \varphi_{Al} \cos \varphi \right). \quad (5.46)$$

The quotient of the peak positions

$$\begin{aligned} \frac{(g_4 - g_2) - (g_1 - g_3)}{(g_4 - g_2) + (g_1 - g_3)} &= \frac{F'_+(\varphi_{Al}) - F'_-(\varphi_{Al})}{F'_+(\varphi_{Al}) + F'_-(\varphi_{Al})} \\ &= p \sin \varphi_{Al} \frac{\int_{-\pi}^{\pi} d\varphi f(\varphi) \sqrt{1 - q_0^2 \cos^2 3\varphi} \cos \varphi}{\int_{-\pi}^{\pi} d\varphi f(\varphi)} \end{aligned} \quad (5.47)$$

therefore results in the same relation

$$p = \frac{(g_4 - g_2) - (g_1 - g_3)}{(g_4 - g_2) + (g_1 - g_3)} \frac{\gamma'}{\sin \varphi_{Al}} \quad (5.48)$$

with a modified factor

$$\gamma' = \frac{\int_{-\pi}^{\pi} d\varphi f(\varphi)}{\int_{-\pi}^{\pi} d\varphi f(\varphi) \sqrt{1 - q_0^2 \cos^2 3\varphi} \cos \varphi}. \quad (5.49)$$

For the case shown in Fig. 5.5, a maximal out-of-plane polarization of about $q_0 \approx 0.17$ at the lower edge of the bulk gap results in a relative change of γ of only $\frac{\gamma'}{\gamma} \approx 1.008$ for measurements along the x -direction. So, the influence of the out-of-plane polarization is only of the order of the accuracy with which the polarization can be read from the DC curves and is far from being detectable in real experiments. The reason for this small influence of the out-of-plane polarization in 3D devices is basically that the overlap of eigenstates of the aluminum electrode with the out-of-plane component of TI surface states is the same for spin-up and

spin-down states and for all φ_{Al} .

For measurements along the y -direction, the impact of the out-of-plane polarization is even slightly smaller ($\frac{\gamma'}{\gamma} \approx 1.007$) because the out-of-plane spin is zero for surface states with momentum parallel to the measurement axis, which have the largest contribution to the DC. In the case of a measurement along x , the out-of-plane spin was maximal along the measurement axis. As the out-of-plane spin component of the new surface state approximation Eq. (5.39) is not invariant under arbitrary in-plane rotations, γ' depends on the relative orientation of the crystal with respect to the device. To get γ' for a measurement along y , one has to rotate the crystal with respect to the device axes, i.e. in this case replace $\cos 3\varphi$ with $\cos(3\varphi - \frac{\pi}{2})$ in Eq. (5.49), because a rotation of the device, i.e. $f(\varphi) \rightarrow f(\varphi - \frac{\pi}{2})$, violates the symmetry assumption $f(\varphi) = f(-\varphi)$.

The impact of the out-of-plane component becomes stronger in 2D device structures as $f(\varphi) = \delta(\varphi)$ yields $\frac{\gamma'}{\gamma} \approx 1.015$. However, when the crystal is rotated by $\frac{\pi}{2}$ with respect to the device, the out-of-plane polarization is $q = 0$ along the measurement axis, i.e. $\frac{\gamma'}{\gamma} = 1$. So, the out-of-plane component can be avoided by measurements along different crystal axes. As the effect is still very small, it is, however, unlikely that the out-of-plane spin can be measured from the angular variation of γ' .

5.1.2 Geometrical factor

The essential difference between the polarization formula for ferromagnets and Eq. (5.38) is the geometrical factor γ . As already small changes of γ alter the obtained polarization value, it is crucial to derive γ as precise as possible. In the following, the function $f(\varphi)$, representing the probability for an electron starting at an angle φ inside the TI to end up at a specified electrode, will be derived for some interesting cases. $f(\varphi)$ can be obtained by dividing the number of trajectories starting at an angle φ that reach the electrode by the total number of trajectories.

Basic geometry with scattering

So far, it was assumed for the basic device that an electron initially moving in positive x -direction will end up at the right electrode. However, this is only true as long as there are no spin-changing scattering processes. In real devices, there will always be scattering and an electron will thereby gradually change its movement direction. Only elastic scattering processes that directly flip the spin to the opposite orientation are forbidden in the absence of time-reversal symmetry breaking perturbations. As scattering processes reduce the apparent spin polarization measured by the device, scattering processes should be compensated for by an increased geometrical factor γ .

In the case of the device shown in Fig. 5.2, the path length for an electron starting below the Al electrode towards the metallic electrode in positive x -direction is $\frac{x}{\cos \varphi}$. Here, φ is the movement angle with respect to the x -axis and x the distance of two lines parallel to the y -axis, one in the Al electrode and one in the M electrode. When ξ is the mean spin diffusion length, i.e. the length after which an electron loses all information on its original spin, the

5 Meservey Tedrow method

probability for an electron to reach the other line is

$$P_r(x, \varphi) = \frac{1}{2} \left(1 + e^{-\frac{x}{\xi |\cos \varphi|}} \right) \quad (5.50)$$

and correspondingly to be scattered to the opposite direction

$$P_s(x, \varphi) = \frac{1}{2} \left(1 - e^{-\frac{x}{\xi |\cos \varphi|}} \right). \quad (5.51)$$

So, the DC with respect to the right electrode consists of those electrons that initially move in positive x -direction and are not scattered and those initially moving in negative direction but that are then scattered towards the positive direction. By averaging over all possible distances $d \leq x \leq d + 2l$ of the two lines, this results in

$$f(\varphi) = \int_d^{d+2l} dx \frac{l - |x - d - l|}{l^2} \frac{1}{2} \begin{cases} \left(1 + e^{-\frac{x}{\xi \cos \varphi}} \right) & \text{if } \varphi \in \left[-\frac{\pi}{2}, \frac{\pi}{2} \right] \\ \left(1 - e^{-\frac{x}{\xi \cos \varphi}} \right) & \text{if } \varphi \in \left[-\pi, -\frac{\pi}{2} \right], \left[\frac{\pi}{2}, \pi \right], \end{cases} \quad (5.52)$$

where l is the width of the electrodes and d their spatial separation (see Fig. 5.2). From this expression, the geometrical factor γ has to be calculated numerically for specified values of d , l and ξ (see Fig. 5.9). As $f(\varphi)$ approaches $\frac{1}{2}$ for all φ if ξ is large compared to x , i.e. all spin information is lost, the ratio $\frac{x}{\xi}$ should be kept small in order to measure the spin polarization.

Semi circles

Another approach to deal with small spin diffusion lengths is to reduce path lengths as much as possible. In the device shown in Fig. 5.6, which consists of a circular aluminum electrode enclosed by two metallic semi circles, the mean path length is equal for all φ . Besides, no boundary effects at the device edges are involved as the aluminum electrode is completely enclosed.

For a given angle φ , electrons from the circular fragment with area

$$A' = R_i^2 \arccos \left(1 - \frac{h}{R_i} \right) - (R_i - h) \sqrt{2R_i h - h^2} \quad (5.53)$$

cannot reach the right electrode. Thus, for an electron moving under an angle φ , the probability to reach the right electrode is $\frac{A-A'}{A}$, where $A = \pi R_i^2$ is the area of the aluminum electrode with radius R_i . The height $h = R_i - R_o \cos \varphi$ of the fragment can be expressed in terms of the two radii and φ , and after some simplifications, A' reads

$$A' = R_i^2 \arccos \left(\frac{R_o}{R_i} \cos \varphi \right) - R_o R_i \cos \varphi \sqrt{1 - \frac{R_o^2}{R_i^2} \cos^2 \varphi}. \quad (5.54)$$

As the outer radius R_o is bigger than the inner radius R_i , $\frac{R_o}{R_i} \cos \varphi$ becomes bigger than one when the red line in Fig. 5.6 does not cut the inner circle. In that case, A' becomes imaginary,

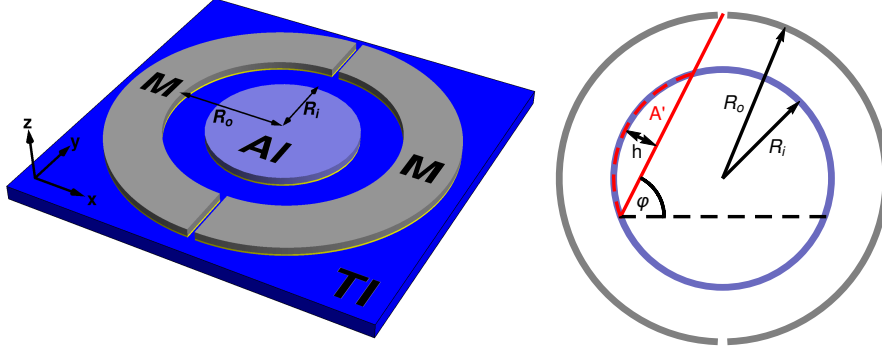


Figure 5.6: In a device structure with a circular aluminum electrode enclosed by two metallic electrodes formed as semi circles, the path length is independent of the propagation angle φ and boundary effects are reduced. The right panel shows a sketch for the construction of $f(\varphi)$. Electrons from the red encircled area A' do not reach the right electrode but the left.

and the probability for an electron to reach the right metallic electrode is therefore given by the real part of $\frac{A-A'}{A}$:

$$f(\varphi) = 1 - \frac{1}{\pi} \operatorname{Re} \left[\arccos \left(\frac{R_o}{R_i} \cos \varphi \right) - \frac{R_o}{R_i} \cos \varphi \sqrt{1 - \frac{R_o^2}{R_i^2} \cos^2 \varphi} \right] \quad (5.55)$$

$$\stackrel{(R_o \approx R_i)}{\approx} 1 - \frac{1}{\pi} (|\varphi| - \cos \varphi \sin |\varphi|). \quad (5.56)$$

Analytical solutions for γ can only be obtained for the two limiting cases $R_o \approx R_i$ ($\gamma = \frac{3}{16} \pi^2$) and $\frac{R_i}{R_o} \rightarrow 0$ ($\gamma = \frac{\pi}{2}$). The latter is the same factor as for the basic device geometry.

Approximate 2D

Device geometries discussed so far are only capable of measuring the mean in-plane spin polarization. This is sufficient if the investigated material has in-plane rotation symmetry or at least can be approximated as such, like the top surface of the Bi_2Se_3 class of materials. In materials without in-plane rotation symmetry, e.g. the side surfaces of materials of the Bi_2Se_3 class [2], the polarization can be very anisotropic and the mean spin polarization is thus less meaningful. To get the full angular dependence of the spin polarization, one has to reduce the angle from which electrons are detected. A device geometry capable of this (Fig. 5.7) was presented in Ref. [2] to mimic a 2D tunnel magnetoresistance device on the surface of a 3D TI, and is discussed in the following. It consists of two small electrodes of length l and height h , separated by a distance d . Here, one of these is the (injecting) aluminum electrode and

5 Meservey Tedrow method

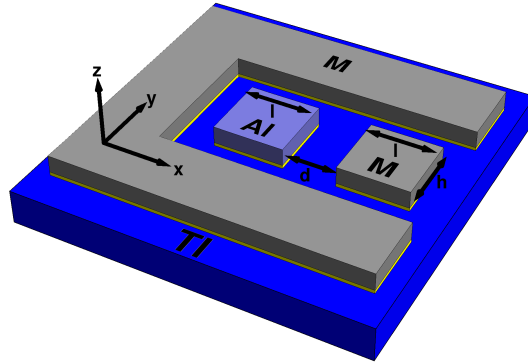


Figure 5.7: Device structure for selectively measuring the angular dependence of the surface state spin polarization. Only electrons moving in the direction of the small metallic electrode contribute to the measured DC. All other electrons are captured by the U-shaped metallic electrode. Modified from Ref. [2].

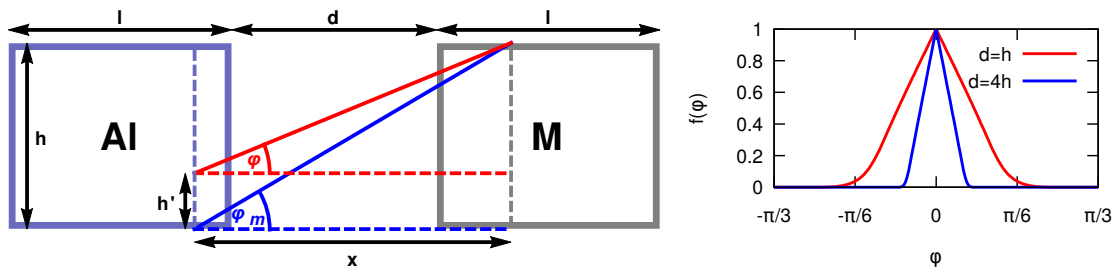


Figure 5.8: Sketch for deriving the geometrical function $f(\varphi)$ for the device structure shown in Fig. 5.7 (left panel), and angular dependence of $f(\varphi)$ (right panel) for $l = h$ and two different values of distance d . $f(\varphi)$ becomes more strongly focused around $\varphi = 0$ when going from $d = h$ (red line) to $d = 4h$ (blue line). Figures are reproduced and modified from Ref. [2].

one the (extracting) metallic electrode. Another metallic electrode, partly enclosing the small electrodes, captures all electrons not moving in the direction of the small metallic electrode so that only electrons from a small angular fraction are detected. The angular fraction can be tuned by the ratio of electrode height h and spatial separation d .

The function $f(\varphi)$ can be derived from the sketch shown in the left panel of Fig. 5.8. Just like for the basic geometry with scattering, two parallel lines, separated by a distance x , in the two small electrodes are considered. Electrons starting at an angle φ from the line in the aluminum electrode can only reach the line in the metallic electrode if they come from the top or bottom fraction of the line of size $h' = h - x \tan |\varphi|$, where φ is limited by $|\varphi| \leq \varphi_m = \arctan \frac{h}{x}$. So,

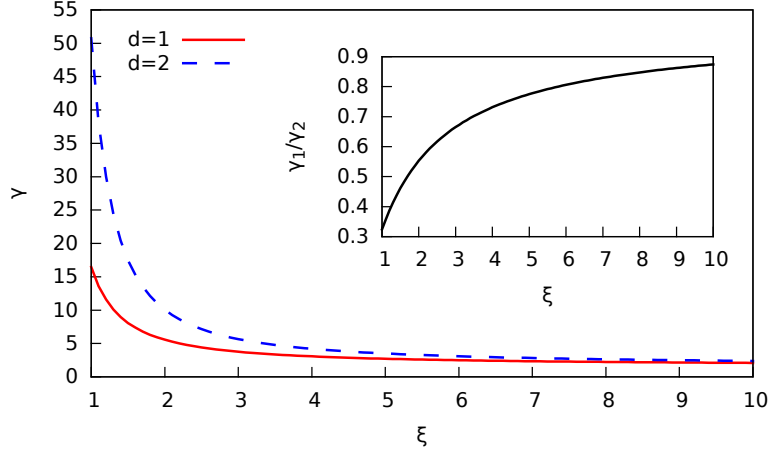


Figure 5.9: Geometrical factor γ for the basic device geometry as a function of spin diffusion length ξ for two distances d and $l = 1$. ξ can be obtained from the quotient of these curves (inset), which is independent of the polarization. To get an accurate result, both distances and ξ should be of the same order of magnitude.

by averaging over all distances $d \leq x \leq d + 2l$, the angular dependent probability $\frac{h'}{h}$ becomes

$$f(\varphi) = \int_d^{d+2l} dx \frac{l - |x - d - l|}{l^2} \left(1 - \frac{x}{h} \tan |\varphi|\right) \Theta \left(\arctan \frac{h}{x} - |\varphi|\right), \quad (5.57)$$

where the Heaviside step function Θ restricts φ to the allowed range for a given x . From this expression, γ can be calculated numerically for specified values of d , l and h . The angular dependence of Eq. (5.57) is shown for some example values in the right panel of Fig. 5.8, demonstrating that $f(\varphi)$ is strongly focused around $\varphi = 0$. This can also be seen from the corresponding γ factors, $\gamma \approx 1.0226$ for $d = h$ and $\gamma \approx 1.0034$ for $d = 4h$, i.e. γ approaches the 2D value $\gamma = 1$ ($f(\varphi) = \delta(\varphi)$). In both cases, $l = h$.

In the derivation of $f(\varphi)$, the U-shaped metallic electrode played no role, and therefore, its exact shape needs not to be specified as long as it captures all electrons not moving in the direction of the small metallic electrode. It could as well be split into multiple small electrodes in order to measure the spin polarization along different crystal axes in one device. For that purpose, a modified version of the circular device with $R_o \gg R_i$ and the metallic semi circles split into multiple smaller parts might be most suitable.

5.2 Spin diffusion length

Besides a high spin polarization of surface states and a large bulk gap, a long spin diffusion length is one of the most important requirements on TIs for spintronic applications. As has been shown in section 5.1.2, the geometrical factor can be modified to include spin diffusion. The linear dependence of geometrical factor and apparent spin polarization therefore allows

5 Meservey Tedrow method

to measure the geometrical factor for a given spin polarization instead of the reverse process. When all other parameters are known, the spin diffusion length can be obtained by a simple fit. If the apparent spin polarization is unknown, the spin diffusion length can still be obtained from how the geometrical factor changes with the distance of the aluminum and metallic electrode. This requires multiple devices because, even if no bias voltage is applied to certain metallic electrodes in a device with multiple parallel electrodes, tunneling processes between the TI and these electrodes may change the polarization and propagation direction of surface electrons. These devices, however, should be build from the same sample to reduce errors due to varying material qualities, i.e. different polarization values and spin diffusion lengths. Then it can be assumed that the polarization is the same for different distances d_i between aluminum and metallic electrode, i.e.

$$p = \chi_i(d_i) \gamma_i(d_i) \quad (5.58)$$

with

$$\chi = \frac{(g_1 - g_3) - (g_4 - g_2)}{(g_1 - g_3) + (g_4 - g_2)} \frac{1}{\cos \Delta\varphi_{Al}}. \quad (5.59)$$

So, the quotient

$$\frac{\gamma_1(d_1)}{\gamma_2(d_2)} = \frac{\chi_2(d_2)}{\chi_1(d_1)} \quad (5.60)$$

is independent of the unknown polarization, and the spin diffusion length can be obtained by a fit to calculated quotients for different diffusion lengths. This is shown exemplarily in Fig. 5.9 for the basic device with spin scattering, but it would work for other device structures as well. In order to get accurate results, ξ , d_1 , d_2 , and $|d_1 - d_2|$ should ideally be of the same order of magnitude. Too large distances compared to ξ result in too small measured signals and too small distances in too small variations of $\frac{\gamma_1}{\gamma_2}$ as a function of ξ .

Because of varying material qualities, it is reasonable to always first measure the spin diffusion length of a material before measuring its spin polarization in order to get results that are as precise as possible.

5.3 Summary

Meservey and Tedrow have shown that the BCS density of states of superconducting aluminum films splits in a strong parallel magnetic field. By measuring the DC of tunnel junctions with ferromagnets, they were able to measure the polarization of the ferromagnet. In this chapter, it has been shown that, by measuring the differential conductance with respect to electrodes in defined spatial directions, the in-plane spin polarization of topological surface states can be measured. For that purpose, the polarization formula by Meservey and Tedrow has to be modified to include the device geometry. More complex device geometries allow measurements of the momentum dependence of the polarization for anisotropic surfaces. Even though the surface states can have a significant momentum dependent out-of-plane spin component, the measured polarization is shown to be basically only the polarization of the in-plane component. Aside from the spin polarization, also the spin diffusion length of

5.3 Summary

topological surface states should be measurable by inverting the polarization formula, even if the spin polarization is unknown.

6 Spin Hall effect tunneling spectroscopy

The method of Meservey and Tedrow, discussed in the previous chapter, could be great for measuring the spin of electrons in topological surface states. However, it can only measure the in-plane spin component because the measured in-plane polarization is basically unaffected by an out-of-plane spin component (see section 5.1.1). To get a measure of the out-of-plane component, tunneling electrons with out-of-plane spin are needed, which can be realized in a tunnel junction with a ferromagnet (FM).

Liu *et al.* [23] developed a method, which they called spin Hall effect tunneling spectroscopy. This method allows to study the charge spin conversion efficiency of materials, i.e. the spin Hall angle, in a tunnel junction with a FM. In conventional (scanning) tunneling spectroscopy (STS), material properties are extracted from the dI/dV characteristics of an unpolarized tunneling current. By applying a bias voltage, the energy dependent density of states and therefore also the energy gap can be measured. STS measurements on TIs indeed show densities of states in consistence with ARPES measurements [25, 112]. In SHE tunneling spectroscopy, a polarized current is injected into the investigated material and, in the presence of strong spin-orbit coupling, gives rise to a measurable transverse voltage. The functioning of this new method has been shown by Liu *et al.* for normal metals [23], where the transverse voltage originates from the SHE, and for TIs [24], where it originates from the spin-momentum locking of surface states. A schematic of the device for the TI case is shown in Fig. 6.1.

In this chapter, it is shown that the SHE tunneling spectroscopy may be used to measure a relation between in-plane and out-of-plane spin polarization of topological surface states. Time-reversal symmetry requires that the in-plane spin rotates around the Fermi surface because states with opposite momentum must have opposite spin. As the same holds for the out-of-plane component (see Fig. 2.2), an out-of-plane polarized tunneling current gives rise to a transverse voltage as well. When the spin Hall voltage is measured for in-plane and out-of-plane polarized currents, the densities of states and properties of the insulating barrier drop out in the quotient and a relation between the two spin components of the topological surface states can be obtained. So, if the in-plane polarization has been determined through other measurements like the method by Meservey and Tedrow (chapter 5), the out-of-plane polarization can be obtained.

6.1 Derivation

The derivation of the relation between in-plane and out-of-plane component is in many aspects analogous to calculations in chapter 5 and is therefore kept rather short.

When a voltage is applied between lead 1 and 3, electrons will tunnel into surface states of the TI and give rise to a tunneling current $I(U)$. Depending on the initial spin of a tunneling

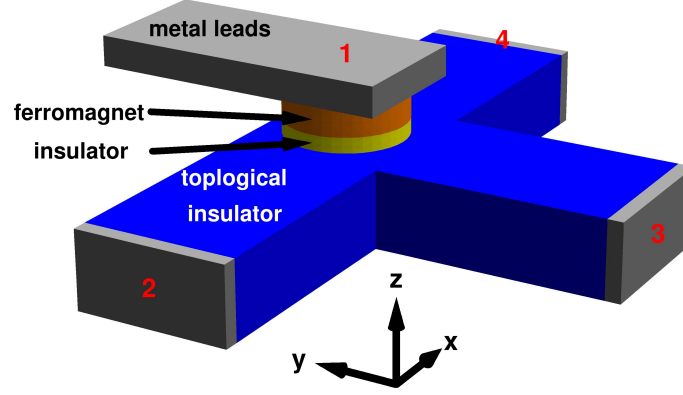


Figure 6.1: Schematic of the device structure for SHE tunneling spectroscopy as devised by Liu *et al.* [24]. An alternating current is applied between lead 1 and 3 to inject spin-polarized electrons into the surface states. Due to spin-momentum locking, this induces a voltage between lead 2 and 4.

electron, it will propagate either towards lead 2 or 4. A spin polarized current from a FM can lead to an asymmetry between electrons propagating into the two leads, and the resulting asymmetric charge accumulation therefore gives rise to a voltage V_{SH} between these leads. The change $\frac{dV_{\text{SH}}}{dI}$ of this voltage is thus proportional to the difference of the differential conductances (DC) $G(U) = \frac{dI(U)}{dU}$ of the tunnel junction with respect to the two leads. The absolute value of the Hall voltage V_{SH} depends on many aspects like device dimensions, properties of the insulating layer and spin and momentum relaxation processes. Here, however, only relative voltages for different magnetizations of the FM are of interest, and such effects, which are also strongly dependent on the device quality, are neglected.

Topological surface states are described by a simplified form of Eq. (5.39)

$$\bar{\psi}_{\pm}(p, \bar{q}, \varphi) = \frac{1}{2} \begin{pmatrix} \pm \sqrt{1 \pm \bar{q} \text{sign}(\cos 3\varphi)} \sqrt{1 + p} e^{-i(\varphi - \frac{\pi}{2})} \\ \sqrt{1 \mp \bar{q} \text{sign}(\cos 3\varphi)} \sqrt{1 + p} \\ \mp \sqrt{1 \pm \bar{q} \text{sign}(\cos 3\varphi)} \sqrt{1 - p} e^{-i(\varphi - \frac{\pi}{2})} \\ \sqrt{1 \mp \bar{q} \text{sign}(\cos 3\varphi)} \sqrt{1 - p} \end{pmatrix}, \quad (6.1)$$

where the out-of-plane spin $q_0(E) \cos 3\varphi$ is replaced by its mean value

$$\bar{q}(E) = \frac{3q_0(E)}{\pi} \int_{-\frac{\pi}{6}}^{\frac{\pi}{6}} d\varphi \cos 3\varphi \quad (6.2)$$

multiplied with the sign of its angular dependence. By this, all appearing integrals can be

solved analytically and the final formula is independent of the explicit angular dependence of the out-of-plane spin. As has been shown in section 5.1.1, tunneling currents depend only weakly on the measurement direction for tunneling electrons with in-plane polarization, and out-of-plane polarized tunneling electrons couple to the in-plane spin component independently of φ . So, the overall error due to this simplification should be small.

Eigenstates of the FM are modeled analog to those of the aluminum film in the previous chapter. For the beginning, only fully polarized eigenstates of the FM are considered. A finite polarization will be introduced later by assuming different densities of states for spin-up and spin-down states. The tunneling probability from ferromagnetic states with in-plane polarization (see Eq. (5.17))

$$\psi_{\varphi_F}^1(k_z, \varphi_F) = \frac{1}{\sqrt{2}} \sin k_z \begin{pmatrix} e^{-i\varphi_F} \\ 1 \\ 0 \\ 0 \end{pmatrix}, \quad \psi_{\varphi_F}^2(k_z, \varphi_F) = \frac{1}{\sqrt{2}} \sin k_z \begin{pmatrix} 0 \\ 0 \\ e^{-i\varphi_F} \\ 1 \end{pmatrix} \quad (6.3)$$

into the topological surface states is thus obtained by replacing $q \cos 3\varphi$ with $\bar{q} \text{sign}(\cos 3\varphi)$ and φ_{Al} with φ_F in Eq. (5.45)

$$|\langle \psi_{\varphi_F} | H_T | \bar{\psi}_{\pm} \rangle|^2 = \frac{1}{2} C_B^2 \sin^2 k_z(k) \left[1 \mp p \sqrt{1 - \bar{q}^2} \sin(\varphi_F - \varphi) \right]. \quad (6.4)$$

The momentum $k_z(k)$, orthogonal to the tunnel barrier, is given by Eq. (5.18) to assure energy and in-plane momentum conservation, and the transition matrix element of the insulating barrier is again chosen as $C_B = 1\text{eV}$ for numerical calculations. Analog to the construction of eigenstates with in-plane polarization (Eq. (5.17)), eigenstates with z -polarization can be constructed. In fact, the z -polarized states are already the four degenerate eigenstates. The two degenerate eigenstates with positive polarization are

$$\psi_{z+}^1(k_z) = \sin k_z \begin{pmatrix} 1 \\ 0 \\ 0 \\ 0 \end{pmatrix}, \quad \psi_{z+}^2(k_z) = \sin k_z \begin{pmatrix} 0 \\ 0 \\ 1 \\ 0 \end{pmatrix} \quad (6.5)$$

and those with negative polarization

$$\psi_{z-}^1(k_z) = \sin k_z \begin{pmatrix} 0 \\ 1 \\ 0 \\ 0 \end{pmatrix}, \quad \psi_{z-}^2(k_z) = \sin k_z \begin{pmatrix} 0 \\ 0 \\ 0 \\ 1 \end{pmatrix}. \quad (6.6)$$

6 Spin Hall effect tunneling spectroscopy

For FM states with positive z -polarization, the individual matrix elements

$$|\langle \psi_{z+}^1 | H_T | \bar{\psi}_{\pm} \rangle|^2 = \frac{1}{4} C_B^2 \sin^2 k_z(k) (1 \pm \bar{q} \text{sign}(\cos 3\varphi)) (1 + p), \quad (6.7)$$

$$|\langle \psi_{z+}^2 | H_T | \bar{\psi}_{\pm} \rangle|^2 = \frac{1}{4} C_B^2 \sin^2 k_z(k) (1 \pm \bar{q} \text{sign}(\cos 3\varphi)) (1 - p) \quad (6.8)$$

depend on the in-plane polarization p , which was introduced into the topological surface states as an asymmetry of the two orbitals with opposite in-plane spin. The sum of both matrix elements, however, is independent of p because the coupling to the in-plane spin does not depend on its sign

$$\begin{aligned} |\langle \psi_{z+} | H_T | \bar{\psi}_{\pm} \rangle|^2 &\equiv |\langle \psi_{z+}^1 | H_T | \bar{\psi}_{\pm} \rangle|^2 + |\langle \psi_{z+}^2 | H_T | \bar{\psi}_{\pm} \rangle|^2 \\ &= \frac{1}{2} C_B^2 \sin^2 k_z(k) (1 \pm \bar{q} \text{sign}(\cos 3\varphi)). \end{aligned} \quad (6.9)$$

Analogously for negative z -polarization

$$|\langle \psi_{z-} | H_T | \bar{\psi}_{\pm} \rangle|^2 = \frac{1}{2} C_B^2 \sin^2 k_z(k) (1 \mp \bar{q} \text{sign}(\cos 3\varphi)). \quad (6.10)$$

For an arbitrary ferromagnetic state ψ_F , the DC with respect to a direction defined by $f(\varphi)$ is

$$\begin{aligned} G(T, U) &= \frac{\text{const.}}{T} \int_0^{k_0} dk k \int_{-\pi}^{\pi} d\varphi \left(f(\varphi) \frac{|\langle \psi_F | H_T | \bar{\psi}_+ \rangle|^2}{\cosh^2\left(\frac{E_+ - U}{2k_B T}\right)} \right. \\ &\quad \left. + f(\varphi - \pi) \frac{|\langle \psi_F | H_T | \bar{\psi}_- \rangle|^2}{\cosh^2\left(\frac{E_- - U}{2k_B T}\right)} \right). \end{aligned} \quad (6.11)$$

After inserting the matrix elements, this expression can be rewritten as

$$G_F(T, U) = \frac{\text{const.}}{T} \int_0^{k_0} dk k \int_{-\pi}^{\pi} d\varphi (f(\varphi) g_+^F(\varphi) A_+(k) + f(\varphi - \pi) g_-^F(\varphi) A_-(k)). \quad (6.12)$$

Here, $A_{\pm}(k) = \frac{C_B^2 \sin^2 k_z(k)}{\cosh^2\left(\frac{E_{\pm} - U}{2k_B T}\right)}$ is equal for all ψ_F and $g_{\pm}^F(\varphi)$ contains the remaining parts that distinguish the different states. However, all states satisfy $g_-^F(\varphi + \pi) = g_+^F(\varphi)$. When the temperature is low and $\bar{q}(E)$ varies only slowly as a function of E , $\bar{q}(E)$ can be taken out of the integral, i.e. $\bar{q}(E) \approx \bar{q}(U)$. Then, under the assumption that $f(\varphi) = f(\varphi + 2\pi) = f(-\varphi)$,

Eq. (6.12) can be simplified to

$$\begin{aligned}
G_F(T, U) &= \frac{\text{const.}}{T} \int_0^{k_0} dk k \int_{-\pi}^{\pi} d\varphi f(\varphi) (g_+^F(\varphi) A_+(k) + g_-^F(\varphi + \pi) A_-(k)) \\
&= \frac{\text{const.}}{T} \int_0^{k_0} dk k (A_+(k) + A_-(k)) \int_{-\pi}^{\pi} d\varphi f(\varphi) g_+^F(\varphi) \\
&= G_0(T, U) \int_{-\pi}^{\pi} d\varphi f(\varphi) g_+^F(\varphi). \tag{6.13}
\end{aligned}$$

For mirror symmetry of the device with respect to the y - z -plane, the geometrical function for the other lead is given by $f'(\varphi) = f(\varphi + \pi)$, and consequently, the difference of the DCs can be written as

$$\Delta G_F(T, U) = G_0(T, U) \int_{-\pi}^{\pi} d\varphi f(\varphi) (g_+^F(\varphi) - g_-^F(\varphi)). \tag{6.14}$$

In the device structure shown in Fig. 6.1, all electrons initially moving in positive direction end up in the corresponding lead so that (compare Eq. (5.10))

$$f(\varphi) = \begin{cases} 1 & \text{for } \varphi \in [-\frac{\pi}{2}, \frac{\pi}{2}] \\ 0 & \text{else.} \end{cases} \tag{6.15}$$

Considering now the concrete matrix elements in Eq. (6.4), (6.9) and (6.10) the resulting ΔG for a fully polarized FM can be easily calculated and are given by

$$\Delta G_{\varphi_F}(T, U, \varphi_F) = G_0(T, U) 2p\sqrt{1 - \bar{q}^2(U)} \sin \varphi_F \tag{6.16}$$

and

$$\Delta G_{z\pm}(T, U) = \pm G_0(T, U) \frac{\pi}{3} \bar{q}(U). \tag{6.17}$$

In the case of a finite polarization of the FM, the total DC differences ΔG between the two leads are given by a weighted sum of terms with opposite FM polarization. So, for an in-plane polarized FM

$$\Delta G_{\text{ip}}(T, U, \varphi_F) = G_0(T, U) 2p\sqrt{1 - \bar{q}^2(U)} \sin \varphi_F \Delta n_{\text{ip}} \tag{6.18}$$

is obtained, where the direction of the in-plane polarization φ_F has to be adjusted to the polarization of surface states with propagation direction along the x -axis, i.e. in this case $\varphi_F = \frac{\pi}{2}$. For a FM with out-of-plane polarization

$$\Delta G_{\text{op}}(T, U) = G_0(T, U) \frac{\pi}{3} \bar{q}(U) \Delta n_{\text{op}} \tag{6.19}$$

is obtained. Here, $\Delta n = n_+ - n_-$, with $n_+ + n_- = 1$, is the relative density of states of spin-up and spin-down states, and the indices ip and op stand for in-plane and out-of-plane polarization of the FM, respectively. The quotient of Eq. (6.18) and (6.19) can be solved for

6 Spin Hall effect tunneling spectroscopy

the out-of-plane polarization $\bar{q}(U)$ and is independent of G_0 :

$$\bar{q}(U) = \sqrt{\frac{1}{1 + \left(\frac{\Delta G_{\text{ip}}}{\Delta G_{\text{op}}} \frac{\Delta n_{\text{op}}}{\Delta n_{\text{ip}}} \frac{\pi}{6p \sin \varphi_F} \right)^2}}. \quad (6.20)$$

So, if the anisotropy of the FM and the in-plane polarization of the TI are known, the mean out-of-plane polarization of the TI can be determined by measuring ΔG_{ip} and ΔG_{op} .

Assuming that the approximation

$$q(E, \varphi) = \pm q_0(E) \cos 3\varphi \quad (6.21)$$

for the out-of-plane polarization is good (\pm is for the upper and lower Dirac cone, respectively), $q(E, \varphi)$ can be calculated from \bar{q} by

$$q(E, \varphi) = \pm \bar{q}(E) \frac{\pi}{3} \frac{\cos 3\varphi}{\int_{-\pi/6}^{\pi/6} d\varphi' \cos 3\varphi'} = \pm \bar{q}(E) \frac{\pi}{2} \cos 3\varphi. \quad (6.22)$$

However, since only the alternating sign of $\cos 3\varphi$ was used in the derivation of Eq. (6.20), a different angular dependence can be assumed as well. In theory, the angular dependence could even be determined from how ΔG_{op} changes when the TI crystal is rotated with respect to the device structure.

6.2 Numerical test

In this section, the validity of Eq. (6.20) and (6.22) will be tested by comparison with numerical calculations. For that purpose, ΔG_{ip} and ΔG_{op} are calculated with numerically exact eigenvectors of the full Hamiltonian Eq. (3.20), analog to section 5.1. Because the numerical eigenstates are only given for discrete momenta, the integrals in Eq. (6.11) have to be replaced by a sum over all numerical TI eigenstates and analytical FM eigenstates that fulfill energy and in-plane momentum conservation. The TI eigenvectors are calculated by exact numerical diagonalization for 50 (Bi_2Se_3) or 200 (Sb_2Te_3) real space lattice sites in z -direction and a hexagonal in-plane momentum discretization of $\frac{2}{\sqrt{3}} \frac{2\pi}{2000}$. Their propagation direction is determined from a difference quotient, i.e. from changes of the corresponding eigenvalues for small variations of the in-plane momenta k_x and k_y . Figure 6.2 shows the resulting ΔG curves for two different parameter sets (Bi_2Se_3 (a) and Sb_2Te_3) and energy values inside the corresponding bulk gaps. For simplicity, the tunneling currents are assumed to be fully polarized in either y - or z -direction. A reduced polarization would only scale the whole curves to lower values. At low temperature (10K), ΔG_{ip} is nearly zero at the Dirac point and in its vicinity increases about linearly to either side. Decreases at the gap edges can be mostly attributed to increased decay lengths of the surface states as they merge into the bulk states.

ΔG_{op} has a wider minimum at the Dirac point and then increases strongly towards the gap edges because out-of-plane polarization and density of states increase at the same time. As the mean out-of-plane polarization is smaller than the in-plane polarization and the contribu-

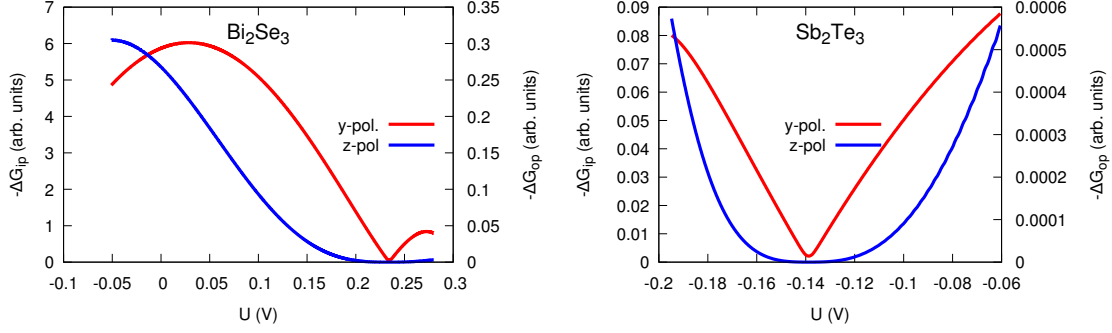


Figure 6.2: Numerical DC differences ΔG at 10K inside the bulk gap for y - and z -polarization of the FM. ΔG_{ip} shows a clear kink at the Dirac point, while ΔG_{op} has a wider minimum. For both materials, ΔG_{ip} is about two orders of magnitude larger than ΔG_{op} . The overall smaller values for Sb_2Te_3 result from weaker localized surface states and a lower density of states.

tions of two-thirds of the surface states compensate each other for an out-of-plane polarized tunneling current, ΔG_{op} is about two orders of magnitude smaller than ΔG_{ip} . However, the shown absolute values are of no physical meaning because they largely depend on device properties like size, material and thickness of the tunneling contact and other material properties like spin and momentum decay lengths. The absolute values for Sb_2Te_3 are overall smaller because the surface states reach deeper into the bulk and therefore have smaller absolute values at the surface. Besides, the density of states is somewhat smaller.

As a next step, the mean out-of-plane polarization is calculated from these curves, with parameters $p = \Delta n_{ip} = \Delta n_{op} = 1$ and $\varphi_F = \frac{\pi}{2}$, and is then compared to the energy dependent mean value $\bar{q}_{ana}(E)$ of the analytical z -polarization $p_z(k_x, k_y)$ (Eq. (3.41)). To calculate the mean value of the analytical polarization, k_x and k_y are expressed in polar coordinates, where the momentum k is calculated numerically by solving the dispersion $E_{\pm}(k \cos \varphi, k \sin \varphi)$ (Eq. (3.37)) for k for a given E and φ . Then, $\bar{q}_{ana}(E)$ can be obtained by numerically calculating

$$\bar{q}_{ana}(E) = \frac{\int_0^{\pi/3} d\varphi k(E, \varphi) |p_z(k(E, \varphi) \cos \varphi, k(E, \varphi) \sin \varphi)|}{\int_0^{\pi/3} d\varphi k(E, \varphi)}. \quad (6.23)$$

Both operations, solving the dispersion for k and calculating the integrals, are performed using build-in functions of *Mathematica*. As can be seen in Fig. 6.3, $\bar{q}(E)$ and $\bar{q}_{ana}(E)$ coincide very well. Only for Bi_2Se_3 , $\bar{q}(E)$ slightly exceeds the analytical value for low energies, i.e. where $\bar{q}(E)$ becomes larger. The reason for this deviation is the replacement of $q \cos 3\varphi$ by its mean value in Eq. (6.1). This leads to a changed angular dependent weighting of the matrix elements for tunneling from a FM with in-plane polarization and thereby causes a slight overestimate of ΔG_{ip} in Eq. (6.20). Consequently, the smaller numerical value for ΔG_{ip} results in an overestimate of $\bar{q}(E)$.

A comparison of the angular dependent analytical polarization along a constant energy contour E , i.e. $p_z(k(E, \varphi) \cos \varphi, k(E, \varphi) \sin \varphi)$, and Eq. (6.21) is shown in Fig. 6.4 for three

6 Spin Hall effect tunneling spectroscopy

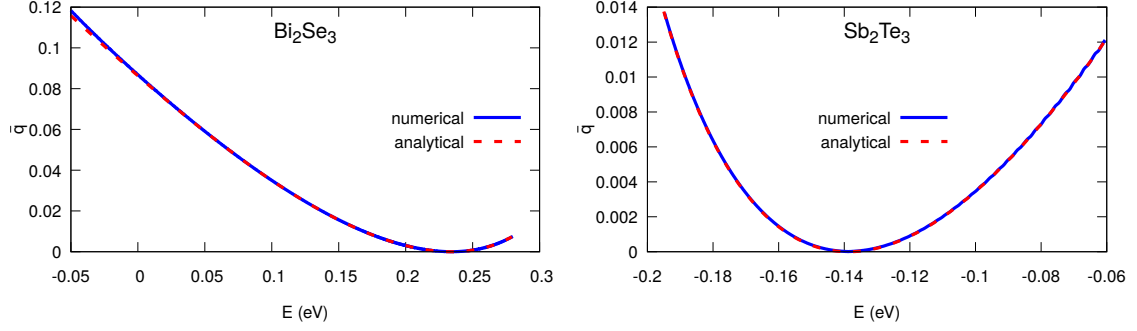


Figure 6.3: Comparison of the mean polarization $\bar{q}(E)$, obtained from the numerical DCs, and the energy dependent mean value $\bar{q}_{\text{ana}}(E)$ of the analytical out-of-plane polarization. A small deviation is only visible for Bi_2Se_3 towards the lower edge of the bulk gap. For higher energies and for Sb_2Te_3 , no notable deviations exists.

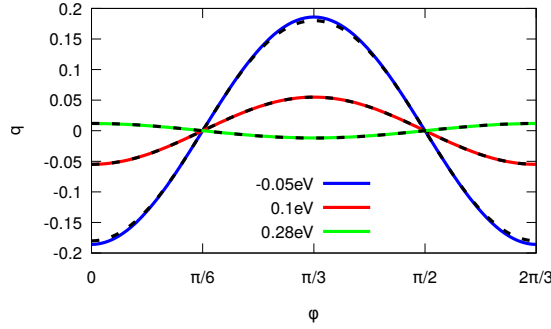


Figure 6.4: Comparison of Eq. (6.21) (solid colored lines) and the analytical polarization $p_z(k(E, \varphi) \cos \varphi, k(E, \varphi) \sin \varphi)$ (black dashed lines) for three different energies throughout the bulk gap. Apart from a small scaling factor of the amplitude, the curves coincide very well.

different energies. Apart from small amplitude deviations, coming from the overestimate of $\bar{q}(E)$, the two curves are in very good agreement and therefore justify the approximation of TI surface states in Eq. (5.39). When p and q_0 are determined from the spin expectation values of the numerical eigenstates, the maximal deviations between Eq. (3.39)-(3.41) and Eq. (5.40)-(5.42) for Bi_2Se_3 are only $\max |p_z - p'_z| \sim 2 \cdot 10^{-3}$ and $\max |p_{x/y} - p'_{x/y}| \sim 3 \cdot 10^{-4}$ at the lower edge of the bulk gap and get smaller towards the Dirac point.

6.3 Summary

Due to the locking of spin and momentum in topological surface states, a spin polarized current which is injected into the surface of a TI results in a directional surface current. When metallic

6.3 Summary

contacts are connected to opposite sides of the TI, this gives rise to a measurable voltage between these contacts. In this chapter, it has now been shown that, by measuring these voltages for tunneling currents with in-plane and out-of-plane polarization, a relation between in-plane and out-of-plane spin polarization of the topological surface states can be given. Especially, when the in-plane spin is known from other measurements, the out-of-plane spin can be derived by a simple formula.

7 Summary and conclusion

TIs are rather new materials with great potential for applications in spintronic devices and are therefore studied intensively in current research. The first topic of this thesis was about electronic transport in edge state channels of 2D TIs with local FEFs and the possibility to create pure spin current devices from such structures. The electronic transport was studied by quantum transport calculations on a lattice. Wave packets, constructed from topological edge states, were placed in lead positions of the investigated structure and then their propagation through the device structure was studied by numerically applying the time-evolution operator. As the wave packet contains a broad energy range, the energy dependent scattering probabilities into defined exit channels could be calculated for the whole TI bulk gap in a single calculational run from the time-dependent overlap with wave packets placed along the exit channels. Non-equilibrium densities of state, which show the paths electrons can take between different leads, were obtained from integrating the propagating wave packet during the time-evolution. The tight-binding character of the Hamiltonian describing materials of the Bi_2Se_3 class allowed an efficient implementation of the transport code on a GPU device using *CUDA* with favorable computation times even for relatively large systems.

Transport calculations for TI sheets described by a 2D Hamiltonian showed that local FEFs perpendicular to the surface plane locally cause a quantum phase transition into a QAH state. In the presence of the FEF, one of the two spin polarized edge state channels is removed from the TI-vacuum interface and shifted to the inner edge of the FEF. Reversing the FEF interchanges the two channels. Even though FEFs generally break time-reversal symmetry, fields perpendicular to the surface do not cause spin-flip scattering. FEFs with polarization parallel to the surface, on the other hand, open a gap in the edge state dispersion and cause scattering processes that can reverse the spin and propagation direction of electrons in edge state channels.

By combining multiple local FEFs with positive and negative polarization perpendicular to the surface, devices were conceived that can create, switch and detect pure spin currents. A pure spin current arises when spin polarized currents of equal magnitude are driven in opposite directions along the edge so that the charge currents compensate each other while the spin transport remains. As these devices directly convert charge currents into pure spin currents, they can be much more power efficient than other state of the art methods like the spin Hall effect. To measure the pure spin currents, they are simply split back into the two counter propagating charge currents.

An experimental realization of the proposed devices with state of the art materials can be challenging but should be possible. The QAH effect has been measured in thin films of V-doped $(\text{Sb,Bi})_2\text{Te}_3$, however only at very low temperatures because the magnetic excitation gap in the edge state dispersion and the Curie temperature are relatively small. The challenge in devices where the QAH effect is locally induced by chemical doping is then to tune the Fermi

7 Summary and conclusion

level into the gap for all device parts. Introducing the FEF by proximity to a ferromagnetic insulator may be the more promising alternative because no dopants are introduced into the TI and the Curie temperature is higher. However, so far no QAH effect has been measured in such systems. To achieve room temperature applicability, other 2D TIs with larger bulk gaps of about 0.3eV have to be used and the magnetic excitation gap and Curie temperature have to be strongly enhanced to the same level.

Quantum transport calculations based on the 3D Hamiltonian showed that the pure spin currents should remain very robust in the presence of certain perturbations because spin-up and spin-down currents are scattered equally. Small distortions of the pure spin current can only arise when the number of scattering sites is different for spin-up and spin-down currents. Assuming no random time-reversal symmetry breaking perturbations, this can only be the case for the transistor in the “off”-state, where the counter propagating currents are reflected by two consecutive magnetic domains. In that specific case, a broken structural inversion symmetry or an in-plane field component can result in a small residual charge current where no current should flow at all. Careful device engineering may resolve even this potential problem.

As a second topic, quantum tunneling from thin superconducting aluminum films into topological surface states was investigated as a method for measuring the surface state spin polarization. Knowledge about the spin polarization is essential for the efficiency of many TI based spintronic applications. This method, which was first applied to ferromagnetic materials by Meservey and Tedrow, relies on the splitting of the BCS density of states in a strong parallel magnetic field into a spin-up and a spin-down part. As the spin of electrons tunneling from the aluminum film into the ferromagnet is conserved, the polarization of the ferromagnet can be calculated from the relative height of four peaks in the tunneling spectrum.

TIs have no net polarization, but spin and propagation direction of electrons in surface states are locked. A mean value for the surface state polarization can therefore be obtained from measuring only tunneling electrons that flow off in a defined direction in the surface of the TI. Starting from an analytical approximation of aluminum states and TI surface states that neglects the out-of-plane spin component, a modified polarization formula, analogous to the one by Meservey and Tedrow, was derived. This formula takes into account the spin-momentum locking of surface states as well as the device geometry. The main difference between the two formulas is then a factor γ that has to be calculated from a function describing the angular dependent probability for a surface electron to reach a certain electrode on the surface. This function can also include effects like spin-flip scattering and, by solving the polarization formula for γ , the spin-flip mean free path can be measured as well, even if the polarization is unknown. Application of the polarization formula to tunneling spectra obtained from numerically exact eigenstates of the full 3D Hamiltonian showed that this method is largely insensitive to the out-of-plane spin component of the topological surface states. Essentially, only the polarization of the in-plane component is measured.

To obtain the out-of-plane component, another method was investigated that involves tunneling from a ferromagnet, which can have polarizations parallel and perpendicular to the surface of the TI. Due to the locking of spin and propagation direction, a polarized current injected into the surface of a TI will flow off mainly in one direction. When two metallic electrodes

are attached on opposite sides of the TI, this leads to a measurable voltage between the two electrodes. Such a voltage has already been measured in experiments for a ferromagnet with in-plane polarization.

The difference in differential conductances with respect to the two electrodes, which is proportional to the measurable voltage, was again calculated from analytical approximations of ferromagnetic states and topological surface states, now including a mean out-of-plane spin component. When this difference is measured for parallel and perpendicular polarizations of the ferromagnet, all unknown material properties should drop out in the quotient. The analytical expression of this quotient was then solved for the mean out-of-plane spin, where the only additional parameters are the polarization anisotropy of the ferromagnet and the in-plane spin polarization of the topological surface states. By applying a model for the out-of-plane spin, the angular dependence can be calculated from the mean value. A comparison of the mean polarization, obtained from calculating the differential conductance differences from numerically exact TI eigenstates of the full Hamiltonian, with the correct analytical values showed good agreement. Only when the mean out-of-plane component reaches values of the order of 10%, the polarization formula slightly overestimates the polarization.

Bibliography

- [1] M. Götze, M. Joppe, and T. Dahm, “Pure spin current devices based on ferromagnetic topological insulators,” *Scientific Reports* **6**, 36070 (2016).
- [2] M. Götze, T. Paananen, G. Reiss, and T. Dahm, “Tunneling Magnetoresistance Devices Based on Topological Insulators: Ferromagnet–Insulator–Topological-Insulator Junctions Employing Bi_2Se_3 ,” *Phys. Rev. Applied* **2**, 054010 (2014).
- [3] S. A. Wolf, D. D. Awschalom, R. A. Buhrman, J. M. Daughton, S. von Molnár, M. L. Roukes, A. Y. Chtchelkanova, and D. M. Treger, “Spintronics: A Spin-Based Electronics Vision for the Future,” *Science* **294**, 1488 (2001).
- [4] I. Žutić, J. Fabian, and S. Das Sarma, “Spintronics: Fundamentals and applications,” *Rev. Mod. Phys.* **76**, 323 (2004).
- [5] S. D. Bader and S. S. P. Parkin, “Spintronics,” *Annual Review of Condensed Matter Physics* **1**, 71 (2010).
- [6] H. Liu, D. Bedau, D. Backes, J. A. Katine, J. Langer, and A. D. Kent, “Ultrafast switching in magnetic tunnel junction based orthogonal spin transfer devices,” *Applied Physics Letters* **97**, 242510 (2010).
- [7] T. Fujita, M. B. A. Jalil, and S. G. Tan, “Topological Insulator Cell for Memory and Magnetic Sensor Applications,” *Applied Physics Express* **4**, 094201 (2011).
- [8] V. Krueckl and K. Richter, “Switching Spin and Charge between Edge States in Topological Insulator Constrictions,” *Phys. Rev. Lett.* **107**, 086803 (2011).
- [9] D. Pesin and A. H. MacDonald, “Spintronics and pseudospintronics in graphene and topological insulators,” *Nat Mater* **11**, 409 (2012).
- [10] A. R. Mellnik, J. S. Lee, A. Richardella, J. L. Grab, P. J. Mintun, M. H. Fischer, A. Vaezi, A. Manchon, E.-A. Kim, N. Samarth, and D. C. Ralph, “Spin-transfer torque generated by a topological insulator,” *Nature* **511**, 449 (2014).
- [11] Y. Shiomi, K. Nomura, Y. Kajiwara, K. Eto, M. Novak, K. Segawa, Y. Ando, and E. Saitoh, “Spin-Electricity Conversion Induced by Spin Injection into Topological Insulators,” *Phys. Rev. Lett.* **113**, 196601 (2014).
- [12] U. Roy, R. Dey, T. Pramanik, B. Ghosh, L. F. Register, and S. K. Banerjee, “Magnetization switching of a metallic nanomagnet via current-induced surface spin-polarization of an underlying topological insulator,” *Journal of Applied Physics* **117**, 163906 (2015).

Bibliography

- [13] B. Scharf, A. Matos-Abiague, J. E. Han, E. M. Hankiewicz, and I. Žutić, “Tunneling Planar Hall Effect in Topological Insulators: Spin Valves and Amplifiers,” *Phys. Rev. Lett.* **117**, 166806 (2016).
- [14] F. Ronetti, L. Vannucci, G. Dolcetto, M. Carrega, and M. Sasseti, “Spin-thermoelectric transport induced by interactions and spin-flip processes in two-dimensional topological insulators,” *Phys. Rev. B* **93**, 165414 (2016).
- [15] B. A. Bernevig, T. L. Hughes, and S.-C. Zhang, “Quantum Spin Hall Effect and Topological Phase Transition in HgTe Quantum Wells,” *Science* **314**, 1757 (2006).
- [16] L. Fu, C. L. Kane, and E. J. Mele, “Topological Insulators in Three Dimensions,” *Phys. Rev. Lett.* **98**, 106803 (2007).
- [17] M. Z. Hasan and C. L. Kane, “*Colloquium* : Topological insulators,” *Rev. Mod. Phys.* **82**, 3045 (2010).
- [18] C.-X. Liu, X.-L. Qi, X. Dai, Z. Fang, and S.-C. Zhang, “Quantum Anomalous Hall Effect in $\text{Hg}_{1-y}\text{Mn}_y\text{Te}$ Quantum Wells,” *Phys. Rev. Lett.* **101**, 146802 (2008).
- [19] R. Yu, W. Zhang, H.-J. Zhang, S.-C. Zhang, X. Dai, and Z. Fang, “Quantized Anomalous Hall Effect in Magnetic Topological Insulators,” *Science* **329**, 61 (2010).
- [20] C.-Z. Chang, J. Zhang, X. Feng, J. Shen, Z. Zhang, M. Guo, K. Li, Y. Ou, P. Wei, L.-L. Wang, Z.-Q. Ji, Y. Feng, S. Ji, X. Chen, J. Jia, X. Dai, Z. Fang, S.-C. Zhang, K. He, Y. Wang, L. Lu, X.-C. Ma, and Q.-K. Xue, “Experimental Observation of the Quantum Anomalous Hall Effect in a Magnetic Topological Insulator,” *Science* **340**, 167 (2013).
- [21] P. M. Tedrow and R. Meservey, “Spin-Dependent Tunneling into Ferromagnetic Nickel,” *Phys. Rev. Lett.* **26**, 192 (1971).
- [22] P. M. Tedrow and R. Meservey, “Spin Polarization of Electrons Tunneling from Films of Fe, Co, Ni, and Gd,” *Phys. Rev. B* **7**, 318 (1973).
- [23] L. Liu, C.-T. Chen, and J. Z. Sun, “Spin Hall effect tunnelling spectroscopy,” *Nat Phys* **10**, 561 (2014).
- [24] L. Liu, A. Richardella, I. Garate, Y. Zhu, N. Samarth, and C.-T. Chen, “Spin-polarized tunneling study of spin-momentum locking in topological insulators,” *Phys. Rev. B* **91**, 235437 (2015).
- [25] X.-L. Qi and S.-C. Zhang, “Topological insulators and superconductors,” *Rev. Mod. Phys.* **83**, 1057 (2011).
- [26] M. König, S. Wiedmann, C. Brüne, A. Roth, H. Buhmann, L. W. Molenkamp, X.-L. Qi, and S.-C. Zhang, “Quantum Spin Hall Insulator State in HgTe Quantum Wells,” *Science* **318**, 766 (2007).

- [27] K. v. Klitzing, G. Dorda, and M. Pepper, "New Method for High-Accuracy Determination of the Fine-Structure Constant Based on Quantized Hall Resistance," *Phys. Rev. Lett.* **45**, 494 (1980).
- [28] X.-L. Qi and S.-C. Zhang, "The quantum spin Hall effect and topological insulators," *Physics Today* **63**, 33 (2009).
- [29] M. König, H. Buhmann, L. W. Molenkamp, T. Hughes, C.-X. Liu, X.-L. Qi, and S.-C. Zhang, "The Quantum Spin Hall Effect: Theory and Experiment," *Journal of the Physical Society of Japan* **77**, 031007 (2008).
- [30] J. E. Moore, "The birth of topological insulators," *Nature* **464**, 194 (2010).
- [31] L. Fu and C. L. Kane, "Topological insulators with inversion symmetry," *Phys. Rev. B* **76**, 045302 (2007).
- [32] H. Zhang, C.-X. Liu, X.-L. Qi, X. Dai, Z. Fang, and S.-C. Zhang, "Topological insulators in Bi₂Se₃, Bi₂Te₃ and Sb₂Te₃ with a single Dirac cone on the surface," *Nat Phys* **5**, 438 (2009).
- [33] D. Hsieh, D. Qian, L. Wray, Y. Xia, Y. S. Hor, R. J. Cava, and M. Z. Hasan, "A topological Dirac insulator in a quantum spin Hall phase," *Nature* **452**, 970 (2008).
- [34] Y. Xia, D. Qian, D. Hsieh, L. Wray, A. Pal, H. Lin, A. Bansil, D. Grauer, Y. S. Hor, R. J. Cava, and M. Z. Hasan, "Observation of a large-gap topological-insulator class with a single Dirac cone on the surface," *Nat Phys* **5**, 398 (2009).
- [35] Y. L. Chen, J. G. Analytis, J.-H. Chu, Z. K. Liu, S.-K. Mo, X. L. Qi, H. J. Zhang, D. H. Lu, X. Dai, Z. Fang, S. C. Zhang, I. R. Fisher, Z. Hussain, and Z.-X. Shen, "Experimental Realization of a Three-Dimensional Topological Insulator, Bi₂Te₃," *Science* **325**, 178 (2009).
- [36] D. Hsieh, Y. Xia, D. Qian, L. Wray, F. Meier, J. H. Dil, J. Osterwalder, L. Patthey, A. V. Fedorov, H. Lin, A. Bansil, D. Grauer, Y. S. Hor, R. J. Cava, and M. Z. Hasan, "Observation of Time-Reversal-Protected Single-Dirac-Cone Topological-Insulator States in Bi₂Te₃ and Sb₂Te₃," *Phys. Rev. Lett.* **103**, 146401 (2009).
- [37] G. Wang, X. Zhu, J. Wen, X. Chen, K. He, L. Wang, X. Ma, Y. Liu, X. Dai, Z. Fang, J. Jia, and Q. Xue, "Atomically smooth ultrathin films of topological insulator Sb₂Te₃," *Nano Research* **3**, 874 (2010).
- [38] Z.-H. Pan, E. Vescovo, A. V. Fedorov, D. Gardner, Y. S. Lee, S. Chu, G. D. Gu, and T. Valla, "Electronic Structure of the Topological Insulator Bi₂Se₃ Using Angle-Resolved Photoemission Spectroscopy: Evidence for a Nearly Full Surface Spin Polarization," *Phys. Rev. Lett.* **106**, 257004 (2011).

Bibliography

- [39] C. Jozwiak, Y. L. Chen, A. V. Fedorov, J. G. Analytis, C. R. Rotundu, A. K. Schmid, J. D. Denlinger, Y.-D. Chuang, D.-H. Lee, I. R. Fisher, R. J. Birgeneau, Z.-X. Shen, Z. Hussain, and A. Lanzara, "Widespread spin polarization effects in photoemission from topological insulators," *Phys. Rev. B* **84**, 165113 (2011).
- [40] S. Souma, K. Kosaka, T. Sato, M. Komatsu, A. Takayama, T. Takahashi, M. Kriener, K. Segawa, and Y. Ando, "Direct Measurement of the Out-of-Plane Spin Texture in the Dirac-Cone Surface State of a Topological Insulator," *Phys. Rev. Lett.* **106**, 216803 (2011).
- [41] A. Herdt, L. Plucinski, G. Bihlmayer, G. Mussler, S. Döring, J. Krumrain, D. Grützmacher, S. Blügel, and C. M. Schneider, "Spin-polarization limit in Bi_2Te_3 Dirac cone studied by angle- and spin-resolved photoemission experiments and *ab initio* calculations," *Phys. Rev. B* **87**, 035127 (2013).
- [42] J. Sánchez-Barriga, A. Varykhalov, J. Braun, S.-Y. Xu, N. Alidoust, O. Kornilov, J. Minár, K. Hummer, G. Springholz, G. Bauer, R. Schumann, L. V. Yashina, H. Ebert, M. Z. Hasan, and O. Rader, "Photoemission of Bi_2Se_3 with Circularly Polarized Light: Probe of Spin Polarization or Means for Spin Manipulation?" *Phys. Rev. X* **4**, 011046 (2014).
- [43] G. Landolt, S. Schreyeck, S. V. Ereameev, B. Slomski, S. Muff, J. Osterwalder, E. V. Chulkov, C. Gould, G. Karczewski, K. Brunner, H. Buhmann, L. W. Molenkamp, and J. H. Dil, "Spin Texture of Bi_2Se_3 Thin Films in the Quantum Tunneling Limit," *Phys. Rev. Lett.* **112**, 057601 (2014).
- [44] C.-X. Liu, X.-L. Qi, H. Zhang, X. Dai, Z. Fang, and S.-C. Zhang, "Model Hamiltonian for topological insulators," *Phys. Rev. B* **82**, 045122 (2010).
- [45] G. Zhang, H. Qin, J. Teng, J. Guo, Q. Guo, X. Dai, Z. Fang, and K. Wu, "Quintuple-layer epitaxy of thin films of topological insulator Bi_2Se_3 ," *Applied Physics Letters* **95**, 053114 (2009).
- [46] Y. Zhang, K. He, C.-Z. Chang, C.-L. Song, L.-L. Wang, X. Chen, J.-F. Jia, Z. Fang, X. Dai, W.-Y. Shan, S.-Q. Shen, Q. Niu, X.-L. Qi, S.-C. Zhang, X.-C. Ma, and Q.-K. Xue, "Crossover of the three-dimensional topological insulator Bi_2Se_3 to the two-dimensional limit," *Nat Phys* **6**, 584 (2010).
- [47] J. Linder, T. Yokoyama, and A. Sudbø, "Anomalous finite size effects on surface states in the topological insulator Bi_2Se_3 ," *Phys. Rev. B* **80**, 205401 (2009).
- [48] C.-X. Liu, H. Zhang, B. Yan, X.-L. Qi, T. Frauenheim, X. Dai, Z. Fang, and S.-C. Zhang, "Oscillatory crossover from two-dimensional to three-dimensional topological insulators," *Phys. Rev. B* **81**, 041307 (2010).
- [49] H.-Z. Lu, W.-Y. Shan, W. Yao, Q. Niu, and S.-Q. Shen, "Massive Dirac fermions and spin physics in an ultrathin film of topological insulator," *Phys. Rev. B* **81**, 115407 (2010).

- [50] W. Luo and H. Xiang, "Room Temperature Quantum Spin Hall Insulators with a Buckled Square Lattice," *Nano Letters* **15**, 3230 (2015), pMID: 25822125.
- [51] C. Pauly, B. Rasche, K. Koepf, M. Liebmann, M. Pratzner, M. Richter, J. Kellner, M. Eschbach, B. Kaufmann, L. Plucinski, C. M. Schneider, M. Ruck, J. van den Brink, and M. Morgenstern, "Subnanometre-wide electron channels protected by topology," *Nat Phys* **11**, 338 (2015).
- [52] Y. L. Chen, J.-H. Chu, J. G. Analytis, Z. K. Liu, K. Igarashi, H.-H. Kuo, X. L. Qi, S. K. Mo, R. G. Moore, D. H. Lu, M. Hashimoto, T. Sasagawa, S. C. Zhang, I. R. Fisher, Z. Hussain, and Z. X. Shen, "Massive Dirac Fermion on the Surface of a Magnetically Doped Topological Insulator," *Science* **329**, 659 (2010).
- [53] T. Paananen and T. Dahm, "Magnetically robust topological edge states and flat bands," *Phys. Rev. B* **87**, 195447 (2013).
- [54] T. Paananen, H. Gerber, M. Götze, and T. Dahm, "Appearance of flat surface bands in three-dimensional topological insulators in a ferromagnetic exchange field," *New Journal of Physics* **16**, 033019 (2014).
- [55] X.-L. Qi, Y.-S. Wu, and S.-C. Zhang, "Topological quantization of the spin Hall effect in two-dimensional paramagnetic semiconductors," *Phys. Rev. B* **74**, 085308 (2006).
- [56] C.-Z. Chang, W. Zhao, D. Y. Kim, H. Zhang, B. A. Assaf, D. Heiman, S.-C. Zhang, C. Liu, M. H. W. Chan, and J. S. Moodera, "High-precision realization of robust quantum anomalous Hall state in a hard ferromagnetic topological insulator," *Nat Mater* **14**, 473 (2015).
- [57] C.-Z. Chang, W. Zhao, D. Y. Kim, P. Wei, J. K. Jain, C. Liu, M. H. W. Chan, and J. S. Moodera, "Zero-Field Dissipationless Chiral Edge Transport and the Nature of Dissipation in the Quantum Anomalous Hall State," *Phys. Rev. Lett.* **115**, 057206 (2015).
- [58] W. Li, M. Claassen, C.-Z. Chang, B. Moritz, T. Jia, C. Zhang, S. Rebec, J. J. Lee, M. Hashimoto, D.-H. Lu, R. G. Moore, J. S. Moodera, T. P. Devereaux, and Z.-X. Shen, "Origin of the low critical observing temperature of the quantum anomalous Hall effect in V-doped (Bi, Sb)₂Te₃ film," *Scientific Reports* **6**, 32732 (2016).
- [59] S. Qi, Z. Qiao, X. Deng, E. D. Cubuk, H. Chen, W. Zhu, E. Kaxiras, S. B. Zhang, X. Xu, and Z. Zhang, "High-Temperature Quantum Anomalous Hall Effect in $n-p$ Codoped Topological Insulators," *Phys. Rev. Lett.* **117**, 056804 (2016).
- [60] P. Wei, F. Katmis, B. A. Assaf, H. Steinberg, P. Jarillo-Herrero, D. Heiman, and J. S. Moodera, "Exchange-Coupling-Induced Symmetry Breaking in Topological Insulators," *Phys. Rev. Lett.* **110**, 186807 (2013).
- [61] M. Li, C.-Z. Chang, B. J. Kirby, M. E. Jamer, W. Cui, L. Wu, P. Wei, Y. Zhu, D. Heiman, J. Li, and J. S. Moodera, "Proximity-Driven Enhanced Magnetic Order

Bibliography

- at Ferromagnetic-Insulator–Magnetic-Topological-Insulator Interface,” *Phys. Rev. Lett.* **115**, 087201 (2015).
- [62] F. Katmis, V. Lauter, F. S. Nogueira, B. A. Assaf, M. E. Jamer, P. Wei, B. Satpati, J. W. Freeland, I. Eremin, D. Heiman, P. Jarillo-Herrero, and J. S. Moodera, “A high-temperature ferromagnetic topological insulating phase by proximity coupling,” *Nature* **533**, 513 (2016).
- [63] M. König, M. Baenninger, A. G. F. Garcia, N. Harjee, B. L. Pruitt, C. Ames, P. Leubner, C. Brüne, H. Buhmann, L. W. Molenkamp, and D. Goldhaber-Gordon, “Spatially Resolved Study of Backscattering in the Quantum Spin Hall State,” *Phys. Rev. X* **3**, 021003 (2013).
- [64] K. Taguchi, T. Yokoyama, and Y. Tanaka, “Giant magnetoresistance in the junction of two ferromagnets on the surface of diffusive topological insulators,” *Phys. Rev. B* **89**, 085407 (2014).
- [65] S. Majumder, S. Guchhait, R. Dey, L. F. Register, and S. K. Banerjee, “Large Magnetoresistance at Room Temperature in Ferromagnet/Topological Insulator Contacts,” *IEEE Transactions on Nanotechnology* **15**, 671 (2016).
- [66] A. Hoffmann, “Spin Hall Effects in Metals,” *IEEE Transactions on Magnetism* **49**, 5172 (2013).
- [67] “Spin Transfer Technologies STT-MRAM,” www.spintransfer.com/spin-transfer-technologies-samples-fully-functional-st-mram-devices [Accessed 26.01.2017].
- [68] Y. Fan, P. Upadhyaya, X. Kou, M. Lang, S. Takei, Z. Wang, J. Tang, L. He, L.-T. Chang, M. Montazeri, G. Yu, W. Jiang, T. Nie, R. N. Schwartz, Y. Tserkovnyak, and K. L. Wang, “Magnetization switching through giant spin-orbit torque in a magnetically doped topological insulator heterostructure,” *Nat Mater* **13**, 699 (2014).
- [69] J. E. Hirsch, “Spin Hall Effect,” *Phys. Rev. Lett.* **83**, 1834 (1999).
- [70] K. Uchida, J. Xiao, H. Adachi, J. Ohe, S. Takahashi, J. Ieda, T. Ota, Y. Kajiwara, H. Umezawa, H. Kawai, G. E. W. Bauer, S. Maekawa, and E. Saitoh, “Spin Seebeck insulator,” *Nat Mater* **9**, 894 (2010).
- [71] O. Mosendz, J. E. Pearson, F. Y. Fradin, G. E. W. Bauer, S. D. Bader, and A. Hoffmann, “Quantifying Spin Hall Angles from Spin Pumping: Experiments and Theory,” *Phys. Rev. Lett.* **104**, 046601 (2010).
- [72] O. Madelung, U. Rössler, and M. Schulz, eds., “Antimony telluride (Sb₂Te₃) crystal structure, chemical bond, lattice parameters (including data for Bi₂Se₃, Bi₂Te₃),” in *Non-Tetrahedrally Bonded Elements and Binary Compounds I* (Springer Berlin Heidelberg, Berlin, Heidelberg, 1998) pp. 1–4.

- [73] P. G. Silvestrov, P. W. Brouwer, and E. G. Mishchenko, "Spin and charge structure of the surface states in topological insulators," *Phys. Rev. B* **86**, 075302 (2012).
- [74] G. Czycholl, *Theoretische Festkörperphysik*, 3rd ed., Springer-Lehrbuch (Springer, Berlin [u.a.], 2008) pp. XVII, 498 S. : graph. Darst.
- [75] R. Li, J. Wang, X.-L. Qi, and S.-C. Zhang, "Dynamical axion field in topological magnetic insulators," *Nat Phys* **6**, 284 (2010).
- [76] L. Hao and T. K. Lee, "Surface spectral function in the superconducting state of a topological insulator," *Phys. Rev. B* **83**, 134516 (2011).
- [77] S. Datta, *Electronic transport in mesoscopic systems*, 1st ed., Cambridge studies in semiconductor physics and microelectronic engineering ; 3, Vol. 3 (Cambridge Univ. Press, Cambridge [u.a.], 1997) pp. XV, 377 S.
- [78] S. Acero, L. Brey, W. J. Herrera, and A. L. Yeyati, "Transport in selectively magnetically doped topological insulator wires," *Phys. Rev. B* **92**, 235445 (2015).
- [79] J. S. Van Dyke and D. K. Morr, "Controlling the flow of spin and charge in nanoscopic topological insulators," *Phys. Rev. B* **93**, 081401 (2016).
- [80] X. Xiao, Y. Liu, Z. Liu, G. Ai, S. A. Yang, and G. Zhou, "All-electric spin modulator based on a two-dimensional topological insulator," *Applied Physics Letters* **108**, 032403 (2016).
- [81] V. Krückl, *Wave packets in mesoscopic systems: From time-dependent dynamics to transport phenomena in graphene and Topological insulators*, Ph.D. thesis, Universität Regensburg (2012).
- [82] M. Joppe, *Spin-Transistor auf der Basis einer Heterostruktur aus einem topologischen Isolator und einem Ferromagneten*, Master's thesis, Universität Bielefeld (2014).
- [83] F. Schwabl, *Quantenmechanik (QM I)*, 7th ed., Springer-Lehrbuch (Springer, Berlin [u.a.], 2007) pp. XV, 430 S. : graph. Darst.
- [84] "CUDA release," www.nvidia.com/object/cuda_home_new.html [Accessed 05.12.2016].
- [85] D. Neuhasuer and M. Baer, "The time-dependent Schrödinger equation: Application of absorbing boundary conditions," *The Journal of Chemical Physics* **90**, 4351 (1989).
- [86] Z.-H. Pan, E. Vescovo, A. V. Fedorov, G. D. Gu, and T. Valla, "Persistent coherence and spin polarization of topological surface states on topological insulators," *Phys. Rev. B* **88**, 041101 (2013).
- [87] O. V. Yazyev, J. E. Moore, and S. G. Louie, "Spin Polarization and Transport of Surface States in the Topological Insulators Bi_2Se_3 and Bi_2Te_3 from First Principles," *Phys. Rev. Lett.* **105**, 266806 (2010).

Bibliography

- [88] X. Wang, G. Bian, T. Miller, and T.-C. Chiang, "Topological spin-polarized electron layer above the surface of Ca-terminated Bi_2Se_3 ," *Phys. Rev. B* **87**, 035109 (2013).
- [89] S. Souma, M. Komatsu, M. Nomura, T. Sato, A. Takayama, T. Takahashi, K. Eto, K. Segawa, and Y. Ando, "Spin Polarization of Gapped Dirac Surface States Near the Topological Phase Transition in $\text{TlBi}(\text{S}_{1-x}\text{Se}_x)_2$," *Phys. Rev. Lett.* **109**, 186804 (2012).
- [90] T. Sato, K. Segawa, H. Guo, K. Sugawara, S. Souma, T. Takahashi, and Y. Ando, "Direct Evidence for the Dirac-Cone Topological Surface States in the Ternary Chalcogenide TlBiSe_2 ," *Phys. Rev. Lett.* **105**, 136802 (2010).
- [91] C. Pauly, G. Bihlmayer, M. Liebmann, M. Grob, A. Georgi, D. Subramaniam, M. R. Scholz, J. Sánchez-Barriga, A. Varykhalov, S. Blügel, O. Rader, and M. Morgenstern, "Probing two topological surface bands of Sb_2Te_3 by spin-polarized photoemission spectroscopy," *Phys. Rev. B* **86**, 235106 (2012).
- [92] M. R. Scholz, J. Sánchez-Barriga, J. Braun, D. Marchenko, A. Varykhalov, M. Lindroos, Y. J. Wang, H. Lin, A. Bansil, J. Minár, H. Ebert, A. Volykhov, L. V. Yashina, and O. Rader, "Reversal of the Circular Dichroism in Angle-Resolved Photoemission from Bi_2Te_3 ," *Phys. Rev. Lett.* **110**, 216801 (2013).
- [93] M. Nomura, S. Souma, A. Takayama, T. Sato, T. Takahashi, K. Eto, K. Segawa, and Y. Ando, "Relationship between Fermi surface warping and out-of-plane spin polarization in topological insulators: A view from spin- and angle-resolved photoemission," *Phys. Rev. B* **89**, 045134 (2014).
- [94] C. Brune, A. Roth, H. Buhmann, E. M. Hankiewicz, L. W. Molenkamp, J. Maciejko, X.-L. Qi, and S.-C. Zhang, "Spin polarization of the quantum spin Hall edge states," *Nat Phys* **8**, 485 (2012).
- [95] B. Dieny, V. S. Speriosu, S. S. P. Parkin, B. A. Gurney, D. R. Wilhoit, and D. Mauri, "Giant magnetoresistive in soft ferromagnetic multilayers," *Phys. Rev. B* **43**, 1297 (1991).
- [96] I. Vobornik, U. Manju, J. Fujii, F. Borgatti, P. Torelli, D. Krizmancic, Y. S. Hor, R. J. Cava, and G. Panaccione, "Magnetic Proximity Effect as a Pathway to Spintronic Applications of Topological Insulators," *Nano Letters* **11**, 4079 (2011), pMID: 21861485.
- [97] J. Liu, T. H. Hsieh, P. Wei, W. Duan, J. Moodera, and L. Fu, "Spin-filtered edge states with an electrically tunable gap in a two-dimensional topological crystalline insulator," *Nat Mater* **13**, 178 (2014).
- [98] S. Middelhoek, "Domain Walls in Thin Ni-Fe Films," *Journal of Applied Physics* **34**, 1054 (1963).
- [99] R. Wakatsuki, M. Ezawa, and N. Nagaosa, "Domain wall of a ferromagnet on a three-dimensional topological insulator," *Scientific Reports* **5**, 13638 (2015).

- [100] S. Essert, V. Krueckl, and K. Richter, "Two-dimensional topological insulator edge state backscattering by dephasing," *Phys. Rev. B* **92**, 205306 (2015).
- [101] P. D. C. King, R. C. Hatch, M. Bianchi, R. Ovsyannikov, C. Lupulescu, G. Landolt, B. Slomski, J. H. Dil, D. Guan, J. L. Mi, E. D. L. Rienks, J. Fink, A. Lindblad, S. Svensson, S. Bao, G. Balakrishnan, B. B. Iversen, J. Osterwalder, W. Eberhardt, F. Baumberger, and P. Hofmann, "Large Tunable Rashba Spin Splitting of a Two-Dimensional Electron Gas in Bi_2Se_3 ," *Phys. Rev. Lett.* **107**, 096802 (2011).
- [102] C. Persson and U. Lindefelt, "Detailed band structure for 3 C -, 2 H -, 4 H -, 6 H -SiC, and Si around the fundamental band gap," *Phys. Rev. B* **54**, 10257 (1996).
- [103] A. Damascelli, "Probing the Electronic Structure of Complex Systems by ARPES," *Physica Scripta* **2004**, 61 (2004).
- [104] C. Jozwiak, C.-H. Park, K. Gotlieb, C. Hwang, D.-H. Lee, S. G. Louie, J. D. Denlinger, C. R. Rotundu, R. J. Birgeneau, Z. Hussain, and A. Lanzara, "Photoelectron spin-flipping and texture manipulation in a topological insulator," *Nat Phys* **9**, 293 (2013).
- [105] C.-H. Park and S. G. Louie, "Spin Polarization of Photoelectrons from Topological Insulators," *Phys. Rev. Lett.* **109**, 097601 (2012).
- [106] R. Meservey, P. M. Tedrow, and P. Fulde, "Magnetic Field Splitting of the Quasiparticle States in Superconducting Aluminum Films," *Phys. Rev. Lett.* **25**, 1270 (1970).
- [107] A. A. Zyuzin, M. D. Hook, and A. A. Burkov, "Parallel magnetic field driven quantum phase transition in a thin topological insulator film," *Phys. Rev. B* **83**, 245428 (2011).
- [108] R. E. Prange, "Tunneling from a Many-Particle Point of View," *Phys. Rev.* **131**, 1083 (1963).
- [109] R. C. Dynes, V. Narayanamurti, and J. P. Garno, "Direct Measurement of Quasiparticle-Lifetime Broadening in a Strong-Coupled Superconductor," *Phys. Rev. Lett.* **41**, 1509 (1978).
- [110] O. Schebaum, *Bestimmung der Spinpolarisation durch supraleitende Tunnelspektroskopie*, Ph.D. thesis, Universität Bielefeld (2011).
- [111] R. Meservey and P. Tedrow, "Spin-polarized electron tunneling," *Physics Reports* **238**, 173 (1994).
- [112] Z. Alpichshev, J. G. Analytis, J.-H. Chu, I. R. Fisher, Y. L. Chen, Z. X. Shen, A. Fang, and A. Kapitulnik, "STM Imaging of Electronic Waves on the Surface of Bi_2Te_3 : Topologically Protected Surface States and Hexagonal Warping Effects," *Phys. Rev. Lett.* **104**, 016401 (2010).